

Colloid-based Heterogeneous Catalysts with Tuneable Size and Surface Properties

Vorgelegt von

M. Sc.

Anton Sagaltchik

an der Fakultät II – Mathematik und Naturwissenschaften
der Technischen Universität Berlin

Zur Erlangung des akademischen Grades

Doktor der Naturwissenschaften

- Dr. rer. nat. -

genehmigte Dissertation

Promotionsausschuss:

Vorsitzender: Prof. Dr. Thomas Friedrich

Gutachter: Prof. Dr. Arne Thomas

Gutachter: Prof. Dr. Peter Behrens

Tag der wissenschaftlichen Aussprache: 17.02.2020

Berlin 2020

Danksagung

An dieser Stelle möchte ich mich bei allen Personen bedanken, die mich während meiner Promotion unterstützt und zum Gelingen dieser Arbeit beigetragen haben.

Zuerst möchte ich bei meinen Betreuern Prof. Arne Thomas und Dr. Frank Rosowski für die Möglichkeit, meine Arbeit am BasCat-Institut anzufertigen, bedanken. Beide hatten während meiner gesamten Promotion immer ein offenes Ohr für Probleme, deren Lösungen, sowie Ideen aller Art. Die zahlreichen Diskussionen haben mir geholfen, mich sowohl fachlich, als auch persönlich weiterzuentwickeln.

Mein Dank geht ebenfalls an Prof. Peter Behrens für die Erstellung des Zweitgutachtens über diese Dissertation sowie an Prof. Thomas Friedrich für die Übernahme des Prüfungsvorsitzes der wissenschaftlichen Aussprache.

Bei Dr. Michael Geske möchte ich mich besonders für die vielen wissenschaftlichen Diskussionen bedanken. Nicht nur der große Erfahrungsschatz hinsichtlich der technischen Seite der Katalyse, sondern auch die Bereitschaft sein Wissen bis ins kleinste Detail zu vermitteln, machte die Arbeit mit ihm sehr wertvoll für mich.

Ein großer Dank gilt allen Personen, die mir mit der Durchführung verschiedener Analysemethoden geholfen haben. Nicht selten führten die Ergebnisse dieser Analysen im Anschluss zu tiefergehenden wissenschaftlichen Diskussionen, welche diese Arbeit maßgeblich beeinflusst haben. Danke an Dr. Johannes Schmidt und Dr. Cheng Hefeng für XPS-Messungen, an Sören Selve, Dr. Thomas Lunkenbein, Jan Simke, Dr. Milivoj Plodinec und Ramzi Farra für TEM-Messungen, an Ulrich Gernert und Christoph Fahrenson für SEM-Messungen, an Dr. Frank Girgsdies, Jasmin Allan und Maria Unterweger für XRD-Messungen, an Dr. Andrey Tarasov für TG-MS-Messungen, an Astrid Müller-Klauke und Iris Pieper für ICP-OES-Messungen und an Christina Eichenauer für Sorptions- und TGA-Messungen.

Von großer Bedeutung war auch die Hilfe bei Analysemethoden am BasCat-Institut, daher danke für die Unterstützung an Julia Bauer und Dr. Raoul Naumann D'Alno-court bei TPO und TPR-Messungen, an Kristian Knemeyer beim Ozon-Experiment und an Phil Preikschas bei IR-Messungen.

Zudem möchte ich mich bei Dr. Chengyue Guan und dem hte-Team, vor allem Michael Lejkowski und Armin Lange de Oliveira, für die Messungen meiner Katalysatoren bedanken. An dieser Stelle auch danke für die Zusammenarbeit an die Beteiligten am EO-Projekt Piyush Ingale, Dennis Meiling, Dr. Leon Zwiener, Dr. Maximilian Lamoth und Dr. Elias Frei.

Rückblickend betrachtet ist meine Promotionszeit schnell vorübergegangen. Neben meinen spannenden Projekten lag dies vor allem an meinen Kollegen und der damit verbundenen großartigen Arbeitsatmosphäre am BasCat. Zusätzlich zu den oben genannten Kollegen, danke an Dr. Benjamin Frank, Rhea Christodoulou, Felix Pohl, Noah Subat, Martin Conrad, Stephen Lohr, Jan Meißner, Emanuela Toussaint, Daniel Eichholz, Javier Silva Mora, Dr. Jingxiu Xie, Dr. Mar Hermida, Dr. Gregor Koch, Dr. Christian Schulz, Dr. Verena Stempel, Dr. Stephanie Linke, Dr. Ralph Krähnert, Alessandro Nagel und Peter Ebert vom BasCat. Auch ein großes Dankeschön an die Kollegen vom AK Thomas für die vielen lustigen Stunden.

Zu guter Letzt möchte ich meinen Freunden, meiner Familie und Katrin für die Unterstützung während der letzten Jahre danken.

Abstract

Improvements in catalyst's performance for technical processes stagnated over the last decades. The need for new approaches towards better performing catalysts is apparent. In this thesis, colloidal synthesis methods are examined for different heterogeneously catalyzed reactions. With colloidal methods, size and shape of nanoparticles can be controlled precisely by various reaction parameters like temperature, pH value etc. During synthesis, the particle surface can be modified, e.g. by introducing another species which deposits at the surface to give core-shell particles. The advantages of colloidal methods were exploited to synthesize well-defined catalysts which were tested for the ethylene epoxidation or the dry reforming of methane.

The ethylene epoxidation is a major petrochemical process in which a supported silver catalyst is used. The industrial catalyst shows a very heterogeneous particle size distribution. In chapter 2, a particles size study of silver particle supported on α -alumina was conducted to compare the performance for differently sized silver particles to each other. Colloidal silver nanoparticles with narrow particle size distributions were successfully synthesized. Furthermore, particles smaller than 10 nm were excluded with the colloidal synthesis route, which is challenging using conventional synthesis methods. Three supported samples with differently sized silver nanoparticles (40, 60 and 100 nm on average) were prepared. Among the prepared samples smaller silver particles (40 nm) showed the highest selectivity for ethylene epoxidation if unpromoted. When ethylene chloride was added as the promoter to the feed, the selectivities for all samples were levelled out.

In chapter 3 the effect of sulfur, which is added to the promoter package of the industrial silver catalyst, was examined. By colloidal synthesis, silver-silver sulfide core-shell particles were produced. The supported core-shell particles were compared with an unpromoted colloid-based catalyst from chapter 2 and a colloid-based catalyst to which a sulfate species was added. The test revealed the superior performance of the sulfate promoted catalyst, whereas the sulfide samples performed poorly. This indicates that sulfate is the active sulfur species and there is no conversion of sulfides to sulfates during catalysis. Furthermore, XPS measurements of the spent samples showed that the sulfate is positioned at the support and not on silver particles after catalysis.

The reaction of carbon dioxide and methane to carbon monoxide and hydrogen is an ecologically and economically attractive process, as two greenhouse gases react to more valuable synthesis gas. However, for this endothermic reaction high temperatures of up to 800 °C are needed. At these temperatures many catalysts suffer from strong deactivation, mainly by sintering and coke deposition. In chapter 4, nickel phosphide-manganese oxide core-shell particles were synthesized by colloidal methods, supported on γ -alumina and tested for dry reforming of methane. The performance of this material was compared to a catalyst with supported nickel phosphide nanoparticles. Both catalysts showed high activity and very good stability over 60 h time on stream. By TG-MS measurements of the spent catalysts the sample with manganese showed 35 % less coke deposition in comparison to the pure nickel phosphide sample.

In the last chapter a support variation for the dry reforming of methane was examined. Ordered mesoporous zirconium oxide was synthesized with the nanocasting method, whereby KIT-6 was used as the template. The final BET surface area of 244 m²/g is the highest for a hard templated crystalline zirconia to our knowledge. Nickel was deposited via dry impregnation. The catalytic performance was compared with an aluminum supported nickel catalyst with similar metal loading. Until 700 °C, the mesoporous zirconia support outperformed the reference catalyst. At higher temperatures the surface area, and consequently the performance, decreased. Nevertheless, the performance of the zirconia supported sample per surface area showed a better performance compared to the alumina supported sample indicating a promoter effect by the zirconia support.

Deutsche Kurzzusammenfassung

In den letzten Jahrzehnten stagnierte die Leistungssteigerung von Katalysatoren für großtechnische Prozesse. Daher ist es notwendig, neue Wege in der Herstellung von aktiveren Katalysatoren zu finden. In dieser Arbeit werden kolloidale Synthesemethoden für verschiedene heterogen katalysierte Reaktionen untersucht. Mit kolloidalen Methoden können Größe und Form von Nanopartikeln durch verschiedene Reaktionsparameter präzise gesteuert werden. Darüber hinaus kann während der Synthese die Partikeloberfläche modifiziert werden, z.B. durch Einbringen einer anderen Spezies, die sich an der Oberfläche ablagert. Mittels dieser Methode werden sogenannte Core-Shell-Partikel erzeugt. In dieser Arbeit wurden die Vorteile kolloidaler Methoden genutzt, um genau definierte Katalysatoren zu synthetisieren, die für die Ethylenepoxidierung oder für die Trockenreformierung von Methan getestet wurden.

Die Ethylenepoxidierung ist ein wichtiges petrochemisches Verfahren, bei dem ein geträgerter Silberkatalysator verwendet wird. Der technische Katalysator zeigt jedoch eine sehr heterogene Partikelgrößenverteilung. In Kapitel 2 wurde daher eine Partikelgrößenstudie von Silberpartikeln auf α -Aluminiumoxid für die Ethylenepoxidierung durchgeführt, um die Aktivität für unterschiedlich große Silberpartikel miteinander zu vergleichen. Silberkolloide mit engen Partikelgrößenverteilungen wurden erfolgreich synthetisiert. Des Weiteren wurden bei Elektronenmikroskopiemessungen keine Partikel detektiert, welche kleiner als 10 nm sind. Es wurden drei geträgerte Katalysatoren mit unterschiedlich großen Silberpartikeln (durchschnittlich 40, 60 und 100 nm) hergestellt. Im Vergleich dieser Proben zeigten kleinere Silberpartikel (40 nm) die höchste Selektivität zu Ethylenoxid, sofern kein Promoter zugegeben wurde. Sobald Ethylenchlorid als Promotor dem Gasstrom zugesetzt wurde, glichen sich die Selektivitäten zu Ethylenoxid für alle Katalysatoren an.

In Kapitel 3 wurde der Einfluss von Schwefel, welcher dem Promotorpaket des industriellen Silberkatalysators zugesetzt wird, untersucht. Durch kolloidale Synthese wurden Silber/ Silbersulfid Core-Shell-Partikel hergestellt. Die geträgerten Core-Shell-Partikel wurden mit einem unpromotierten Katalysator auf Kolloidbasis aus Kapitel 2 und einem Katalysator auf Kolloidbasis, dem eine Sulfatspezies zugesetzt worden war, verglichen. Das Katalysatorscreening zeigte, dass der Katalysator mit Sulfatzusatz die beste Aktivität aufwies, während die Sulfidproben eine sehr geringe

Aktivität zeigten. Dies deutet darauf hin, dass die Sulfatspezies die aktive Schwefelspezies ist und während der Reaktion keine Umwandlung von Sulfiden in Sulfate erfolgt. Darüber hinaus zeigten XPS-Messungen der verbrauchten Katalysatoren, dass sich die Sulfatspezies nach der Katalyse auf dem Träger und nicht auf den Silberpartikeln befindet.

Die Reaktion von Kohlenstoffdioxid und Methan zu Kohlenstoffmonoxid und Wasserstoff ist ein ökologisch und wirtschaftlich attraktiver Prozess, da zwei Treibhausgase zu wertvollerem Synthesegas reagieren. Für diese endotherme Reaktion sind jedoch hohe Temperaturen von bis zu 800 °C erforderlich. Bei solch hohen Temperaturen deaktivieren viele Katalysatoren in kurzer Zeit. Die Hauptgründe für die Deaktivierung sind dabei hauptsächlich Sintern und Koksabscheidung. In Kapitel 4 wurden Nickelphosphid-Manganoxid Core-Shell-Partikel mittels kolloidaler Methoden synthetisiert, auf γ -Aluminiumoxid geträgert und für die Trockenreformierung von Methan getestet. Die Aktivität dieses Katalysators wurde mit einem Katalysator mit geträgerten Nickelphosphidkolloiden verglichen. Beide Katalysatoren zeigten eine hohe Aktivität und eine sehr gute Stabilität bei einer Betriebsdauer von mehr als 60 Stunden. Durch TG-MS-Messungen der verbrauchten Katalysatoren zeigte die Probe mit zusätzlichem Mangan 35% weniger Koksablagerung im Vergleich zur reinen Nickelphosphidprobe.

Im letzten Kapitel wurden verschiedene Träger für die Trockenreformierung von Methan untersucht. Geordnetes, mesoporöses Zirkoniumdioxid wurde mittels hartem Templatieren hergestellt, wobei KIT-6 als Templat verwendet wurde. Mit einer BET-Oberfläche von 244 m²/g weist das so hergestellte Zirkoniumdioxid unseres Wissens nach die höchste BET-Oberfläche für ein harttemplatiertes, kristallines Zirkoniumdioxid auf. Nickel wurde durch Trockenimprägnierung auf den Trägern abgeschieden. Die katalytische Aktivität wurde mit einem aluminiumgeträgerten Nickelkatalysator mit ähnlicher Metallbeladung verglichen. Bis 700 °C übertraf der mesoporöse Zirkoniumdioxidträger die Aktivität des Referenzkatalysators. Bei höheren Temperaturen nahm die Oberfläche und damit die Aktivität des mesoporösen Zirkoniumdioxidträgers ab. Nichtsdestotrotz zeigte die zirkoniumgeträgerte Probe pro Oberfläche eine bessere Aktivität im Vergleich zu der Probe mit dem Aluminiumoxidträger, was auf einen Promotoreffekt durch den Zirkoniumdioxidträger hindeutet.

Contents

1. Introduction	1
1.1. Heterogeneous Catalysis and Conventional Synthesis Methods	1
1.2. Colloidal Methods in Heterogeneous Catalysis	7
1.3. Scope of the Thesis	11
2. Particle Size Study with Colloid-based Model Catalysts for Ethylene Epoxidation	13
2.1. Introduction	13
2.2. Experimental	18
2.2.1. Standard Procedure for Silver Nanoparticle Synthesis with Single Injection Method	18
2.2.2. Standard Procedure for Silver Nanoparticle Synthesis with Multiple Injection Method	18
2.2.3. Synthesis of > 100 nm Silver Nanoparticles with Multiple Injection Method	19
2.2.4. Supporting of Tannic Acid Capped Silver Nanoparticles on α -Alumina	19
2.2.5. Catalytic Screening	19
2.2.6. Colloids and Catalysts Characterization	20
2.3. Results	22
2.3.1. Colloidal Silver Synthesis	22
2.3.2. Impregnation and Removal of Stabilizer	28
2.3.3. Performance Test	40
2.3.4. Characterization of Spent Samples	44
2.3.5. New Synthesis Method for Silver Nanoparticles	46
2.4. Conclusion	50
3. Sulfur Promotion Study for Ethylene Epoxidation	52
3.1. Introduction	52
3.2. Experimental	54

3.2.1.	Synthesis of Silver-Silver Sulfide Core-Shell Particles	54
3.2.2.	Preparation of XPS Reference Samples	54
3.2.3.	Catalytic Screening	55
3.2.4.	Characterization of Silver-Silver Sulfide Colloids and Supported Samples	55
3.3.	Results	57
3.3.1.	Silver-Silver Sulfide Core-Shell Particle Synthesis and Characterization	57
3.3.2.	Performance Test	61
3.3.3.	Characterization of Spent Samples	64
3.4.	Conclusion	65
3.5.	Appendix	66
4.	Supported Nickel Phosphide-Manganese Oxide Promoted Core-Shell Particles for DRM	67
4.1.	Introduction	67
4.2.	Experimental	71
4.2.1.	Synthesis of Colloidal Nickel Phosphide-Manganese Oxide Core-Shell Particles	71
4.2.2.	Synthesis of Colloidal Nickel Phosphide Particles	71
4.2.3.	Impregnation of Nickel Phosphide-Manganese Oxide Core-Shell Particles on Puralox®	72
4.2.4.	Catalytic Screening	72
4.2.5.	Colloids and Catalyst Characterization	72
4.3.	Results	74
4.3.1.	Synthesis and Characterization of Core-Shell Particles and Nickel Phosphide Colloids	74
4.3.2.	Synthesis and Characterization of Supported Catalysts before DRM Test	79
4.3.3.	DRM Performance Test	87
4.3.4.	Characterization of Spent Catalysts	90
4.4.	Conclusion	96
4.5.	Appendix	97

5. Mesoporous Zirconium Oxide as Novel Support for Dry Reforming of Methane	98
5.1. Introduction	98
5.2. Experimental	100
5.2.1. Synthesis of Mesoporous KIT-6	100
5.2.2. Synthesis of Mesoporous Zirconium Oxide	100
5.2.3. Catalysts Synthesis via Dry Impregnation Method	100
5.2.4. Catalytic Screening	101
5.2.5. Characterization of Catalysts	101
5.3. Results	103
5.3.1. Mesoporous Zirconium Oxide Synthesis and Characterization	104
5.3.2. Synthesis and Characterization of Supported Samples	107
5.3.3. DRM Performance Test	111
5.3.4. Characterization of Spent Catalysts	113
5.4. Conclusion	116
6. Summary and Outlook	117

1. Introduction

1.1. Heterogeneous Catalysis and Conventional Synthesis Methods

Catalysis is an indispensable pillar of today's society. A catalyst is a material which changes the reaction path and thereby decreases the activation energy (figure 1.1). Usually, this leads to higher product yields over time. Additionally, the catalyst is not consumed during the reaction. In around 90 % of processes in chemical industry a catalyst is added, underlining the importance regarding economic, ecologic and energetic aspects.^[1,2]

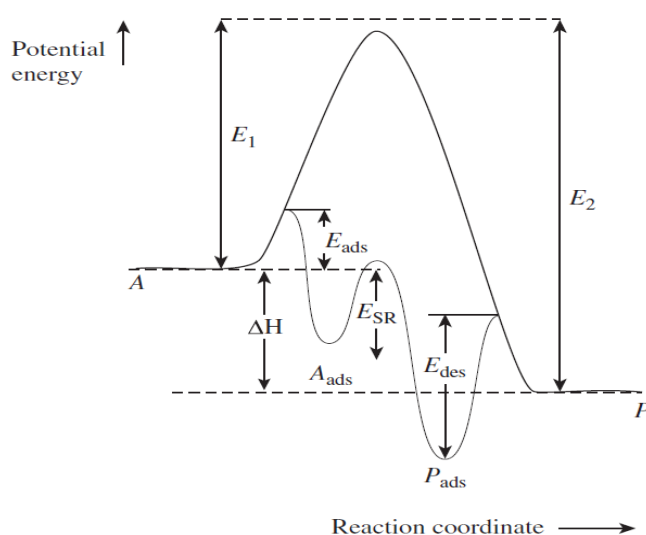


Figure 1.1. Thermodynamic reaction progress of educt A to product Z with and without a catalyst. With catalyst addition the activation energy for the reaction is decreased. Adopted from ^[3].

The field of catalysis is conventionally split in three different classes, namely the biological, the homogeneous and the heterogeneous catalysis. From these the latter one accounts for the majority of technical processes.^[1] In heterogeneous catalysis, the reactants exist in a different phase than the catalyst. Although in homogeneous catalysis the mixing of reactants and catalyst is better, which leads to higher selectivity in most cases, heterogeneously catalyzed reactions have the advantages of better product separation from the catalyst as well as longer lifetime leading to a greater product output over time. Following, only the industrially more relevant heterogeneous catalysis will be discussed.

Catalysts are solid materials which can be a supported or unsupported metal or metal oxides among others. Supported metal catalysts are usually precious metals with low weight loading on high surface area oxide supports, like silica or alumina. In this case only the metal is the active component, whereas in unsupported catalyst most of the surface is catalytically active.

There are many different ways to synthesize these complex materials. The most common synthesis methods for supported catalysts are the dry impregnation or incipient wetness method and the coprecipitation method.^[4–6] In the former, the metal/metal oxide precursor is dissolved in a suitable solvent with the same volume as the pore volume of the used support. Following the physical mixing, the precursor is pulled in the pores of the support by capillary forces. Subsequent drying and calcination give the desired metal/metal oxide on the support. If needed, a reduction step can be conducted to reduce the metal oxide to the corresponding metal. A similar method is the wet impregnation in which more solvent is used in comparison to the dry impregnation. In this case the precursor diffuses into the pores.

The other conventional synthesis method is the coprecipitation method. The precursor(s) are stirred in a reaction vessel and then suddenly precipitated by pH adjustment or oversaturation of the reaction mixture. Certainly, these methods seem simple at first, however as De Jongh et al. and Behrens et al. pointed out in recent studies, there are many parameters, which can be optimized.^[6–8] According to these groups each synthesis step should be carefully conducted to exploit the potential of the catalyst and ensure reproducibility. A scheme for a conventionally synthesized catalyst via dry impregnation is shown in figure 1.2.

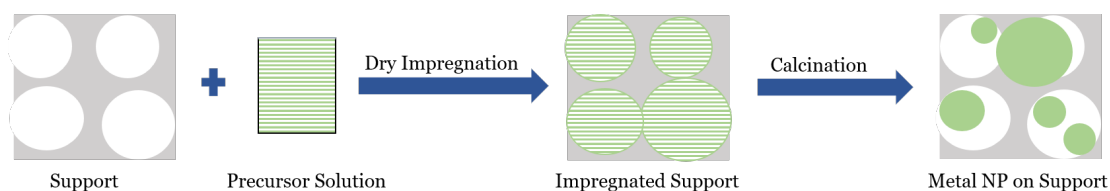


Figure 1.2. A precursor solution is mixed with the support. The volume is the same as the pore volume of the support. After calcination, particles with a broad range of particle sizes, depending on the position in/on the pore, form.

Optimizing the catalytic performance regarding activity, selectivity and longevity is the major goal in catalyst research. This is why promoters are added to many catalyst

formulations.^[9] According to McCue and Anderson promoters are substances that enhance the catalytic performance regarding above stated parameters.^[10]

Promoters can interact with the active metal/site in different ways. Electronic promoters are the most common kind of promoters. The promoter donates or withdraws electrons to/from the active site. An example is tungsten oxide for the selective reduction catalyst (SCR). The high oxygen mobility of WO_3 stabilizes the active V-O-V species responsible for the reduction of NO with ammonia.^[11] Another example is the Fischer-Tropsch reaction where many promoters are able to enhance the performance of supported transition metal catalysts. As Xie et al. reported, adding Na_2S to a supported iron catalyst increases the selectivity to the desired higher C_2 - C_4 olefins.^[12] Sodium donates electrons to the active iron carbide particles, while sulfur, when compared to oxygen counterions, draws less charge back from the iron carbide surface. The electron donation changes the binding strength for hydrogen atoms on the metal carbide surface and thus, decreases the amount of methane formation.

Particle shapes or the presence of exposed metal or metal oxide facets can be modified by structural promoters. Structural promoters change the geometry of active sites or block non-active binding sites. Regarding for example the Fischer-Tropsch process also factors like particle size and shape play a decisive role. Li et al. reported the synthesis of cobalt manganese composite oxide by coprecipitation.^[13] Under reaction conditions this mixed oxide reacted to cobalt carbide nanoprisms. Beside manganese, other promoters like cerium, lanthanum and aluminium were used to synthesize bimetallic catalyst. However, only with manganese formation of cobalt carbide nanoprisms was observed and this sample was also most selective towards the desired C_2 - C_4 olefins and least selective towards undesired methane. The reason for this was the shape of the nanoprisms where (101) and (020) facets are exposed. Those facets are supposedly more selective towards higher olefins. Another example is the copper promotion of supported palladium catalyst for the hydrogenation of acetylene to ethene as published by Kim et al.^[14] In this case, copper binds to the low coordination sites of Pd and thereby increases the selectivity to ethene, while the activity is barely affected.

Increasing the lifetime of catalysts can be achieved by blocking poisonous substrates. Preventing the formation of carbon/coke overlayer can keep catalysts for CO

methanation active for a long time. Examples for this class of promoters are metal oxides which can burn off carbon depositions at high temperatures like vanadia or magnesia.^[15,16] This kind of promotion will be discussed in more detail in chapter 4.

Novel synthesis methods for better promoter/metal interaction

For all kind of promoters close proximity to the active metal/metal oxide is beneficial for the final catalysts performance. In industry, most commonly used methods to deposit promoters with the active metal/metal oxides are by co-impregnation or co-precipitation. Those methods work as described on page two, only with added promotional metal or metal oxide precursors in the solution. However, with these methods the distribution of promoter and active metal is random. Thus, establishing a method where the final distribution can be controlled is of great interest. There are novel methods to maximize the contact area between active metal/metal oxide and promoters described in literature. Here, the first introduced method is called surface redox method (SR).^[14] A supported metal catalyst is reduced to obtain chemisorbed hydrogen on metal binding sites. The solid is stirred in an aqueous solution of another cationic metal species. This cation exchanges with the hydrogen and thus, binds directly to the active metal.^[17] The metal/promoter ratio can be adjusted by cation concentration in the aqueous solution. This method is limited in a way that only metals can be used, which chemisorb hydrogen and have a strong interaction with the promoter metal.

Supported metal catalysts can also be modified by atomic layer deposition.^[18–21] A layer of metal or metal oxide can be deposited on a material by reaction of a precursor with the surface groups of the material, e.g. hydroxyl groups. As the surface groups are finite, this step is self-limited. After flushing out the precursor with inert gas, the first half-cycle is complete. The monolayer of the promoter precursor is then exposed to a second precursor to give the final metal/metal oxide monolayer. This step is called second half-cycle. In between the reaction chamber is purged to remove precursor residues. The desired layer thickness can be obtained by repeating the cycle multiple times. Furthermore, also unsupported catalysts can be used for ALD modification. Examples are the phosphorus deposition on vanadia to give a selective catalyst for the selective oxidation of *n*-butane to maleic anhydride and the coating of nickel particles with alumina to give a very active catalyst for the dry reforming of methane.^[22,23]

Another novel strategy is the single source precursor (SSP) approach. A single metalorganic complex is synthesized containing two (or more) metals. The final metal ratio can be controlled by the stoichiometry of the synthesized complex. Another advantage is the molecular interaction between active metal/metal oxide and promoter, especially benefitting electronical promoters. Preikschas et al. synthesized a rhodium-manganese complex for the synthesis gas to ethanol conversion. Manganese is the promoter for rhodium, which is the only known single metal catalyst to show selectivity towards ethanol in this reaction. The complex is supported on silica and subsequent decomposition yields well dispersed rhodium manganese particles in close proximity. This catalyst outperformed other supported rhodium manganese catalysts, which were synthesized by conventional methods.^[24] Menezes et al. synthesized an unsupported nickel manganese catalyst for the dry reforming of methane by using nickel manganese oxalate as the SSP. By varying the manganese amount in the precursor complexes and thus, in the final material, they could demonstrate a promotion effect of manganese.^[25] Drawbacks are the synthesis efforts for the single source precursor, which are not commercially available in most cases. Furthermore, the approach cannot be extended to all metal combinations as complex formation is not possible or the ligand decomposition is not feasible.

Industrial Processes

Catalytic reactions take place at the catalyst's surface, or more precisely at the active site. For most catalytic systems however, the active site is unknown. Even the active site of a simple reaction like the oxidation of CO to CO₂ is debated in literature.^[26–28] Although there was much improvement for many industrial processes in the last decades, the source of improvement or a general understanding of the underlying mechanism with all influencing effects like support-metal interactions, promoters etc. is in most cases not fully understood. Following examples show the stagnation of improvement over the last years based on industry patents (figure 1.3).

The selective oxidation of ethylene to ethylene oxide is a circular process, which means the selectivity is a key parameter regarding the catalyst's performance. Nowadays a silver supported catalyst with many promoters is used. In the 1980s and 1990s the selectivity could be improved from 74 % to 86 %.^[29–31] This improvement can be mainly ascribed to the discovery of new promoters by try and error experiments. A major advancement was the discovery of rhenium as a promoter, which

was patented by Shell in 1988.^[30] As can be seen in figure 1.3, this discovery strongly increased the selectivity towards ethylene oxide. A more detailed discussion about promoter mechanisms will be given in chapter 2 and 3. In earlier patents selectivity values were measured at 40 % oxygen conversion to compare with older patents. Newer patents show selectivities up to 90 % EO without focusing on constant oxygen conversion as the circular process is nowadays widely adopted.^[32,33] Improvements in the last two centuries are based on promoter fine tuning, but also improvements from the process site lead to higher product output.

Another example for stagnation of catalyst's performance improvement in industrial processes is the selective oxidation of *n*-butane to maleic anhydride over a vanadyl pyrophosphate catalyst (VPP). In this case, the product yield is regarded. From 1975 to 1985 a 10 % yield increase can be observed.^[34,35] Better knowledge of the active phase and thus, performance increasing pretreatment to obtain a more selective crystal phase was discovered. After that, the yield increased only by few percent by tuning the promoter package for the vanadyl pyrophosphate catalyst.^[36,37] The nature of the active site is still under debate and over the last years no significant improvement could be achieved.^[38]

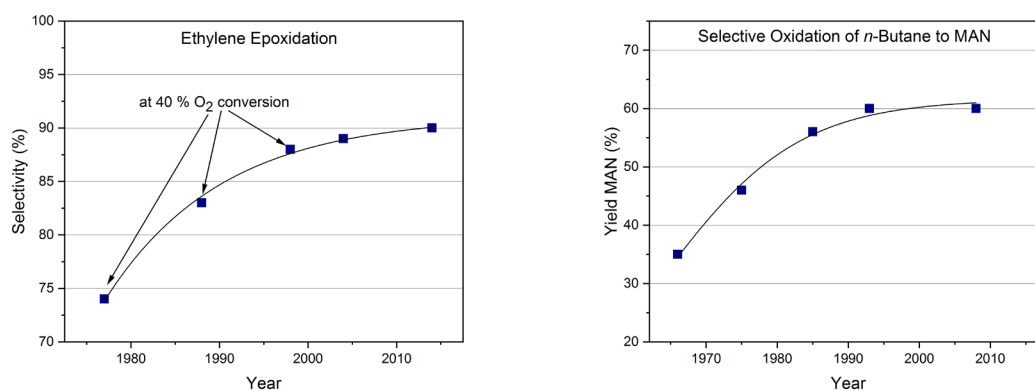


Figure 1.3. Performance data of industrial processes based on patents. Left: Selectivity to ethylene oxide in the selective oxidation of ethylene. The selectivity is strongly dependant on the conversion and process conditions. The performance increasement in earlier years is due to improvement of the added promoter package.^[29–33] Right: Yield of maleic anhydride in the selective oxidation of *n*-butane. The strong yield improvement from 1966 to 1985 was due to optimization of the synthesis pretreatment procedure.^[34–38]

To ensure further improvement, new materials must be introduced. Success probability of a try and error approach is very low, instead a rational design of catalysts is necessary.

The foundation for a rational design of catalysts is an interdisciplinary mode of operation. While the “perfect” catalyst could be designed by computational methods, it is still up to synthetic chemist to fabricate these catalysts.^[39,40] Therefore, control of each synthetic parameter is necessary. The synthesis of anything and everything is still (and will be for a long time) a “holy grail” in chemistry.^[41] In contrast to the aforementioned conventional synthesis methods, colloidal methods bring us one step closer in achieving this goal.

1.2. Colloidal Methods in Heterogeneous Catalysis

The composition and structure of a catalyst are essential for its performance. Hence, particular attention should be given to the synthesis route. By implementing colloidal synthesis methods, a greater control over size and shape of metal particles can be achieved.^[42,43] For metal or metal oxide particles a lowering of particle size to few nanometers changes electronic state density, magnetic and optical properties besides others in comparison to their bulk equivalents.^[44] Besides an increase in surface area, different defect formations and surface and strain-driven lattice distortion can have significant effects on catalytical performance.^[45,46] The particle’s final shape and size can be controlled by varying reaction parameters such as precursor/ligand ratio, concentration, the ligand nature, temperature, pH, stirring speed and mode etc. A detailed discussion of the nanoparticle formation mechanism will be given below. The uniformity of the particle size is another important aspect in synthesis. By producing the nanoparticles via colloidal methods a narrow particle size distribution can be obtained, which is fundamental for particle size studies. With particle size studies of heterogeneous catalysts a structure-activity relationship for the examined reaction can be drawn. In this regard, uniform particle sizes are crucial for final conclusions. Examples from literature and thoroughly discussion about different particle size studies for the ethylene epoxidation will be given in chapter 2.

In addition to the size effect, the particle shape plays an important role as well. Many catalytic reactions seemingly prefer a certain crystal plane of the used metal/ metal

oxide.^[47–49] By varying the shape e.g. as spheres, cubes or triangular particles, an effect on surface energies and thus, on catalytical performance can be seen.^[50] This can be achieved by employing certain stabilizers, which selectively bind to specific crystal planes. At the blocked crystal planes further growth is limited so that addition of atoms will lead to anisotropic growth.^[51,52]

To produce nanoparticles with a bottom-up approach, usually a metal/ metal oxide precursor is dissolved in a suitable solvent and then reduced or decomposed. The formed nanoparticles are then stabilized by ligands. Thus, the precursor/ligand ratio is crucial for the final particle size. A theory which describes the nucleation and growth of nanoparticles is the LaMer model.^[53–55] According to the LaMer model (figure 1.4), nanoparticle formation can be divided into three stages. After addition of a reducing agent, the dissolved precursor cation is reduced to metal atoms. At a certain concentration of metal atoms, a burst nucleation occurs due to oversaturation. This can be interpreted as a homogeneous nucleation. For a narrow particle size distribution this phase should be short to prevent multiple nucleation events. In the third stage more metal atoms accumulate at the nuclei surface. The particles grow until an equilibrium concentration is reached.

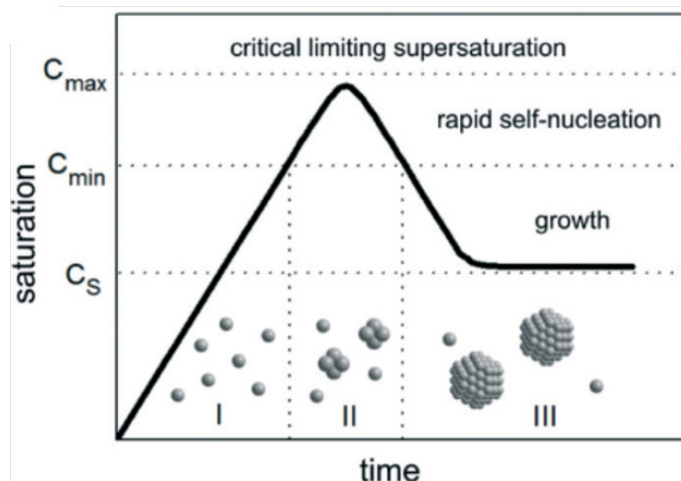


Figure 1.4. Model of particle formation mechanism as postulated by LaMer. In the first phase the precursor is reduced to metallic atoms. If a critical atom concentration is reached the fast nucleation event occurs. Remaining or new formed atoms nucleate at the surface of existing particles until saturation is reached. Adopted from ^[55].

Besides structure, also the surface composition of nanoparticles can be changed, e.g. by coating a nanoparticle with another metal/metal oxide to yield core-shell particles. Core-shell nanoparticles are defined as composite materials with nanoscaled

cores (inner layer) and shells (outer layer).^[56] Cores and shells can be composed of organic materials, for the most part polymers, and inorganic material, e.g. metals or metal oxides.^[57] The highly variable composition of these materials leads to a myriad of applications, such as catalysis, electrochemistry and biomedical applications amongst others.^[58–60] The motivation to synthesize these materials is to stabilize active particles, e.g. with a silica shell, or combine the desired properties of different materials. In addition, due to the high contact area significant synergistic effects between core and shell can occur that could result in materials with new properties or improved properties regarding a certain application. For the synthesis of core-shell particles the concept of heterogeneous nucleation is used. Newly formed metal atoms rather attach to already existing nanoparticles or nuclei instead of forming new particles (homogenous nucleation).^[61,62] This is possible for slow nucleation rates when it is energetically more unfavorable to form new nanoparticles. In literature, the notation “core”@”shell” is most common. Therefore, also in the thesis, the core material will be named first, followed by the shell material.

Despite numerous publications and research projects, catalysts synthesized by colloidal methods are almost non-existent in industrial applications. There are two main challenges for the colloidal approach. First, to avoid sintering the loading needs to be kept at low percentages.^[63] Sintering can occur by many mechanisms, therefore the particles should have a certain distance between each other. However, too harsh reaction conditions, e.g. above the Tamman temperature of the used metal/ metal oxide, will lead to sintering anyway.^[64] The Tamman temperature is the temperature at half the temperature of the melting point (in Kelvin) where atoms in the bulk become mobile.^[65] As some catalytic processes need a certain metal loading, colloidal synthesized catalysts are not suitable for all industrial processes. In these cases, they can serve as model catalysts. Model catalysts are well-defined materials, where the tuneable structure allows to give a structure-reactivity relationship and thus, more information about the catalytic mechanism of the regarded process.^[66]

The second challenge is the stabilizer removal. Nanoparticles need the stabilizers to keep their size.^[67] Stabilizers can interact by electrostatic or steric repulsion. After supporting, the nanoparticles are ideally stabilized against sintering by the pore geometry of the support. The attached stabilizer can have a detrimental effect, as they

block binding sites of the active material. For stabilizer removal several procedures have been suggested. Methods include heat treatments at low temperatures for a long time or at high temperature for a short time,^[68,69] UV radiation,^[70] ozone treatment^[71] and solvent extraction.^[72,73] Some groups have shown that a partial ligand removal can have beneficial effects for catalysis in comparison to complete removal, as the ligands alter the electronic density at the metal.^[69,74]

1.3. Scope of the Thesis

The above-described needs for innovation on the one hand and deeper understanding of catalytic reactions on the other hand lead to the implementation of new synthesis routes to obtain well-defined catalysts. The objective of the present work is to apply materials synthesized by colloidal methods as heterogeneous catalysts under industrially relevant conditions. To obtain colloids, various techniques, e.g. heat-up method, hot injection method and the synthesis of core-shell nanoparticles will be carried out. As described in the previous section, the removal of stabilizers without changing the properties of the colloids is challenging. Therefore different procedures will be examined. Finally, the catalysts will be tested for the ethylene epoxidation and dry reforming of methane.

Analysis of the industrial ethylene epoxidation catalyst by electron microscopy reveals a broad particle size distribution ranging from a few to several hundred nanometers. In chapter 2, the influence of silver particle size for the ethene epoxidation will be examined. Detailed analysis of the colloid synthesis, the supporting on α -alumina including stabilizer removal and catalytic testing will be given. Based on these results the role of particles with different sizes and the effect on the mechanism will be discussed.

Addition of a promoter package increases the selectivity to ethylene epoxide significantly. Sulfur is one of the promoters that could be the key for understanding the different selectivity and activity compared to the unpromoted catalyst. In chapter 3, the synthesis and characterization of silver-silver sulfide core-shell particles will be described. Furthermore, the role of the sulfur oxidation state for the catalytic reaction will be discussed.

The dry reforming of methane converts two greenhouse gases, methane and carbon dioxide, to synthesis gas. The challenge to make this process viable is to find a cost efficient and stable catalyst. In this regard, nickel is favourable to be the main metal in an industrial catalyst. In chapter 4, the synthesis and characterization of nickel based manganese oxide core-shell nanoparticles will be described. By using core-shell particles a higher contact area between active metal and promoting metal oxide can be obtained. During the DRM reaction, coke formation on the catalyst is a major

deactivation source. In this regard, promoter effects by manganese and phosphorous will be discussed.

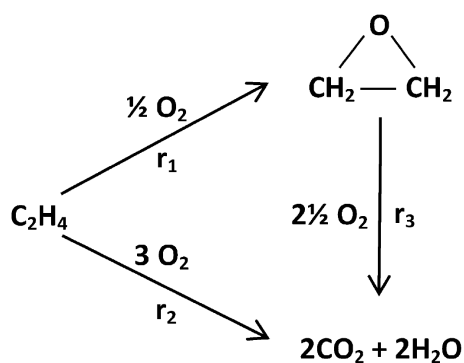
Nanostructured ordered metal oxides gain popularity as supports for heterogeneous catalysis. For DRM, zirconium oxide is viewed as a promoter for nickel based catalysts. Due to the high oxygen mobility carbon depositions can be burned off, which mitigates deactivation caused by coke formation. In chapter 5, the synthesis and characterization of a hard templated zirconia is described. Furthermore, it is used as support for nickel nanoparticles. The material is tested for DRM reaction and the performance is directly compared to alumina supported nickel catalyst.

For each described chapter an introduction to the respective topic will be given. Then, the experimental work is introduced followed by description and discussion of the obtained results and a summary. After these four main chapters a general summary with concluding results and discussion as well as a short outlook will be given.

2. Particle Size Study with Colloid-based Model Catalysts for Ethylene Epoxidation

2.1. Introduction

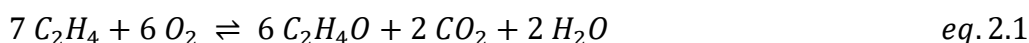
The oxidation of ethylene to ethylene oxide over a silver catalyst is one of the major petrochemical processes with a production over 30 million tons in 2016.^[75] Ethylene oxide is directly used as a disinfectant and sterilizer, but is industrially more important as an intermediate for glycols, which are mainly used as antifreeze and for polyester production. Since the discovery of this process by Lefort in 1931, the main focus was to improve the selectivity of the silver catalyst, e.g. by adding promoters, for economic and technical reasons.^[76] Nowadays, ethylene is converted to ethylene oxide over an α -aluminium oxide supported silver catalyst with a promoter package including sulfur, rhenium and caesium among others. The α -alumina support contains very few acidic hydroxyl groups on the surface. These groups are responsible for an unwanted isomerization of ethylene oxide to acetaldehyde which undergoes fast total oxidation to water and carbon dioxide (scheme 2.1).^[77] Therefore, only low surface area supports like α -aluminium oxide are viable in this process. Alumina supported silver catalysts only show a selectivity of 50 % towards ethylene oxide while promoters increase the selectivity to around 90 % at around 40 % oxygen conversion.^[78,79]



Scheme 2.1. Scheme for ethylene epoxidation. Ethylene can either directly react to ethylene epoxide (r_1) or undergo total oxidation to water and carbon dioxide (r_2). Furthermore, under reaction conditions ethylene epoxide can also undergo total oxidation (r_3) after isomerization to acetaldehyde. Adopted from ^[80].

The role of the promoters as well as the overall mechanism of the reaction is still under debate in literature.^{[81][82]} A chlorine species, e.g. ethylene chloride, is usually

added in the feed at concentrations of only a few ppm, because larger concentrations would lead to an overpromotion, thus acting as catalyst poison. Other promoters are added to the impregnation solution during synthesis. For a long time it has been suggested that molecular adsorbed oxygen is the active phase.^[83] After molecular adsorbed oxygen reacts with adsorbed ethylene, atomic oxygen remains at the surface (equation 2.1). With atomic oxygen, the total oxidation pathway is favored. The main promoter, a chlorine species, acts as an inhibitor and blocks off atomic oxygen. With this mechanism, the selectivity with optimal inhibitory effect of the chlorine species would be limited at 6/7 (85.7%).



Nowadays, selectivities around 90% are achieved, so this pathway is either wrong or cannot be the only mechanism. More recent publications show that atomic surface oxygen can be subdivided into two species: Weakly bound electrophilic oxygen $O^{\delta+}$ selectively oxidizes ethylene to ethylene oxide, whereas strongly bonded nucleophilic oxygen $O^{\delta-}$ leads to the total combustion of ethylene.^[84–86] However, nucleophilic oxygen is also accounted for adsorption of ethylene by formation of π -complexes.^[87] Thus, both oxygen species are required for ethylene epoxidation. Rocha et al. showed by in situ near-ambient x-ray photoelectron spectroscopy (XPS) studies that dosing of chlorine changes the ratio of electrophilic to nucleophilic oxygen. Subsequently, the selectivity towards ethylene oxide increases with time on stream.^[88] Another particularity is the oxygen-silver interaction. Oxygen can diffuse through the silver bulk. The formed subsurface oxygen can then diffuse to the surface and substitute other surface oxygen species, thereby changing the electronic properties at the silver surface.^[89–92]

Linic et al. have postulated an oxometalloycycle (OMC) intermediate formed on the silver surface from ethylene and an oxygen atom.^[93,94] Depending on the bond angle, ethylene oxide or acetaldehyde can be formed from this intermediate. This model could explain the 50 % selectivity for the unpromoted catalyst. The promoter effect of the chlorine species is still unclear for this model. Torres et al. suggest that adsorbed chlorine species in the immediate vicinity of the OMC intermediate lowers the energy barrier to ethylene oxide,^[95] while Van Santen et al. suggest that chlorine species block oxygen vacancies and thus, the OMC intermediate is not formed in the first place. The latter group postulates two existing pathways, one through the OMC

intermediate and one direct epoxidation route. With high oxygen coverage and chlorine promotion the latter route will be favoured.^[81]

Recent publications suggest that the research for the active/selective site will continue in future.^[96,97] The ethylene epoxidation over silver-oxygen catalysts is a good example for the “pressure gap” in catalysis research as in situ analytics are often used under below ambient pressure conditions while the industrial process is run at 16 bar.^[98] Ultimately, an uncertainty will always lie within literature results based on experiments conducted under reduced pressure and their transfer to the industrial process.

Besides promoters and mechanisms, another topic which is still under debate in literature is the influence of the particle size. In general, smaller particle sizes are preferred, because this leads to more surface area per mass and thus, more active sites in comparison to bigger particles. Nevertheless, smaller is not always better as following examples will show. To examine particle size effects, model catalysts with narrow particle size distributions can be prepared and tested for the regarded reaction. There are many examples in literature for so called particle size studies. Bezemer et al. examined cobalt particle size effects for the Fischer-Tropsch reaction (figure 2.1A).^[99] Among particle sizes from 2.6 to 27 nm, the highest activity per mass cobalt was observed for cobalt particles with 6 nm diameter. However, for particles bigger than 6 nm the TOF does not change. Also the selectivity to desired higher alkanes is decreasing with decreasing particle size. The authors propose that for the variety of single steps needed in the Fischer-Tropsch reaction a minimum of 6 nm particles is beneficial for stabilizing active sites.

A particle size study for the carbon monoxide oxidation was conducted by Valden et al. (figure 2.1B).^[100] In this study, supported gold nanoparticles with particle diameters from 1-6 nm on titania were examined regarding their turnover frequency. Gold particles with sizes of 3-3.5 nm exhibited the highest conversion. The authors explain these results with electronic effects, more specifically, the band gap difference. The highest activity is observed for two-atom thick clusters, whereas band gaps for clusters with one-atom layers are already too large.

An example for size-dependant selectivity changes is the pyrrole hydrogenation. Kuhn et al. synthesized 0.8-5 nm platinum colloids and supported them on SBA-

15.^[101] As can be seen in figure 2.1.C the selectivity to *n*-butylamine and *n*-butane is increasing with bigger particle diameter. The authors propose that the ring-opening is favoured for bigger particles due to electronic properties. Smaller particles are more electron deficient and thus, cannot stabilize the formation of the electron rich nitrogen of the *n*-butylamine. Summarizing, these results show that smaller particle size does not always mean better catalytic performance. Furthermore, each catalytic process is unique, so the reason for particle size effects can be diverse.

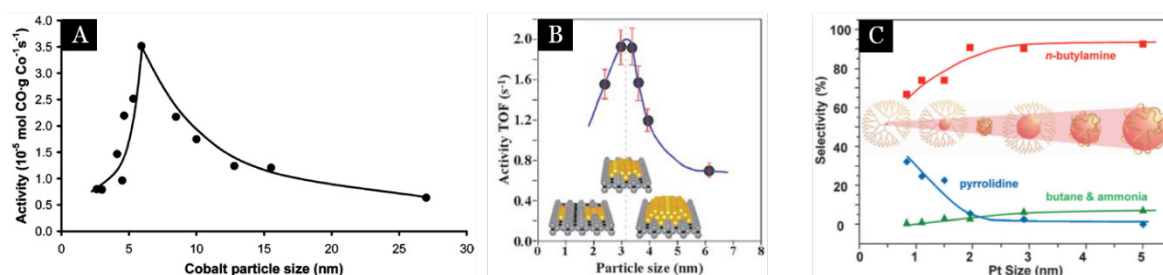


Figure 2.1. Examples for Particle size studies in the literature. A: The influence of different cobalt particles size regarding the activity for the Fischer-Tropsch process. The highest activity is observed at 6 nm. B: Turnover frequencies for different sized gold nanoparticles on ceria for the carbon monoxide oxidation. The highest TOF is observed at around 3 nm. C: Selectivity influence for different sized platinum colloids in the pyrrole hydrogenation. Smaller particles give higher amounts of pyrrolidone and lower amounts of *n*-butylamine compared to bigger particles. Adopted from ^[99–101].

In case of the ethylene epoxidation catalyst, the impregnation of the silver precursor and subsequent calcination yields mainly large particles (> 20 nm) that show the desired activity and selectivity towards ethylene oxide, while small particles (< 10 nm) show less selectivity for ethylene oxide.^[102] Thus, controlling the silver particle size could be crucial regarding the catalytical performance. Based on literature results, an optimal size domain regarding the selectivity can be found between 40 and 60 nm.^[103–107] However, in these reports the particle size was varied by silver loading. With higher silver concentrations in the impregnation solution bigger particles are formed on the final catalyst after calcination. This method can lead to performance changing effects independent of the particle size. The results in these papers were calculated per silver mass despite significant difference in metal loading and ethylene conversion.

Van den Reijen et al. also conducted a particle size study by supporting silver on α -alumina and changing the particle size by gas post treatment in hydrogen, nitrogen

or synthetic air.^[108] They concluded that the optimal size of the silver particles is indeed around 60 nm, while the selectivity is not influenced by particle sizes when measured at constant conversion. It was suggested that oxygen is part of the active site. For smaller particles, only few sites for adsorbing oxygen are present and thus, the activity of these catalyst is lower in comparison to catalysts with bigger particles according to the group. The active site for conversion to ethylene oxide should then be the same for all particle sizes, hence the particle size independence regarding selectivity. All conducted particle size studies were done via the impregnation method. However, by this method smaller particles (< 10 nm) cannot be excluded, although this is essential to distinguish between small and big particles (> 20 nm) and draw conclusions about the mechanism. Furthermore, synthesis by dry impregnation on low surface area supports like α -alumina usually leads to broad particle size distributions.

In our study, we focus on a colloidal approach to synthesize silver nanoparticles with narrow particle size distributions and support them in a structure retaining manner. To compare particle sizes, silver loading on the support should be similar. After stabilizer removal, the samples with different particle sizes were tested for ethylene epoxidation. For establishing an structure-reactivity relationship the catalysts were thoroughly characterized before and after the catalytic reaction.

2.2. Experimental

2.2.1. Standard Procedure for Silver Nanoparticle Synthesis with Single Injection Method

The silver colloid synthesis is based on literature publication, but modified for higher product output.^[109]

In a 500-mL round bottom flask tannic acid (616 mg, 0.36 mmol) was dissolved in H₂O (234 mL, HPLC grade). With an pH adjusting reagent (either potassium carbonate or ammonium hydroxide) the pH was set to desired values. The solution was stirred at 1400 rpm and rt. To the stirring solution a solution of silver nitrate in water (51 mg in 6 mL, HPLC grade) was added with an Eppendorff pipette as fast as possible. The reaction mixture changed color from bright yellow to dark orange. The stirring time for the color change was strongly dependent on the set pH value. For higher pH values (> 6.8) the color change occurred immediately. For samples with lower pH values color changed to green-grey. After 6 h stirring the reaction mixture was centrifuged at 9000 rpm for 30 minutes. The supernatant liquid was decanted and the remaining silver nanoparticles were dispersed in HPLC water (100 mL).

2.2.2. Standard Procedure for Silver Nanoparticle Synthesis with Multiple Injection Method

In a 50 mL round-bottom flask, tannic acid (1.7 mg, 0.001 mmol) was dissolved in HPLC water (19.5 mL). Then the pH was set to 7.0 with a potassium carbonate solution (0.5 M) and the solution was stirred with 400 rpm at 30 °C. To that stirring solution aqueous silver nitrate solution (2 mM, 0.5 mL) was added and the yellow solution was stirred for one hour. The solution was cooled down to 20 °C and then aqueous solutions of tannic acid (2 mM, 0.5 mL, pH=5.5) and silver nitrate (20 mM, 0.5 mL) were added simultaneously. The reaction mixture was heated up to 30 °C and stirred for 2 h. These last two steps were then repeated up to seven times before stirring the reaction mixture overnight. The dispersion was then centrifuged, the supernatant liquid was decanted and the solid was redispersed in HPLC water.

2.2.3. Synthesis of > 100 nm Silver Nanoparticles with Multiple Injection Method

The silver particles of at least 100 nm were synthesized according to the literature.^[110]

For injection solution 1, tannic acid (85.0 mg, 0.05 mmol) was dissolved in H₂O (20.0 mL, HPLC grade). For injection solution 2, trisodium citrate (129 mg, 0.50 mmol) was dissolved in H₂O (20.0 mL, HPLC grade). For injection solution 3, silver nitrate (85.0 mg, 0.05 mmol) was dissolved in H₂O (20.0 mL, HPLC grade).

In a 100-mL round bottom flask, a solution of tannic acid (17.0 mg, 0.01 mmol) was dissolved in H₂O (100 mL, HPLC grade). Trisodiumcitrate (129 mg, 0.5 mmol) was added to the solution, then the mixture was refluxed for 15 min. After cooling down to 90°C, 16.5 ml of the reaction volume was removed. In intervals of 1 min each, H₂O (13.5 mL, HPLC grade), injection solution 2 (1 mL, 25 mM), injection solution 1 (3 mL, 2.5 mM) and injection solution 3 (2 mL, 25 mM) were added into the reaction vessel. Then, the reaction solution was stirred for 35 min at 90 °C. This procedure was repeated ten times.

2.2.4. Supporting of Tannic Acid Capped Silver Nanoparticles on α -Alumina

Tannic acid capped silver nanoparticles in aqueous solution (200 mL, approx. 65 mg Ag) were mixed with alumina pellets (3.91 g, from BASF). The suspension was stirred for 30 min and then the water was removed under reduced pressure. An orange solid was obtained after the first impregnation. The procedure was repeated two more times with the same impregnated alumina pellets. The color changed from orange to grey. For the catalytic test, the pellets were crushed in sieve fraction of 250-315 μ m.

2.2.5. Catalytic Screening

Catalytic screening was carried out at the hte GmbH in Heidelberg. For each sample 1 mL was used in a sieve fraction of 250-315 μ m. The run protocol is given in table 2.1.

Table 2.1. Run protocol for ethylene epoxidation catalysts screening at hte.

Phase	Runtime [h]	Temp. [°C]	Ethen IN [vol.%]	O2-IN [vol.%]	Ethylene chloride-IN [ppm]	Ar-IN [vol.%]
1	16	165	35	7	0	5
2	16	175	35	7	0	5
3	16	200	35	7	0	5
4	16	215	35	7	0	5
5	16	230	35	7	0	5
6	16	245	35	7	0	5
7	16	200	35	7	0	5
8	16	245	35	7	0.6	5
9	16	230	35	7	0.6	5
10	16	215	35	7	0.6	5
11	5.33	260	35	7	0	5
12	21	260	35	7	0.6	5
13	16	260	35	7	1.2	5
14	16	245	35	7	1.2	5
15	16	230	35	7	1.2	5
16	16	215	35	7	1.2	5
17	32	260	35	7	0	5
18	16	245	35	7	0	5

2.2.6. Colloids and Catalysts Characterization

Transmission electron microscopy (TEM) was carried out with a FEI Tecnai G² 20 S-TWIN with an equipped r-TEM SUTW Detector for electron dispersive x-ray spectroscopy. 25 μ L of sample (stabilized silver particles in water) were placed on a carbon coated copper grid. Then, the grid was dried at rt before put on the sample holder.

UV-VIS measurements were conducted with a Cary 300 UV-VIS from Agilent. The samples were diluted with water (HPLC grade) before measurement. The same water source was used as a reference. For standard measurements wavelengths ranging from 800 to 200 nm with a speed of 20 nm/s were scanned.

Scanning electron microscopy (SEM) measurements were performed with a Hitachi FEG-SEM model SU8030. The solid samples were placed on double-sided adhesive carbon pads before measurement.

Infrared spectroscopy (IR) measurements were carried out with a Bruker ALPHA FT-IR spectrometer by attenuated total reflection (ATR). The solid samples

were placed directly under the diamond ATR crystal. For each sample wavenumber in the range from 4000 cm^{-1} to 400 cm^{-1} were measured.

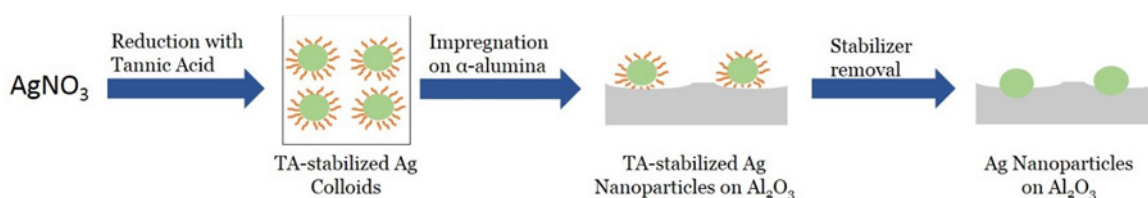
Elemental analyses was conducted with a Thermo Finnigan FlashEA 1112 Organic Elemental Analyzer for carbon quantification and by ICP-OES with a Varian 715 Emission Spectrometer for silver quantification. Carbon quantification was performed with 1-2 mg of sample for each measurement. Usually, two measurements for each sample were carried out. Digestion of ICP-OES samples was done by stirring the sample (10-20 mg) in conc. nitric acid (10 mL) for 16 h. After the solid settled, the supernatant liquid (5 mL) was diluted 1:1 with water (HPLC grade).

Temperature programmed oxidation (TPO) coupled with a mass spectrometer (MS) were conducted with MicrotracBEL BelCat II setup and a Pfeiffer Vacuum QMG 220 mass spectrometer. The exhaust of the BelCat II setup was connected to the MS with a capillary. The sample was fixed with glass wool in a quartz glass setup and then put into the BelCat II setup. For the TPO measurement 131 mg of sample were used. The gas mixture was 10 % O_2 in He with a total flow of 50 mL/min. The temperature was increased from 50 $^\circ\text{C}$ to 800 $^\circ\text{C}$ with 2 K/min.

X-ray photoelectron spectroscopy (XPS) was measured on K-Alpha^{TM+} X-ray Photoelectron Spectrometer System from Thermo Scientific. The x-ray source was Al- $\text{K}\alpha$ -radiation. For the measurement, the solid samples were pressed and put on carbon taps which were put in the sample holder for measurement. Survey spectra were run in the binding energy range of 0-1000 eV and high-resolution spectra of C1s, O1s and Ag3d_{5/2} were collected.

2.3. Results

To examine the silver particle size influence, a particle size study was conducted. To our knowledge, all particle size studies for the ethylene epoxidation reaction in literature are based on dry impregnation, where the existence of small nanoparticles beside larger particles cannot be excluded. To give unambiguous statements about particle size influence more defined catalysts are needed. This study was based on colloidal silver nanoparticles. By this method, narrow particle size distributions can be obtained and furthermore, the presence of small nanoparticles (< 10 nm) can be excluded. After the synthesis of silver nanoparticles, the colloids are supported on α -alumina. Subsequent stabilizer removal yields the final catalyst. The synthesis route of the catalyst is summarized in scheme 2.2.



Scheme 2.2. Scheme for the preparation of a colloid-based catalyst. First, the precursor is reduced in presence of a stabilizer. Then, colloids are supported via wet impregnation. The last step is the removal of the stabilizer.

2.3.1. Colloidal Silver Synthesis

In general, the size of nanoparticles can be tuned by various synthesis parameters. Based on the work of Cao et al. the synthesis of silver nanoparticle with silver nitrate as the precursor and tannic acid as the stabilizer, the pH value is the most important parameter.^[109] Tannic acid is chosen as it stabilizes particles by electronic and steric interaction. Hence, final particle size distributions are more narrow in comparison to widely used citric acid. By changing the pH, a range of particle sizes can be synthesized. The reason is that the reducing power of the tannic acid is decreased as the pH is lowered. More hydroxyl groups become uncharged, which makes the electron transfer to the silver precursor more difficult. This results in a nucleation of fewer particles compared to reduction at a higher pH. After the nucleation phase, the reduced precursor will grow at the already present silver particles as heterogeneous nucleation is favoured according to the nucleation theory resulting in bigger particles.^[111,112]

Another parameter to tune the particle size is the precursor/stabilizer ratio. With higher ratios particles are less stabilized and can grow to bigger sizes. However, in this work changing the precursor/stabilizer had almost no impact on the final particle size and will not be discussed.

In this chapter, two ways of silver nanoparticle synthesis are introduced. First, the single injection method (SIM) in which a high concentration of silver precursor and reducing/stabilizing agent are present. This leads to fast nucleation and thus, to formation of rather small nanoparticles. The other method is the multiple injection method (MIM). By using very low concentrations during the first injection silver seeds are formed. Additional injections lead to heterogeneous nucleation on the already present seeds. With this method, rather big nanoparticles, e.g. over 100 nm in diameter, can be obtained.

First, the SIM was tested to examine which particle size can be reached, how narrow the particle size distribution and if the exclusion of small nanoparticles is successful by this method.

UV-Vis Analysis

Silver particles have unique optical properties due to the strong interaction with light when excited with a certain wave length. The stimulation by light leads to a resonant oscillation of the conducting electrons at the metal surface. This is known as the plasmon surface resonance.^[113] Depending on the size of the silver particles, the absorption maximum in the visible spectrum changes as increasing particle sizes lead to a red-shift. At diameters greater than 80 nm, a second peak becomes visible at a shorter wavelength than the primary peak. This secondary peak is due to a quadrupole resonance that has a different electron oscillation pattern than the primary dipole resonance. The peak wavelength, the peak width and the effect of the secondary resonances yield a unique spectral fingerprint for a plasmonic nanoparticle with a specific size. According to the Mie theory the dielectric constant of the medium plays a decisive role for the plasmon resonance.^[114] Tannic acid, which is used as the capping agent in this work, has a dielectric constant one magnitude higher than citrate and seven magnitudes higher than air. Therefore the relation between UV-VIS spectra and particle size can be easier evaluated so that the position of the maxima in UV-VIS spectra will be used as the first analytical tool. In figure 2.2, the UV

spectra of colloidal silver nanoparticles synthesized at different pH values are shown. For comparison, a reference spectra from the Sigma Aldrich website is given. A red-shift for samples synthesized at lower pH values can be seen. Furthermore, the peak shape broadens with bigger particles sizes. A sharper peak shape implies a more narrow particle size distribution. At pH 6.8 the peak maximum is at 414 nm, for pH 5.9 at 441 nm. Comparing with the reference spectra this indicates particle sizes of around 30 nm for the pH 6.8 sample and around 60 nm for the pH 5.9 sample.

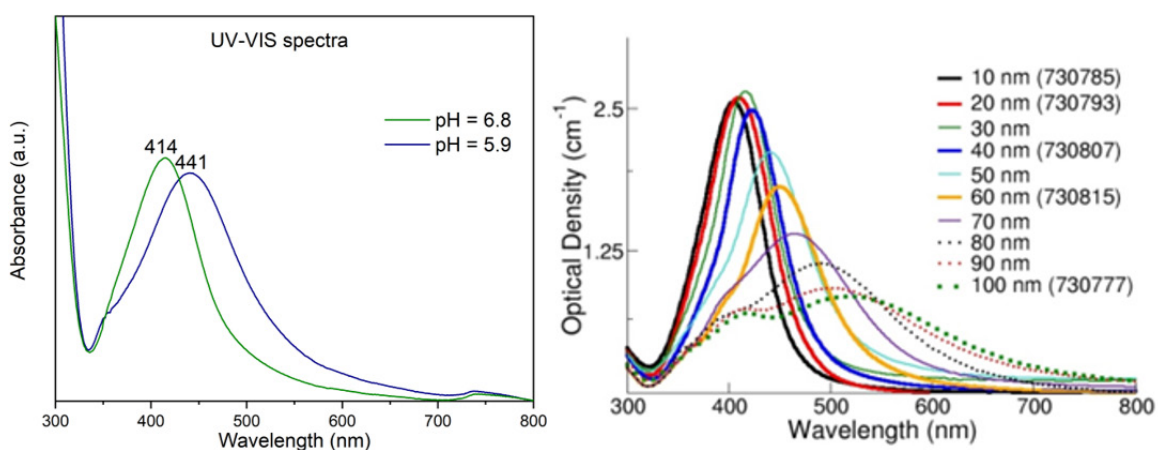


Figure 2.2. UV-VIS measurements of the tannic acid stabilized silver colloids at different reaction pH values. The sample synthesized at higher pH value absorbs at higher wave lengths (left). The Sigma Aldrich reference diagram shows assignment of absorption maxima to particle size. Based on the reference, the pH 6.8 sample is around 30 nm and the pH 5.9 sample around 60 nm in size. The strong increase in absorbance in the UV region could originate from the tannic acid stabilizer. Right graph adopted from sigmaaldrich.com/technical-document/articles/materials-science/nano-material/silver-nanoparticles.html.

TEM Analysis

To evaluate the size and shape of the nanoparticles, TEM images of both samples were taken (figure 2.3). According to the UV-VIS results, the particle size is increasing with lower pH values. From the TEM images a particle size distribution with the imageJ software was created. The nanosizer plugin was used for at least 100 particles of each sample. For all measured particles an average (arithmetic mean) size was determined. The particle size distribution broadens with bigger particle sizes. While at pH 6.8 the average particle size is $26 \text{ nm} \pm 4 \text{ nm}$, at a pH of 5.9 the average particle size is $58 \text{ nm} \pm 7 \text{ nm}$. TEM and UV-VIS analysis show very similar results, if silver particle sizes from UV-VIS are derived from the Sigma-Aldrich reference.

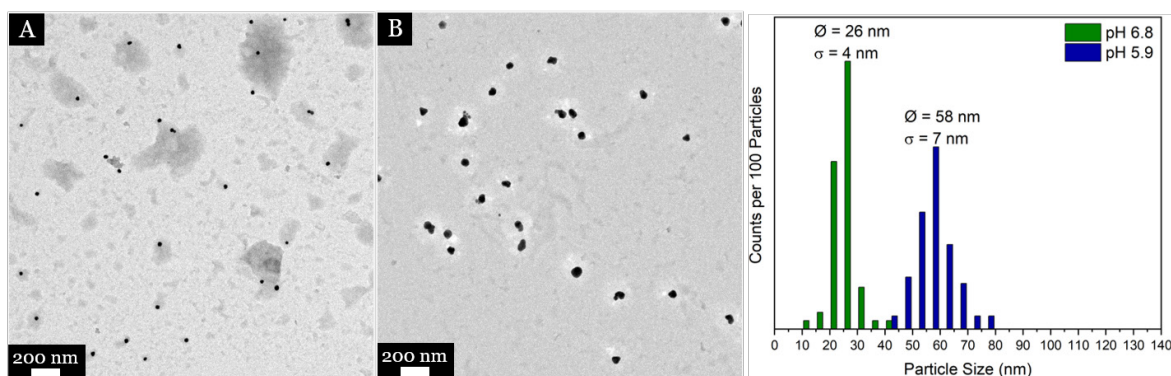


Figure 2.3. TEM images of the tannic acid stabilized silver colloids at different reaction pH values (A,B) and their particle size distribution (C). The images show a homogeneous particle size distribution. The TEM measurement is in accordance with the UV-VIS results.

Multiple Injection Method

With the described method, the synthesis of bigger nanoparticles (> 70 nm) would require an even lower pH value. However, at low pH values the reduction of the silver precursor is very slow and thus, many nucleation events could occur, leading to broad particle size distributions. A method to achieve bigger particle sizes with narrow particle size distributions is the above described multiple injection method. By using low concentrated solutions initially, the particle growth of the silver nanoparticles can be controlled by consecutively adding silver precursor and reducing agent. The growth can be monitored by color (figure 2.4).

The final product was examined with TEM which shows an average particle size of $80 \text{ nm} \pm 10 \text{ nm}$ (figure 2.5). Besides longer reaction time, small silver amounts per run were another drawback of the multiple injection method. Furthermore, the growth after multiple reactions was very limited, so that particle bigger than 100 nm could not be synthesized.

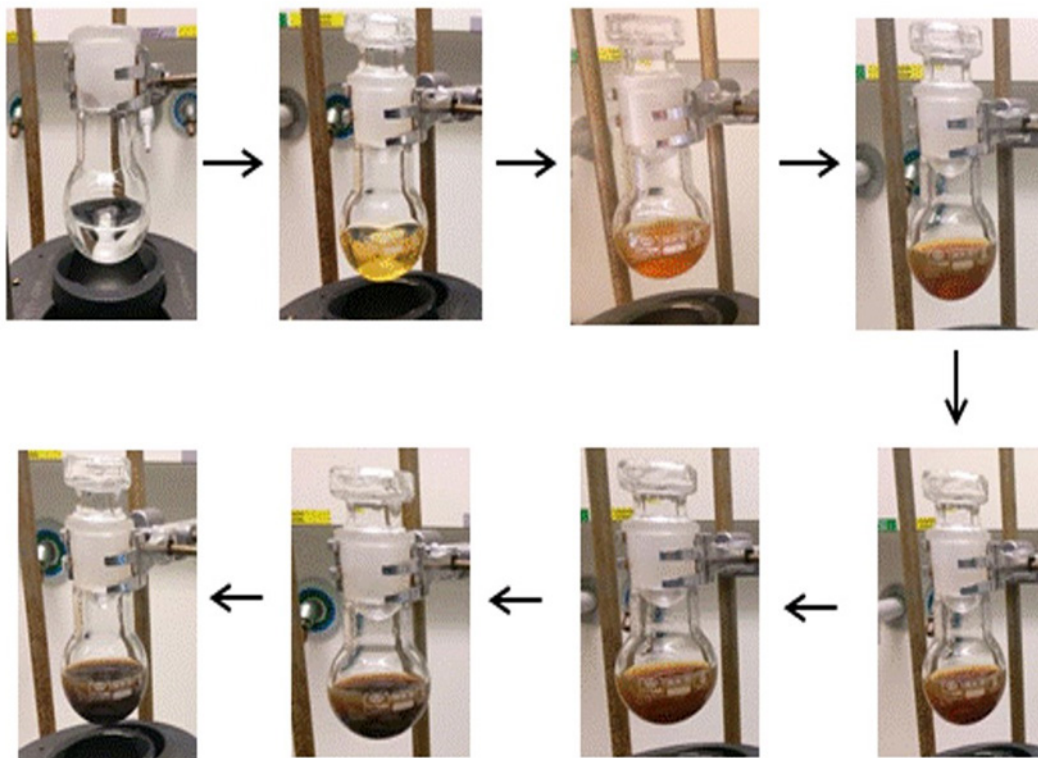


Figure 2.4. Images of the stepwise multiple injection synthesis. After each injection a color change can be observed. With each injection silver nitrate and tannic acid are added. Color changed from yellow to brown.

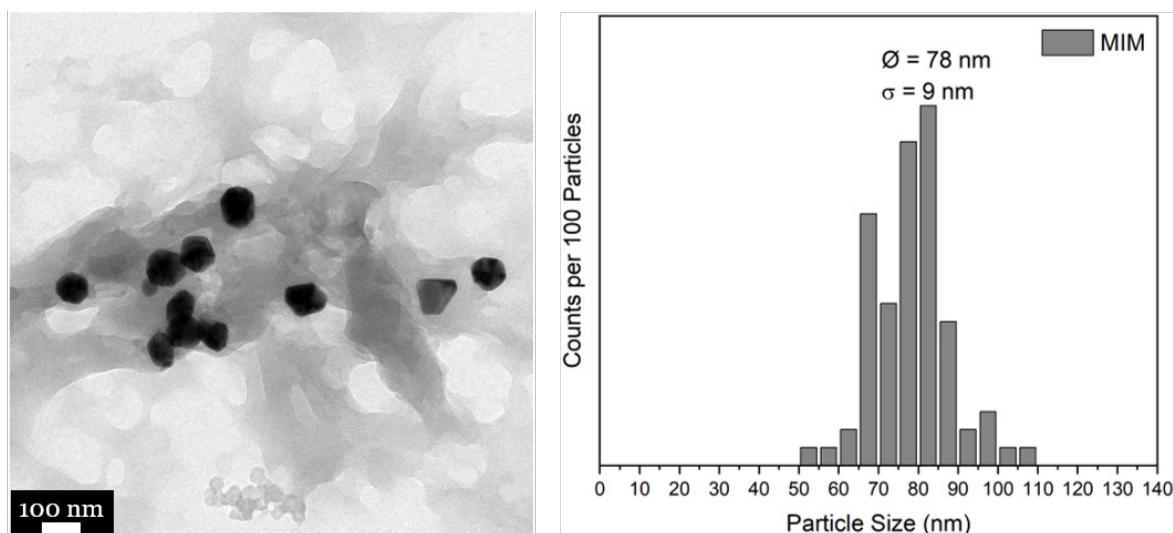


Figure 2.5. TEM images of stabilized silver colloids synthesized by multiple injection method. The images show a narrow particle size distribution with an average diameter of 78 nm.

To generate bigger nanoparticles, another method based on the paper by Bastus et al. was carried out.^[110] Here, additionally to the tannic acid, citrate is used as the stabilizing/reducing agent. By this, the electrostatic force of citrate ions helps to stabilize the silver particles in addition to the steric and electrostatic stabilization by tannic acid. Figure 2.6 shows TEM images and the connected particle size distributions of this citrate added MIM. The synthesis of silver nanoparticles >100 nm was successful, however the silver amount per run was even lower than in the original MIM synthesis.

Samples with the single injection method had higher product amounts per run and were easier to upscale in comparison to both MIMs. With the MIM methods bigger particles could be synthesized.

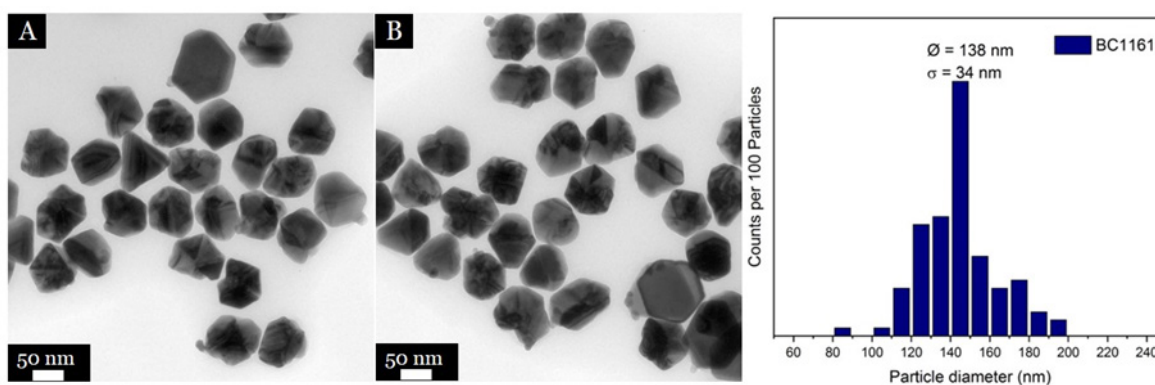


Figure 2.6. TEM images of stabilized silver colloids synthesized by citrate added multiple injection method. The images show a narrow particle size distribution but also some irregular shaped particles.

To produce enough catalyst material for a screening test, the nanoparticle synthesis had to be upscaled, which is challenging due to different nucleation and growth behavior when the reaction volume and/or concentrations are changed.^[115,116] Increasing the concentration could lead to destabilization of the nanoparticles and thus, partial particle agglomeration. Therefore, the amount of all educts was upscaled in the same ratio. This led to smaller nanoparticle sizes, which was verified by UV-Vis. The reason for this could be an increase in reduction power of tannic acid as with each molecule tannic acid several reduction sites are added to the reaction mixture. To counteract this observation the pH value was increased from 6.8 to 6.9 for the smallest particles. This property was also used to make bigger nanoparticles (> 70 nm) with the single injection method. For this, a pH value of 6.0 was necessary. The UV-VIS spectra and TEM images are shown in figure 2.7.

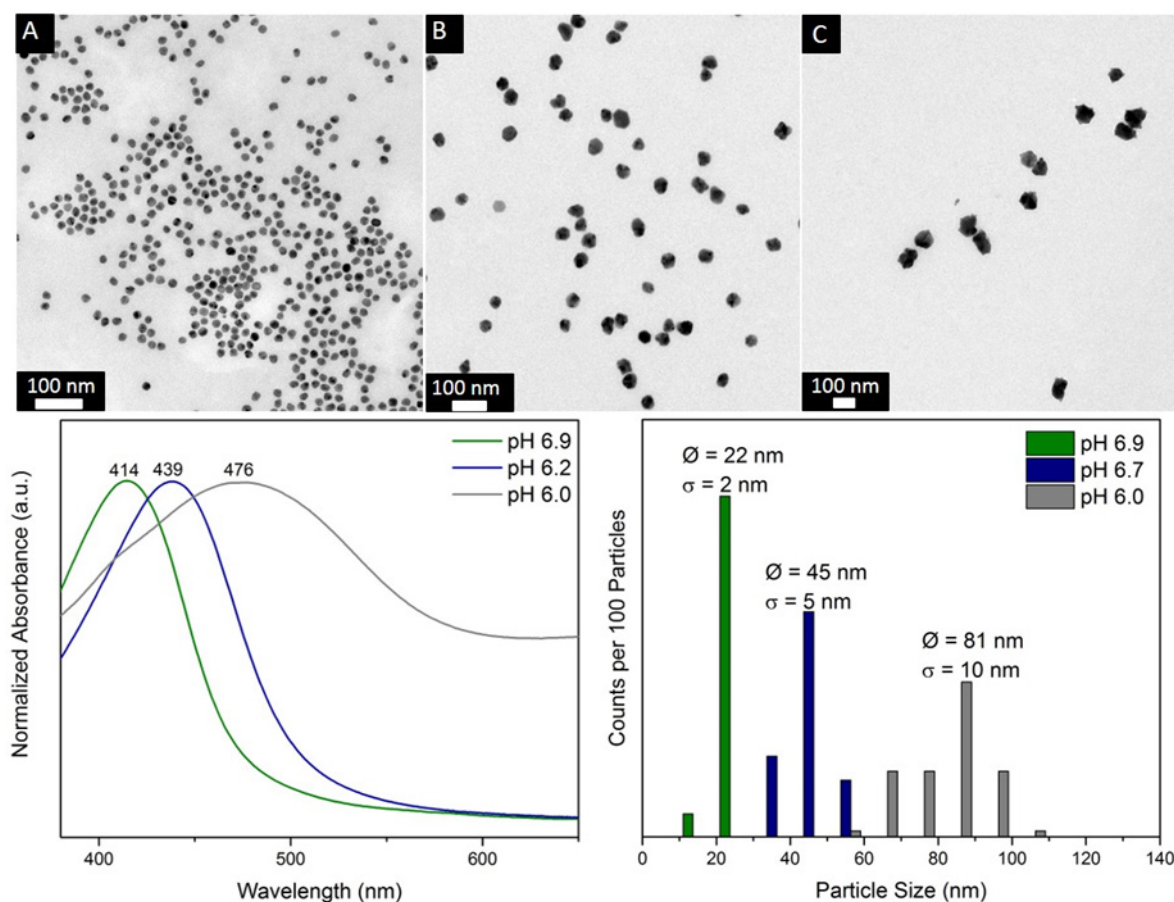


Figure 2.7. TEM and UV-VIS analysis for upscaled silver colloid synthesis. Smaller particles show a more narrow particle size distribution in comparison to bigger particles.

2.3.2. Impregnation and Removal of Stabilizer

For the catalytic test, it was decided to use three different particle sizes, namely 25 nm (synthesized by SIM), 55 nm (SIM) and 80 nm (MIM). For the 80 nm sample the multiple injection synthesis route was chosen, because the particle size distribution was more narrow in comparison to the single injection method (see figure 2.5 and 2.7). The next step according to scheme 2.1 was the supporting on cylindrical α -alumina pellets. Each pellet weighed around 400 mg. As α -alumina has a very small pore volume and the silver dispersions are not stable in small volumes, the wet impregnation method was chosen. The supporting step was carried out in a rotary evaporator. After rotating for 30 min at atmospheric pressure, the pressure was reduced to remove the water. A successful deposition was indicated by color change. To obtain a higher loading, the impregnation step was repeated two more times.

During pre-experiments it was found that a maximum silver loading on α -alumina is reached after few steps. The step number is depending on the concentration and volume of the impregnation dispersion. The reason for this finding is the low support metal interaction as corundum has very few functional groups which could anchor the silver particles. After all anchor points are occupied, particles on the surface and in dispersion are in an equilibrium so that the loading can not be increased anymore.

The next challenge is to remove the tannic acid stabilizer to free the silver surface for educt adsorption and subsequent conversion to products. For removing or exchanging stabilizers, many publications can be found in the literature, underlining the importance of this step for colloid-based materials and their applications.^[67–74] Common methods include heat treatment, UV-ozone treatment, reflux in aqueous solution, washing with certain reagents or exchange to other capping agents. For this project it is crucial to remove the stabilizer while suppressing the silver sintering. An uncontrolled sintering and thus, broadening of the particle size distributions, would weaken general conclusions about particle size influence.

Two different ways of heat treatments were compared. First, a calcination procedure similar to industrial synthesis conditions was tested, in which the sample is heated from room temperature to temperatures around 270–330 °C with fast heat rates of 30 K/min.^[117] The other heat treatment is based on a publication, where the samples were heated at higher temperatures but much shorter time, e.g. at 500 °C for 60 s.^[68] Additionally, an UV-ozone treatment, which is described as very mild in literature, was tested.^[70] To compare the three methods, one mother sample with the ca. 25 nm silver nanoparticles on alumina was prepared. The samples were analyzed qualitatively by IR-spectroscopy and quantitatively by elemental analysis. The structural composition of tannic acid is shown in figure 2.8.

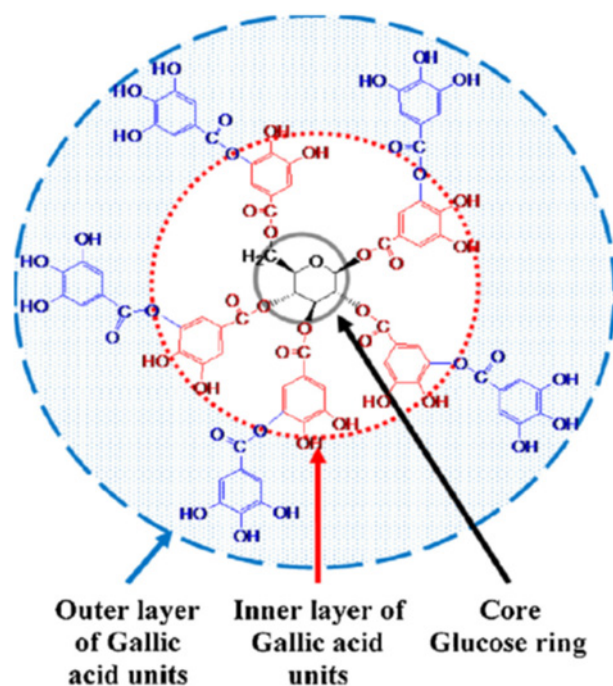


Figure 2.8. Tannic acid structure with two layers of gallic acid units and a glucose core ring. Gallic acid units can also decompose as pyrogallol and carbon dioxide. Adopted from ^[118].

To examine the decomposition behavior of tannic acid, a temperature programmed oxidation coupled with a mass spectrometer (TPO-MS) experiment was carried out (figure 2.9). For the experiment the sample was fixed with quartz wool in a BelCat II sample cell. In air flow (20 % O₂ in N₂, 50 mL/min) the freshly impregnated sample was heated with a ramp of 2 K/min to 800 °C. The experiment reveals two peaks and a shoulder. The onset of the first signal is at 155 °C, with the peak being measured at 182 °C. The onset of the second signal is difficult to determine, because it overlaps with the first signal. The peak position is at 248 °C and the shoulder is positioned at 311 °C. The decomposition event proceeds until ca. 400 °C. However, this is depending on the heat rate as with slower heat rates the decomposition would end at lower temperatures, whereas with higher heat rates the decomposition would end at higher temperatures. Xia et al. showed that oxidative degradation of tannic acid occurs under a stepwise bond dissociation.^[118] With increasing temperature the group observed following order regarding the leaving groups: First, the outer pyrogallols, then the carbon dioxides, the catechols, then again carbon dioxides and ultimately 2-methyltetrahydrofuran are removed. This explains the two signals for $m/z = 44$ deriving from carbon dioxide, whereas the shoulder signal at slightly higher temperatures could originate from a stronger interaction with the metal and/or support. The other m/z signal shown is $m/z = 52$, which is a fragment from

pyrogallol. However, this signal shows a poor signal to noise ratio. The reason for this could be the capillary between the TPO setup and MS setup, which was not heated and thus, non-volatile compounds (melting point for gallic acid: 253 °C; for pyrogallol: 135 °C) were possibly deposited on the capillary walls. Therefore, the decomposition was mainly monitored by $m/z = 44$ (carbon dioxide).

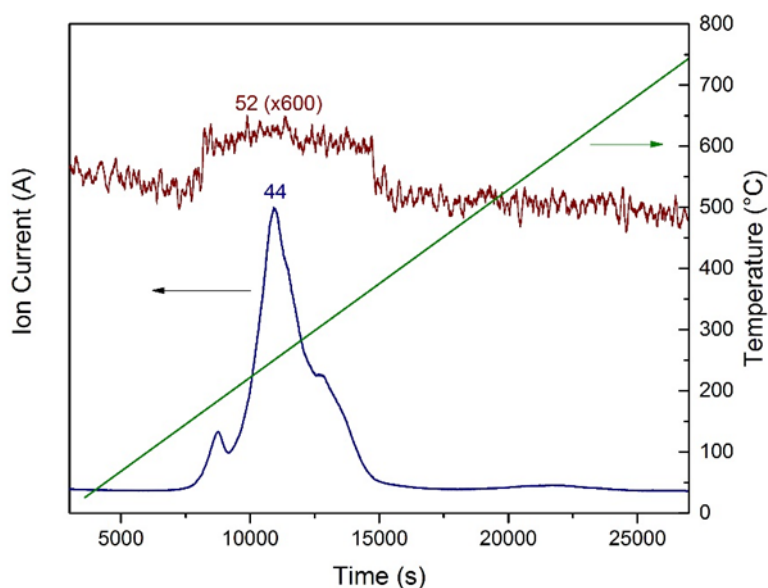


Figure 2.9. TPO-MS measurement of stabilized silver nanoparticles on alumina support. The temperature was increased by 2 K/min. The MS signal $m/z=44$ is shown, as carbon dioxide is the main decomposition product. The MS signal $m/z=52$ is a pyrogallol fragment.

Conventional Calcination Method

Four different calcination procedures similar to industrial synthesis conditions with a temperature range from 270 °C to 330 °C, a heat ramp of 30 K/min and a holding time of 5 min were tested.^[117] The calcination details are found in table 2.2. At first the materials were analyzed by IR spectroscopy to see if the tannic acid stabilizer was removed during the heat treatment. The IR spectra (figure 2.10) before and after heat treatment show mostly the disappearance of bands between 2000-1000 cm^{-1} , which were attributed to tannic acid. The band at approximately 1650 cm^{-1} can be assigned to the C=C stretch vibration and does not disappear. This could be a sign that graphitic carbon formed on the surface. While the other bands disappear, a new band at 1415 cm^{-1} is formed and most pronounced for sample D which was calcined at 330 °C. This band can be assigned to aromatic C=C stretch

vibrations, which either originate from graphitic carbon or tannic acid fragments. Beside this growing aromatic C=C band, there is no significant difference between each calcined sample.

Table 2.2. Four different calcination procedures used for tannic acid removal. Heat rate and holding time are similar to industrial synthesis conditions for silver based ethylene oxide catalysts.

Heat Treatment	Target temperature [°C]	Heat rate [K/min]	Holding time [min]
A	270	30	5
B	285	30	5
C	300	30	5
D	330	30	5

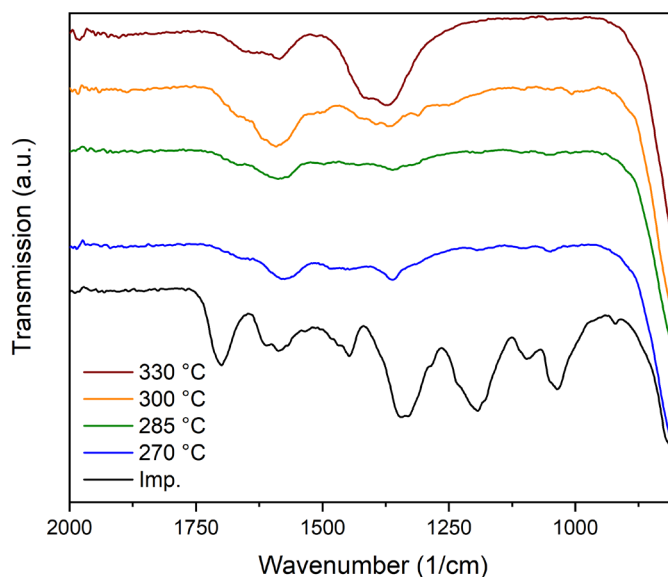


Figure 2.10. IR measurements after impregnation and after four different calcination procedures (see table 2.2 for more information). The measurement was conducted from 4000-400 cm^{-1} , but the relevant bands are in the represented range from 2000-800 cm^{-1} . Spectra were plotted with following offsets: Impregnated: -10 % ; 270 °C: -7 % ; 285 °C: +3 % ; 300 °C: +5 % ; 330 °C: +5 %.

To quantify the carbon amount left on the materials, elemental analysis was carried out. The results are shown in table 2.3. For each measurement of each sample the carbon amount is very fluctuating. This is due to supporting on the cylindrical α -alumina pellets. By this, only the outer surface was impregnated. After crushing the particles the powder is heterogeneous, so that the average of the three measurements was taken. Table 2.3 shows an expected decreasing carbon amount for the calcined samples with increased calcination temperature. There is no hydrogen left,

supporting the assumption based on the IR measurements that the tannic acid decomposed and only graphitic or similar elemental carbon species are left on the material. These carbon species, which are still present in a significant amount, could block active sites and thus, decrease the catalytic activity. Because of that only the sample D was examined with the SEM (figure 2.11). For comparison, the impregnated sample was also examined.

Table 2.3. Carbon and hydrogen (on average) amount as measured by elemental analysis for different calcination procedures. Average values were taken from three measurements of each sample.

Sample	Carbon 1 st measurement [%]	Carbon 2 nd measurement [%]	Carbon 3 rd measurement [%]	Hydrogen [%]	Carbon average [%]
Impregnated	4.83	6.16	5.89	0.25	5.63
A	1.71	1.74	1.73	0	1.73
B	1.83	1.04	1.54	0	1.47
C	1.35	0.97	1.51	0	1.28
D	0.29	0.53	0.37	0	0.40

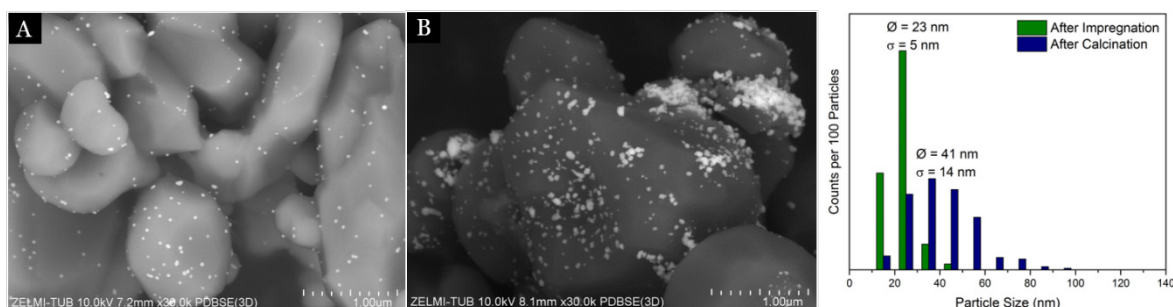


Figure 2.11. SEM images after the impregnation step (A) and after calcination procedure D (B). The particles grow during calcination from 23 to 41 nm on average and the PSD broadens.

After wet impregnation the silver particles are well distributed. Even when stuck together, single particles are well recognizable. After calcination at 330 °C the particle size distribution changes and there are more agglomerates, but single particles were still observable. Removing the stabilizer will always lead to particle growth because the surface energy of nanoparticles is too high. In the case of α -alumina as support there are almost no interactions with the support to stabilize the free surfaces of the silver particles, which enhances their tendency to sinter. With this method, a significant amount of carbon is still measurable, even at the highest temperature, where sintering of particles already started.

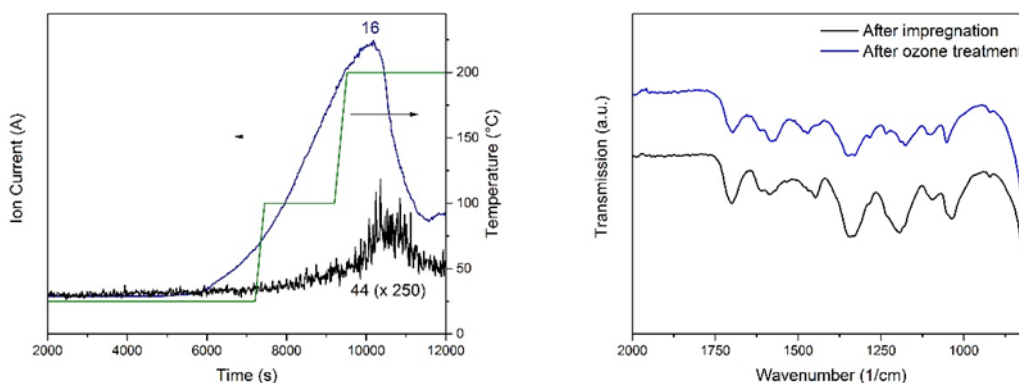
Ozone Experiment

Another method for removing tannic acid from the silver surface was the UV-ozone method (figure 2.12). Described as a very mild method, ozone can oxidize organic molecules at low temperatures ranging from rt to 110 °C.^[119–121] To generate ozone, oxygen is pumped through an ozone generator. Here, UV light converts part of the oxygen, usually 20-30 %, to ozone. The ozone experiment was conducted in the Bas-Cat ALD setup. The sample was filled in a quartz tube and fixed with glass wool. The total gas flow was 100 mL/min, with 80 % He and 20 % O₂/O₃. The conversion was monitored by mass spectrometry. After starting at room temperature, the temperature was increased to 100 °C and then to 200 °C. A signal for $m/z = 44$ which can be assigned to carbon dioxide was observed after increasing the temperature to 200 °C. When comparing to the TPO-MS decomposition (figure 2.9) this indicates, that the ozone treatment has no influence on the decomposition.

During the experiment, the sample's color changed from dark brown to bright grey, indicating a reaction. IR measurements showed only little changes to the tannic acid bands in comparison to the impregnated sample (figure 2.12). Most bands did not change so that a complete decomposition did not occur. However, some bands shifted and also intensities changed. The band at 1194 cm⁻¹ (impregnated sample) assigned to vibrational stretching -C-O- band shifted to lower wave numbers at 1175 cm⁻¹ after ozone treatment. Furthermore, the intensity of this band in comparison to other bands decreased. Since there are two layers of ester groups in the tannic acid molecule a reason for the change could be a partial decomposition in which only the outer layer was removed. The same could be possible for the shift of the -C=C- vibrational stretching band from 1446 cm⁻¹ to 1470 cm⁻¹ after ozone treatment. In this case the outer layer of pyrogallols was removed. Carbon quantification by elemental analysis (table 2.4) confirm a partial decomposition as about half of the carbon amount is still detected after ozone treatment. Adding up all outer pyrogallols and ester groups together will give exactly half of the tannic acid molar mass. With this method, the carbon amount is only halved and a significant part of the organic stabilizer is still blocking the silver surface.

Table 2.4. Carbon and hydrogen (on average) amount as measured by elemental analysis for ozone treatment. Average values were taken from two or three measurements of each sample.

Sample	Carbon 1 st measurement [%]	Carbon 2 nd measurement [%]	Carbon 3 rd measurement [%]	Hydrogen [%]	Carbon average [%]
Impregnated	4.83	6.16	5.89	0.25	5.63
Ozone	2.88	2.87	-	0	2.88

**Figure 2.12.** Left: Ozone decomposition as measured by MS. The MS signal $m/z=44$ is shown, as carbon dioxide is the main decomposition product. The decomposition starts between 100 °C and 200 °C with ozone treatment. Right: IR measurements after impregnation and after ozone treatment. Shifting of vibrational stretching bands at 1194 cm^{-1} (-C-O-) and 1446 cm^{-1} (aromatic -C=C-) is observed, which indicates a partial decomposition of the tannic acid stabilizer.

Short Heat Treatment

The third method carried out to remove the stabilizers was the short heat treatment. Here, the sample is put in a crucible and then introduced in a preheated oven for a short time at high temperature. The temperature needs to be high enough for a fast removal of tannic acid, so that the silver particles are not too long under conditions in which they are mobile on the support. For this project, a temperature of 600 °C was chosen. At this temperature fast removal of organic stabilizer is possible.^[68] After the reaction time, the sample is quenched by putting the crucible out of the oven to room temperature. For reproducibility, the same oven was used for all experiments. Furthermore, a marked stick was used to push the crucible to the exact same position for each experiment. The IR spectra for different reaction times is shown in figure 2.13. After 30 s at 600 °C, the tannic acid bands are disappearing. In the IR

spectra, no difference between the 30 s, 45 s and the 60 s samples is visible. To confirm this result an elemental analysis for each sample was conducted (table 2.5). Also here, a strong decrease in carbon amount is noticeable after 30 s. Still, a complete removal according to the measurement is only accomplished after 60 s. As the measurements have an error interval of 0.1 %, the values only give a tendency of the real carbon amount.

Table 2.5. Carbon amount as measured by elemental analysis for short heat treatment at 600 °C in a preheated oven. Average values were taken from two measurements of each sample. For all samples, no hydrogen was detected.

Sample	Carbon 1st measurement [%]	Carbon 2nd measurement [%]	Carbon average [%]
0s	0.59	0.57	0.58
15s	0.45	0.44	0.45
30s	0.03	0.06	0.05
45s	0.01	0.00	0.01
60s	0.00	0.00	0.00

To see how the particle size changed after the short heat treatment the 60 s sample was analyzed by SEM (figure 2.14). The silver sample shows a good distribution of particles. However, the particle size is partially varying due to sintering with particles up to 60 nm in diameter. Still, the sintering is better mitigated in comparison to the conventional calcination procedure. In addition, according to elemental analysis there is less carbon deposition on the sample which should be beneficial for the catalytic activity.

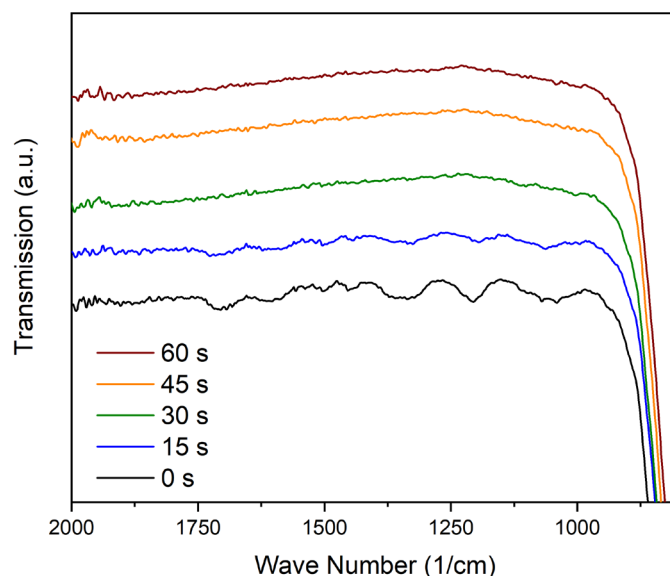


Figure 2.13. IR measurements after impregnation and after four different heat treatment times. The measurement was conducted from 4000–400 cm^{-1} , but the relevant bands are in the represented range from 2000–800 cm^{-1} . After 30 s the bands of the impregnated samples disappeared indicating tannic acid decomposition. Spectra were plotted with following offsets: 0 s : -8 % ; 15 s : -6 % ; 30 s : -4 % ; 45 s : -2 %.

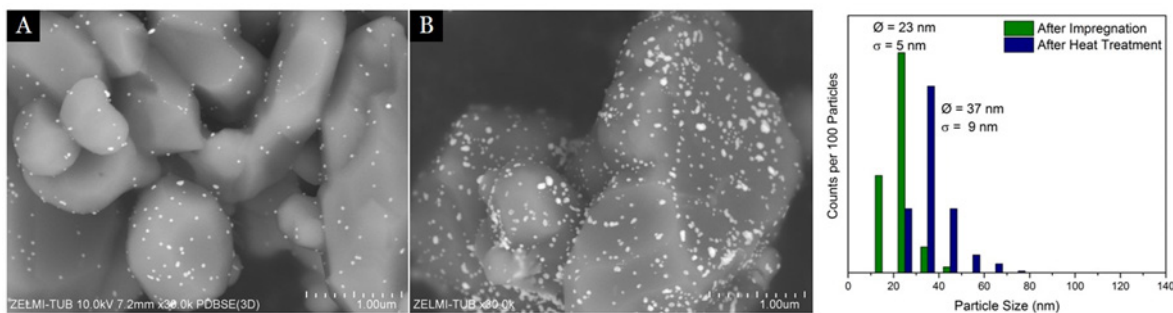


Figure 2.14. SEM images after the impregnation step and after 60 s short heat treatment. The particles grow during calcination from 23 to 37 nm on average and the PSD broadens. Still, this result for the stabilizer removal is better compared to the conventional calcination procedure.

Between the three tested methods, the short heat treatment method was chosen as the most effective one. The 60 s heat treatment time sample was chosen, because no carbon could be detected on the silver surface.

The described method for impregnation and stabilizer removal was applied to all three synthesized colloidal silver samples. All samples were analyzed by SEM after heat treatment (figure 2.15) to examine particle size and shape.

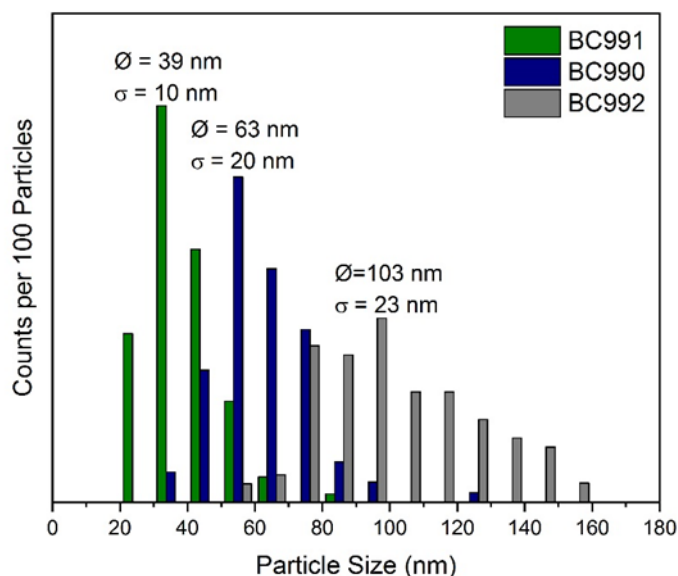
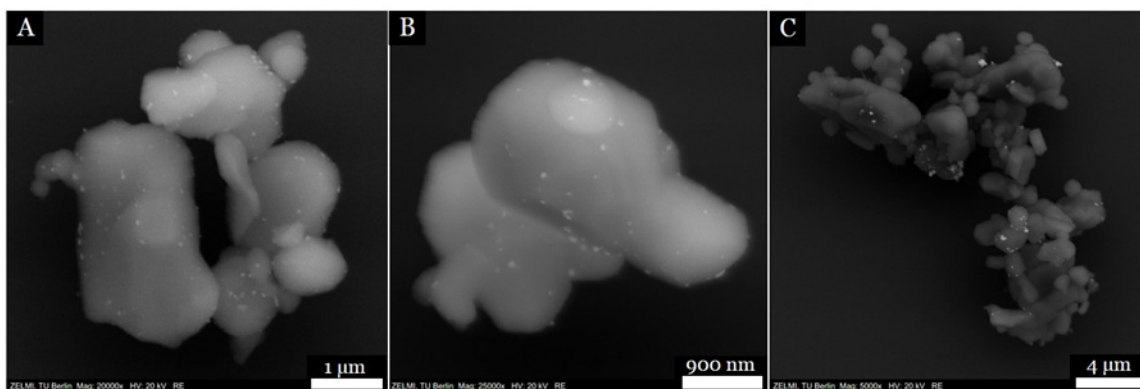


Figure 2.15. SEM images of the three catalysts after the stabilizer removal. The particle size distribution broadened for all samples. Still, the overlap of the samples PSDs is small.

Based on the SEM results it was evident that smaller particles show a better distribution over the support than bigger particles. A possible reason for this is that the smaller particles generate a more stable dispersion. The particle size distribution shows a broadening compared to the colloidal samples. Nevertheless, PSDs of each sample only overlap to a small extent, so that these samples were tested for ethylene epoxidation. Colloid-based samples were given BC (BasCat) numbers according to table 2.6.

ICP-OES analysis was conducted to examine the silver amount for each sample. For digestion, the samples were heated under reflux in concentrated nitric acid. The insoluble alumina was separated and silver dispersions were measured for ICP. The ICP results are shown in table 2.6. Additionally, the silver surface was calculated based on the silver particle radius. It was assumed that all particles are perfectly spherical and there is no interaction with the support or other particles. A detailed calculation for the estimated silver surface can be found in the appendix. In general, all catalysts contained significantly less silver than the targeted 5 wt% due to the before mentioned lack of anchor points at the support surface. The estimated silver surface shows that BC990 (60 nm) has the highest value among the three samples. SEM images of all samples showed some sintering after calcination which means the silver surface is probably lower than the calculated surface in table 2.6. Also the particle size ranges and averages are given in the table. Furthermore, the particles sizes from the particle size study of Van den Reijen et al. for direct comparison is given.^[108] To simplify the discussion, the particle sizes are called 40 nm (BC991), 60 nm (BC990) and 100 nm (BC992).

Table 2.6. Properties of synthesized catalysts and comparison with literature catalysts from Van den Reijen et al. In contrast to these results, any particles smaller than 20 nm in diameter were not detected for the samples in the present work.

Synthesis pH/ Gas posttreatment*	Average Particle Size and Standard deviation [nm]	Particle Range from minimum to maximum [nm]	Silver Loading by ICP [wt%]	Estimated Silver Sur- face [m²/g]
6.9 (BC991)	39 ± 10 (=40 nm)	22-85	1.2	0.24
6.2 (BC990)	63 ± 20 (=60 nm)	37-203	2.3	0.28
6.0 (BC992)	103 ± 25 (=100 nm)	57-220	2.2	0.15
H ₂	28 ± 19*	0-110*	--	--
N ₂	62 ± 21*	10-130*	--	--
O ₂	76 ± 37*	10-280*	--	--

2.3.3. Performance Test

The synthesized catalysts were tested for ethylene epoxidation under industrially relevant conditions in a 16-fold parallel test setup at hte GmbH. 1 mL of each catalyst was used in a fixed bed reactor. Temperatures were varied from 165 °C to 260 °C. The temperature was gradually increased and then decreased in three cycles for each different ethylene chloride (EC) concentration. The screening run protocol is shown in figure 2.16.

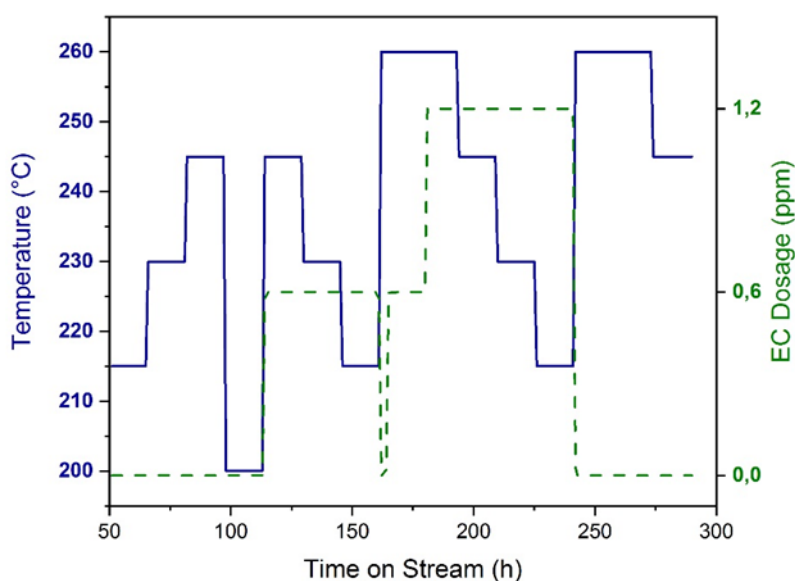


Figure 2.16. Screening program with temperature and ethylene chloride concentration over time on stream. Full test program is given in the experimental part. Due to low conversions, the maximum temperature was increased from 245 °C to 260 °C.

The gas composition was $C_2H_4:O_2:Ar:N_2$ 35:7:5:53. Ethylene chloride (EC) was dosed as promoter in concentrations of 0.0, 0.6 and 1.2 ppm and the tests were conducted at 16 bar and a GHSV of 4850 h^{-1} .

For all samples the ethylene conversion at lower temperatures was very low so that no selectivity towards ethylene oxide could be measured. Increasing the temperature to 245 °C gave conversions above 1.5 %. Comparing to the unpromoted industrial reference catalyst (EO1453), this is still low. E.g. the most active sample BC990 had an ethylene conversion of 1.6 % at 245 °C compared to 11 % for the EO1453 sample. The reason for this could be the much lower silver loading. For EO1453 the silver loading was 15.5 wt%, while the silver loading for the colloid-based samples

was around 2 %. Due to the low activity the second temperature cycle, now with 0.6 ppm EC, started at 215 °C instead of 165 °C. Dosing of 0.6 ppm ethylene chloride to the gas feed was significantly beneficial for sample BC991 as the conversion increased up to 1.81 % at 245 °C. After the positive response to EC, the temperature was also set to 260 °C to increase conversion rates for all catalyst. Increasing the ethylene chloride dosage to 1.2 ppm at 260 °C decreased the conversion of all BasCat catalysts. Due to the low loading, an overpromotion can occur with much lower EC concentrations in comparison to the industrial catalyst with a silver loading of 15.5 %.

For all samples the selectivity to EO at lower temperatures is not detectable. The reason for this is that the ethylene oxide selectivity calculation is based on the formed products and the ethylene conversion was very low. At 260 °C, all samples show a measurable selectivity towards EO with BC991 having the highest ethylene oxide selectivity with 71.8 %. Adding ethylene chloride to the gas stream with a dosage of 0.6 ppm all samples show strongly increased selectivity. Again, BC991 is the most selective catalyst with 75 %. Increasing the ethylene chloride dosage to 1.2 ppm at 260 °C increased the selectivity of all BasCat catalysts except BC990. At these conditions BC992 was the most selective BasCat catalyst with 78.16 %. Compared to the reference catalyst (EO1453) the ethylene oxide selectivities of all BasCat catalysts were slightly higher at temperatures of 245 °C and 260 °C. However, the selectivity was strongly dependant on the conversion which was much lower for the BasCat samples compared to the reference. The most important values are summarized in table 2.7.

Table 2.7. Performance data at 260 °C without ethylene chloride and with 0.6 and 1.2 ppm EC dosage. More details about the reaction conditions can be found in the experimental section. Values with an asterisk were measured at 215 °C.

Condition Sample	X _{C₂H₄} , 0 ppm EC [%]	S _{EO} , 0 ppm EC [%]	X _{C₂H₄} , 0.6 ppm EC [%]	S _{EO} , 0.6 ppm EC [%]	X _{C₂H₄} , 1.2 ppm EC [%]	S _{EO} , 1.2 ppm EC [%]
BC991 – Ag (40 nm)/Al ₂ O ₃	2.5	71.8	2.7	75	2.1	77.8
BC990 – Ag (60 nm)/Al ₂ O ₃	1.5	69.4	1.6	72.3	1.5	71.7
BC992 – Ag (100 nm)/Al ₂ O ₃	2.4	54.7	1.6	74.9	1.1	78.2
Reference sample (Ag/Al ₂ O ₃ , 15 wt% Ag)	12.4*	59.9*	12.2*	73.3*	9.9*	77.3*

The catalytic results confirm literature results as particles between 40-60 nm behave differently in comparison to particles greater than 60 nm regarding selectivity. Without chlorine promotion, BC991 showed the highest selectivity towards ethylene oxide while BC992 showed the lowest selectivity. By dosing only 0.6 ppm EC, the selectivity values changed drastically. While the selectivities of BC991 and BC990 only increased marginally, samples with bigger particle sizes were greatly influenced by chlorine promotion (BC992 and EO1453). For example, the selectivity of BC992 increased from 54.7 % to 74.9 % at 260 °C. Also the EO selectivity of the reference sample, where the majority of silver particles is greater 100 nm, was strongly increased. After EC dosage all selectivity values are within a small margin. In figure 2.17 a linear fit of the selectivities with data from table 2.7 in dependence of the particle size at 260 °C and at different EC concentrations is shown. Here, the positive influence of EC on bigger particles is pointed out. Also, a selectivity increase with higher EC concentrations for all samples can be observed.

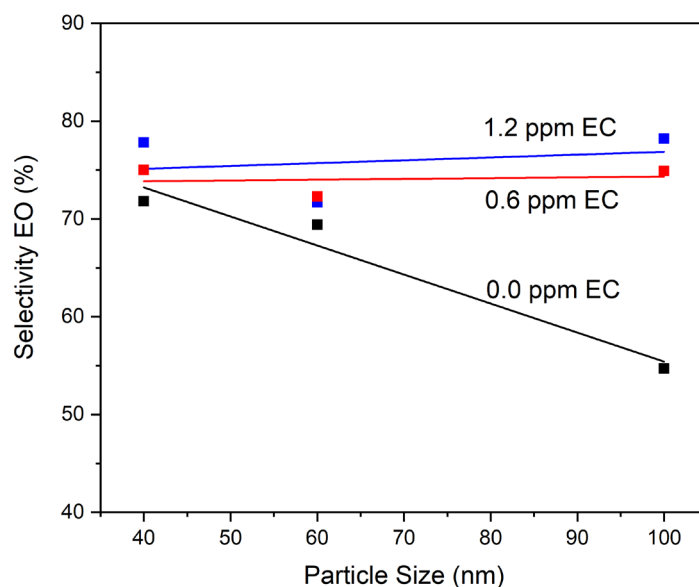


Figure 2.17. Selectivity towards ethylene oxide in dependence of particle size and EC concentration. The graphs are linear fits with data from table 2.7. With EC dosing, the particle size effect regarding the selectivity is offset.

As described in the introduction, ethylene chloride dosage changes the ratio of electrophilic to nucleophilic oxygen, which directly influences the selectivity.^[88] To generate electrophilic oxygen, chlorine adsorbs on silver-oxygen interfaces and withdraws electron density from the oxygen. The particle size plays a deciding role in the

uptake of bulk oxygen. XPS measurements by Bukthiarov et al. showed that particles bigger than 40 nm have a peak in the Ag 3d measurement with the same binding energy as Ag_2O , while smaller nanoparticles have the same binding energy as metallic silver. It can be assumed that a certain size is necessary to obtain the selective species. Apparently all BasCat samples have the necessary size for oxygen uptake as seen by the selectivity values. If no EC is dosed, it seems that BC991 has the best surface to volume ratio which results in a good ratio of electrophilic to nucleophilic oxygen and thus, a high selectivity. With increasing particle size selectivities decrease probably due to an excess of bulk oxygen. The dosing of EC changes the electronic properties of the surface oxygen by making it more electrophilic. Therefore particle sizes become irrelevant after EC dosage. This is assumedly the reason that even much bigger particles on the industrial catalysts are still very selective after long run time (several 1000 h).

2.3.4. Characterization of Spent Samples

After the performance test, the spent samples were characterized by multiple methods to examine the changes in structural and electrical properties during the catalytic conversion.

SEM Analysis

SEM was used to examine the degree of sintering for the silver particles. One characteristic image and the particle size distribution is shown in figure 2.18. After 300 h time on stream, the degree of sintering differs for the samples. While the 40 and 60 nm samples have an increased average particle size of about 14 % (BC991: from 39 nm to 44.5 nm on average and BC990: from 63 nm to 72 nm on average), the average particle size for the 100 nm sample increased by around 33 %, from 103 nm to 137 nm on average. One reason for this could be the sintering mechanism. By Ostwald ripening bigger particles grow at the cost of smaller particles. As BC992 had a broader PSD in comparison to BC991 or BC990, the Ostwald ripening is possibly more pronounced. This could also be the case for the industrial catalyst. A catalyst with monodisperse silver particle distribution would probably help to decrease the speed of the deactivation process.

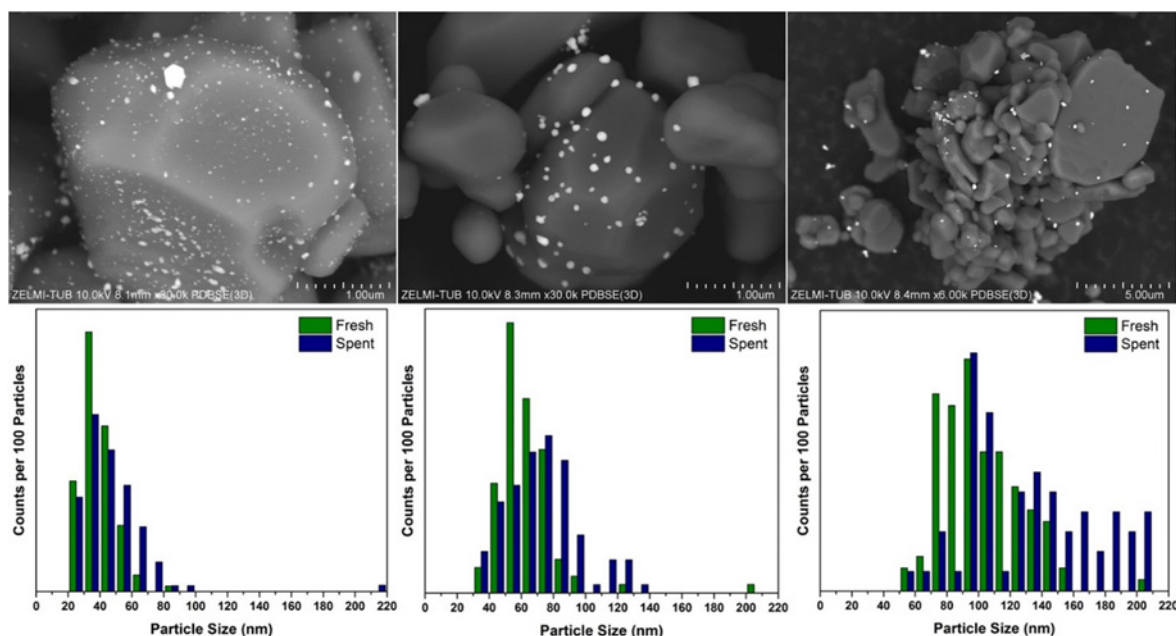


Figure 2.18. SEM images of spent catalysts after 300 h time on stream. Left: BC991 (40 nm); middle: BC990 (60 nm); right: BC992 (100 nm). For the 100 nm sample the most pronounced growth is observed (+ 33 % in average particle size). The 40 and 60 nm samples have an increased average particle size of about 14 %.

XPS Analysis

To examine electronic properties of the surface, XPS measurements for spent samples were conducted (figure 2.19). Signals were charge corrected with the C-C signal at 284.8 eV. For the silver signal, the Ag3d_{5/2} transition was evaluated. Additional to the used samples, another spent catalyst from another run was measured by XPS. This catalyst was prepared by laser ablation and had an average silver particle size of around 20 nm after supporting. Higher silver oxidation states are shifted to lower binding energies. This indicates a higher Ag(I) amount and more oxygen absorption by the sample. While the 20 nm sample peak can be assigned to metallic silver, all other samples show a mixed content of Ag(I) and Ag(0) species. Consequently, it can be assumed that silver particles have to have a certain size for oxygen absorbance. Based on our results the size should be between 20 and 40 nm.

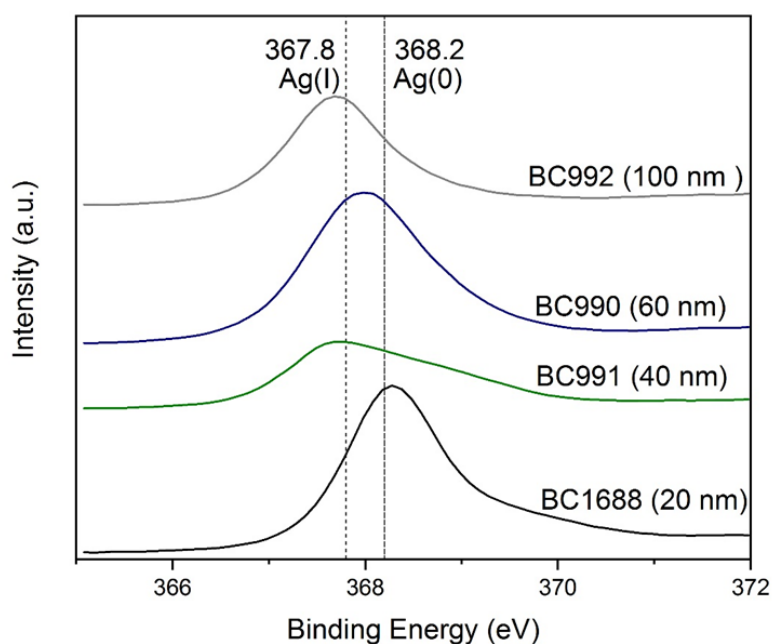


Figure 2.19. XPS measurement of spent catalysts after 300 h time on stream. A tendency towards surface silver oxide is observed for samples 40, 60 and 100 nm, while the 20 nm sample (prepared by laser ablation) can rather be assigned to metallic silver.

Elemental Analysis

Since carbon deposition on the silver particles could lead to deactivation in the catalytic reaction, all four catalysts were analyzed by elemental analysis to measure the carbon amount before and after catalysis. Results of the elemental analysis are shown in table 2.8. After catalysis, the carbon amount increases for BC991 and BC992 and decreases for BC990. The carbon amount is not correlating with the activity of the samples. In addition to that, values are near the detection limit and could be slightly inaccurate. In conclusion, the measured carbon amount has probably little to no influence on the activity of the catalysts.

Table 2.8. Carbon amount as measured by elemental analysis before and after catalysis for all three samples. Two measurements were conducted for each sample.

Sample	Particle size [nm]	Carbon before catalysis [%]	Carbon after catalysis [%]
BC990-1	60	0.19	0.17
BC990-2	60	0.22	0.09
BC991-1	40	0.03	0.22
BC991-2	40	0.03	0.18
BC992-1	100	0.02	0.09
BC992-2	100	0.02	0.25

2.3.5. New Synthesis Method for Silver Nanoparticles

Potassium in low concentrations is known as a promoter for the ethylene epoxidation over silver-based catalysts. However, higher amounts can lead to catalyst deactivation.^[122] During the colloidal synthesis, potassium carbonate is used to adjust the pH. Despite washing the nanoparticles after reaction, potassium can remain in the dispersion. High potassium content was identified as one possible reason for the low activity of the catalysts used in the performance test in chapter 2.3.3. To avoid potassium in the final catalyst, the pH during the synthesis was adjusted by ammonium hydroxide. As hydroxides are strong bases and carbonates only weak bases, smaller amounts were needed. Thus, also less amounts of the cation were present in the final product.

Figure 2.20 shows the absorption range of silver nanoparticles for the new series of silver catalysts. The pH value is the only variable parameter in the synthesis. A

smaller pH leads to a red-shift of the absorption maximum and hence an increase in particle size.

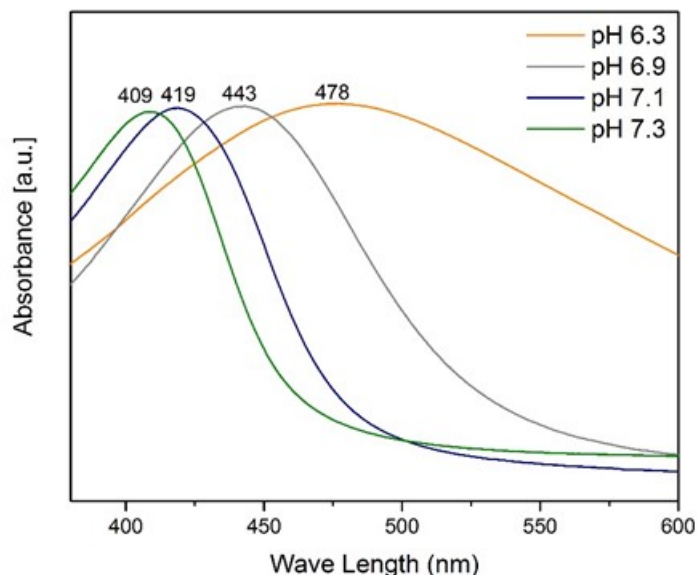


Figure 2.20. UV-VIS measurements of the tannic acid stabilized silver colloids at different reaction pH values with ammonium hydroxide as the pH setting reagent. The sample synthesized at higher pH value absorbs at higher wave length.

Notably, the pH needed to synthesize particles of the same size is higher for NH_4OH in comparison to K_2CO_3 . The underlying effect for this observation could be the stabilizing effect of the anion. Carbonates are bulkier and charged negatively two times. Hydroxides have less stabilizing power than carbonates and thus, a higher pH is needed to produce nanoparticles of the same size as before. At higher pH the reduction power of tannic acid is increased, which then counteracts the lower stabilizing power of ammonium hydroxide. The pH differences for different sizes are shown in table 2.9.

Table 2.9. Particle sizes as measured by UV-VIS depending on the pH value and the pH setting value. With ammonium hydroxide, a higher pH value is needed to obtain silver colloids with the same size as with potassium carbonate.

Particle Size [nm]	pH old method (K_2CO_3)	pH new method (NH_4OH)
15	7.1	7.3
25	6.9	7.2
45	6.7	6.9
80	6.0	6.3

With TEM imaging the shape, size and local anomalies of each sample can be seen. A representative TEM image of samples synthesized at pH 7.3, 6.9 and 6.3 is shown in figure 2.21. While for sample pH 7.3 all particles are spherical shaped, the particles for pH 6.9 and 6.3 are mostly irregularly shaped. Though it has to be taken into account that TEM only represents a very small sample fraction, the particle shapes and size distributions are in accordance with the first series of colloids synthesized with potassium carbonate.

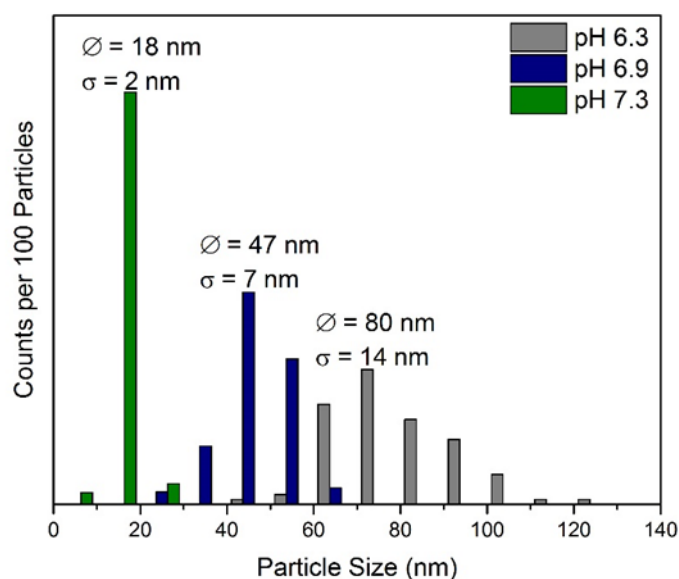
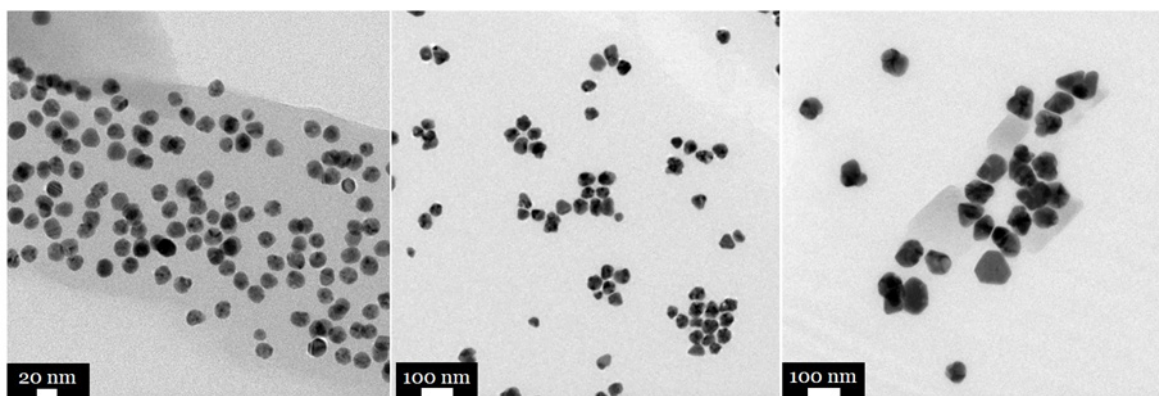


Figure 2.21. TEM images of the tannic acid stabilized silver colloids at different reaction pH values (A, B, C) and their particle size distribution (D). Smaller particles show a more narrow particle size distribution in comparison to bigger particles.

In summary, a new method to synthesize silver nanoparticles without potassium and carbonate, which can be both catalyst poison in high amounts, was established. The particles could not be tested due to lack of availability of an appropriate test setup.

2.4. Conclusion

The synthesis of colloidal silver nanoparticles with narrow particle size distributions (standard deviation < 15 %) was successful. Particles ranging from 20 to 80 nm were synthesized by reduction and stabilisation of tannic acid. With this method, the generation of small particles (< 10 nm) was excluded. Ammonium hydroxide as pH adjusting reagent was successfully implemented with similar results as potassium carbonate. Using citric acid and tannic acid as stabilizers, the synthesis of particle greater than 100 nm with narrow particle size distributions were conducted, albeit with low product output.

After impregnation of the colloids on industrial α -alumina support several methods for stabilizer removal were conducted. The short heat treatment was more efficient in removing carbon as well as mitigating sintering in comparison to conventional calcination and ozone treatment.

Among the tested samples, smaller silver particles (40 nm) showed the highest selectivity for ethylene epoxidation if unpromoted. The difference in selectivity to ethylene oxide was 17 % at 260 °C compared to 100 nm particles. When ethylene chloride was added to the feed, the selectivities for all samples were levelled out.

Characterization of spent samples by SEM showed sintering for all samples after 300 h time on stream. However, smaller particles (40 and 60 nm) sintered only by 14 % on size average in comparison to 33 % for the 100 nm sample. Because of the better dispersion of the two former samples the Ostwald ripening as a mode of sintering could be mitigated.

XPS measurements of the spent samples showed at least partially Ag(I) surface species, probably being adsorbed oxygen species. The ratio of nucleophilic to electrophilic oxygen is responsible for the selectivity to ethylene oxide. Because smaller particles can absorb less oxygen, the oxygen species ratio changes in favour of the selective electrophilic species. Hence, a higher selectivity in comparison to bigger particles was observed. The chlorine promotion negates this advantage of smaller particles by modifying surface silver/oxygen species. Accordingly, the selectivity of all prepared samples is very similar after EC dosage.

Thus, the electronic promotion is responsible for the high selectivity during the long time on stream for the industrial catalyst, where particles much bigger than 100 nm

can be observed. While the synthesis of colloid-based catalysts is not viable for industry due to low silver loadings, reduced sintering for samples with narrow particle size distributions should be further studied. By optimizing synthesis and pretreatment of the catalyst more narrow particle size distributions can be obtained, which could lead to higher longevity of the catalysts.

The sample with the smallest silver particles (40 nm) showed a selectivity of 75 % towards ethylene epoxide without addition of ethylene chloride. Adding a suitable promoter package could further increase the selectivity so that addition of EC could be avoided. However, to make the colloid-based catalyst economically more viable, an increase in silver loading would be necessary. On the other hand, high silver loadings can facilitate sintering and thus, decreasing the selectivity.

2.5. Appendix

Table A2.1. Calculation for total silver surface per gram in each sample. Calculations were carried out with colloid radius and the assumption that all particles are perfect spheres.

Sample	ICP results [wt% silver]	Radius colloids [nm]	Mass per particle ($V \cdot \rho_{\text{silver}}$) [mg]	Particle number (mass Ag/g/ Mass per Ag particles)	Surface Ag particle [m ²]	Surface Ag per gram ($A_{\text{Ag particle}} \cdot \text{number Ag particles}$) [m ² /g]
BC991	1.22	12.5	8.58E-14	1.42E+14	1.96E-15	0.28
BC990	2.26	27.5	9.14E-13	2.47E+13	9.50E-15	0.24
BC992	2.16	40	2.81E-12	7.68E+12	2.01E-14	0.15

3. Sulfur Promotion Study for Ethylene Epoxidation

3.1. Introduction

Since the discovery of the modern process for ethylene epoxidation much research was dedicated to improvement of the catalyst. As described in previous chapters a promoter package is needed to obtain high selectivity for silver based catalysts. Fundamental understanding of the role of each promoter would be valuable in improving the catalyst's performance. For some of the used promoters publications about possible promoting mechanisms have been published. E.g. the chlorine promotion was discussed in detail in chapter 2.3. Alkali metals like caesium and potassium are possibly blocking the few remaining acidic sites of the support, which lead to isomerization to acetaldehyde and further to total oxidation. Thus, they are viewed as structural promoters in the majority of publications.^[102,123,124] However, also reports about caesium as an electronic promoter exist.^[125] In that case caesium hinders the isomerization of ethylene oxide to acetaldehyde by stabilizing the adsorbed EO through electron donation to the oxygen atom. In the 1980s the addition of rhenium lead to a significant increase in EO selectivity for the EO process. More specifically, high-valent Re oxyanions are added to the industrial catalyst. From a mechanistic standpoint, Diao et al. suppose, based on XPS results, that Re^{7+} makes the silver surface more electron deficient and thus, more selective towards EO by decreasing isomerization reactions of the product.^[80] Although this proposed mechanism is similar to chlorine promotion, the two promoter mechanisms have to be different. High amounts of chlorine act as poison and only by addition of rhenium, selectivities of around 90 % are possible. In addition to rhenium many more transition metals, all high-valent oxyanions, like Cr, Zr, V, can be added during catalyst synthesis to enhance performance. The effect of sulfur is not clarified yet, but it is also added as sulfate, a high-valent oxyanion.

Consequently, sulfur could be one of the promoters that could be the key for understanding the selectivity values achieved by adding promoter packages. In recent studies sulfur could not be detected in the spent EO catalyst, which deactivated with time on stream. While the exact sulfur species is not known yet, ammonium sulfate is used as the precursor for the industrial catalyst.

For this project, two catalysts were synthesized to examine the sulfur promoter role. First, a regular, colloid-based silver on alumina catalyst as introduced in chapter 2. To this catalyst ammonium sulfate was added via dry impregnation. To study the importance of the sulfur-silver interaction it is crucial to synthesize a material with a high contact area between sulfur and silver. This could be achieved by introducing a core-shell structure. The specific synthesis of core-shell particles is a new research area where synergistic effects between the core and the shell play a decisive role. The second catalyst was a colloid-based core-shell material with silver core and silver sulfide shell. By this, the sulfide can interact with the silver in close proximity. Silver sulfide is a stable compound that forms spontaneously when silver and sulfide are in contact. Both samples will be tested for the ethylene epoxidation and compared to a colloid-based reference sample (BC991 from chapter 2). The possibility of conversion of silver sulfide into sulfate in the oxygen containing gas stream during the catalytic reaction will be examined.

3.2. Experimental

3.2.1. Synthesis of Silver-Silver Sulfide Core-Shell Particles

Silver nanoparticles were synthesized according to chapter 2.2.

The prepared silver dispersion by single injection method with particles sizes of 25 nm (approx. 33 mg silver in 100 mL H₂O) were added to a 250 mL round bottom flask. An aqueous solution of sodium sulfide nonahydrate (10 mL of an 1.5 mM solution for a 1:20 S:Ag ratio and 2.74 mL for a 1:73 S:Ag ratio) was prepared and added to the stirring silver solution, which was stirred at 1400 rpm (maximum stirring speed). The reaction was finished after 30 minutes indicated by color change from orange to black.

The supporting of these colloids was conducted according to chapter 2.2, yielding samples **BC1573** (Ag:S 20) and **BC1574** (Ag:S 73). Sample BC1575 was prepared similar to BC991. After complete supporting of silver nanoparticles on the alumina, an aqueous solution of ammonium sulfate (1 mL of a 0.025 M solution) was impregnated on the sample (3 g Ag/Al₂O₃ with a target loading of 2 % Ag). The silver to sulfur ratio was chosen according to the core-shell sample with the lower sulfur amount. The solid was then heat treated at 600 °C for 60 s.

3.2.2. Preparation of XPS Reference Samples

Two samples were prepared as references for sulfur XPS measurements.

First, sodium sulfate nonahydrate was dissolved in water (10 mL of an 1.5 mM solution) and then physically mixed with α -alumina (1 g) with a spatula. After drying at rt, the sample was calcined in a muffle oven for 3 h at 350 °C.

For the second sample silver nitrate (787 mg, 4.6 mmol) was dissolved in water (2 mL) and then stepwise physically mixed with α -alumina (1 g) with a spatula. After drying at rt, the sample was calcined in a muffle oven for 3 h at 300 °C to remove the nitrate. Then, sodium sulfate nonahydrate was added to the sample via dry impregnation. Again, the sample was calcined in a muffle oven for 3 h at 350 °C.

3.2.3. Catalytic Screening

Catalytic screening was carried out at the hte GmbH in Heidelberg. For each sample 1 mL was used in a sieve fraction of 250-315 μm . The run protocol is given in table 3.1.

Table 3.1. Run protocol for 2nd ethylene epoxidation catalysts screening at hte.

Phase	Runtime [h]	Temp. [°C]	Ethen IN [vol.%]	O2-IN [vol.%]	Ethylene chloride-IN [ppm]	Ar-IN [vol.%]
1	16	215	35	7	0	5
2	16	230	35	7	0	5
3	16	245	35	7	0	5
4	16	260	35	7	0	5
5	16	275	35	7	0	5
6	16	245	35	7	0	5
7	16	215	35	7	0.6	5
8	16	230	35	7	0.6	5
9	16	245	35	7	0.6	5
10	16	260	35	7	0.6	5
11	25	245	35	7	0	5
12	16	215	35	7	1.2	5
13	16	230	35	7	1.2	5
14	16	245	35	7	1.2	5
15	16	260	35	7	1.2	5
16	25	245	35	7	0	5

3.2.4. Characterization of Silver-Silver Sulfide Colloids and Supported Samples

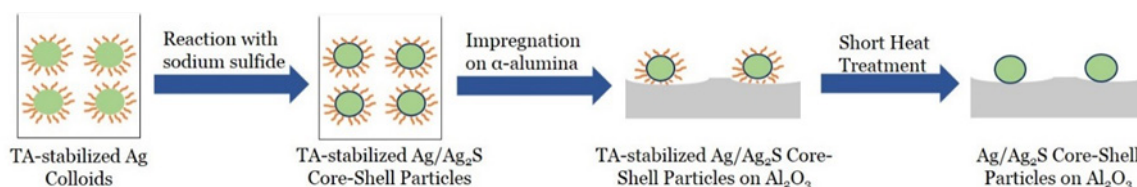
Transmission electron microscopy (TEM) was carried out with a FEI Tecnai G² 20 S-TWIN with an equipped r-TEM SUTW Detector for electron dispersive x-ray spectroscopy. 25 μL of sample (stabilized silver particles in water) were placed on a carbon coated copper grid. Then, the grid was dried at rt before put on the sample holder.

Further TEM measurements, STEM and STEM mappings were conducted with a JEOL JEM-ARM200CF electron microscope at the FHI. The samples were measured on carbon coated copper grid cells.

X-ray photoelectron spectroscopy (XPS) was measured on K-Alpha^{TM+} X-ray Photoelectron Spectrometer System from Thermo Scientific. The x-ray source was Al-K_α-radiation. For the measurement, the solid samples were pressed and put on carbon taps which were put in the sample holder for measurement. Survey spectra were run in the binding energy range of 0-1000 eV and high-resolution spectra of C1s, O1s and Ag3d_{5/2} were collected.

3.3. Results

To study the importance of the sulfur-silver interaction one objective was to synthesize Ag@Ag₂S core-shell nanoparticles. By sulfidation of colloidal tannic acid capped silver particles, some of the silver should be converted to silver sulfide to obtain core-shell particles (scheme 3.1). Impregnation and stabilizer removal was conducted the same way as in chapter 2.



Scheme 3.1. Scheme for the preparation of a core-shell colloid-based catalyst. First, the precursor is reduced in presence of a stabilizer. The formed colloids are purified and then coated with the sulfur shell. Then, core-shell colloids are supported via wet impregnation. The last step is the removal of the stabilizer.

3.3.1. Silver-Silver Sulfide Core-Shell Particle Synthesis and Characterization

For this study, sodium sulfide nonahydrate was used as the sulfur source similar to other literature publications.^[126,127] Two parameters were tuned to achieve a successful, uniform sulfide coating. At first, the Ag:S ratio was varied. The sulfur shell should be very thin to not block silver sites during the catalytic reaction. Secondly, the stirring speed was varied. Since the reaction of silver with sulfide is thermodynamically favored, a complete mixing in a short time is necessary to obtain a uniform coating. For a first try, the reaction was carried out with a ratio of Ag:S of 10 and a stirring speed of 700 rpm. After few minutes, the orange colored dispersion changed to black. The resulting colloidal particles were analyzed by TEM shown in figure 3.1.

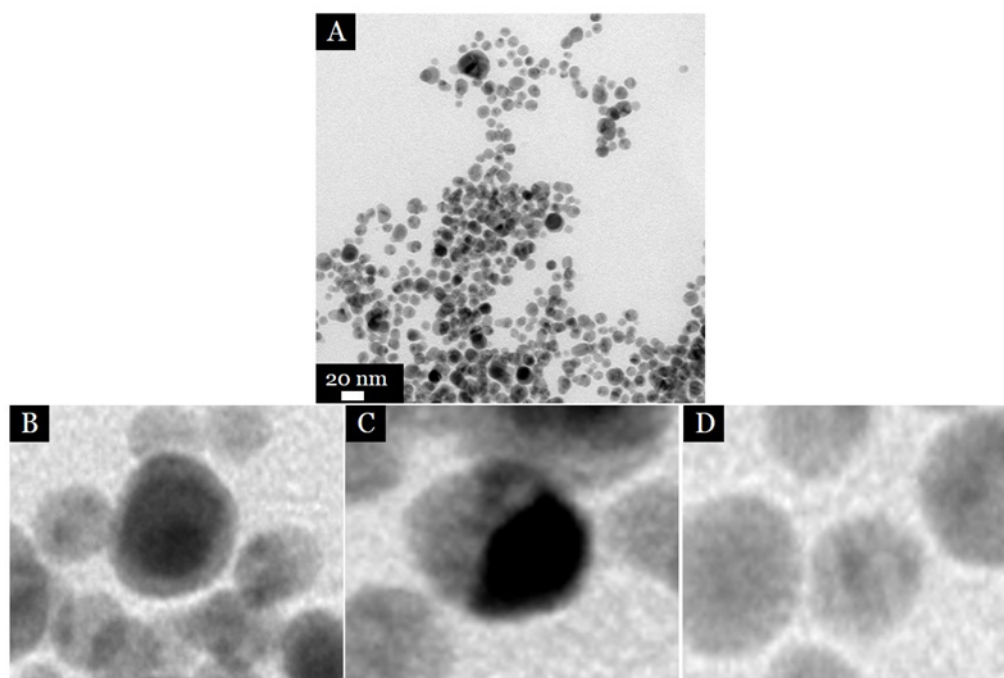


Figure 3.1. TEM overview image of silver/silver sulfide composite (A) and magnification (B, C, D) of image A. Silver shows a stronger contrast (darker compared to the background) than silver sulfide. Colloids formed as desired core-shell particles (A), but also as Janus particles (B). Furthermore, also silver sulfide only particles formed (D).

The TEM images show irregular shapes and heterogeneous particle distribution of $\text{Ag}_2\text{S}/\text{Ag}$ composite nanoparticles. Most of the nanoparticles were completely sulfidized while also some core-shell $\text{Ag}_2\text{S}@\text{Ag}$ nanoparticles were present. Interestingly, Janus type $\text{Ag}_2\text{S}/\text{Ag}$ composite nanoparticles were also seen in TEM measurements. Because of the high amount of completely sulfidized particles, the Ag:S ratio was increased to 20. Complete sulfidation could also originate from lack of mixing. Consequently, the stirring speed was increased to 1400 rpm. The TEM images and related EDX spectra for the second series of silver/silver sulfide particles are shown in figure 3.2.

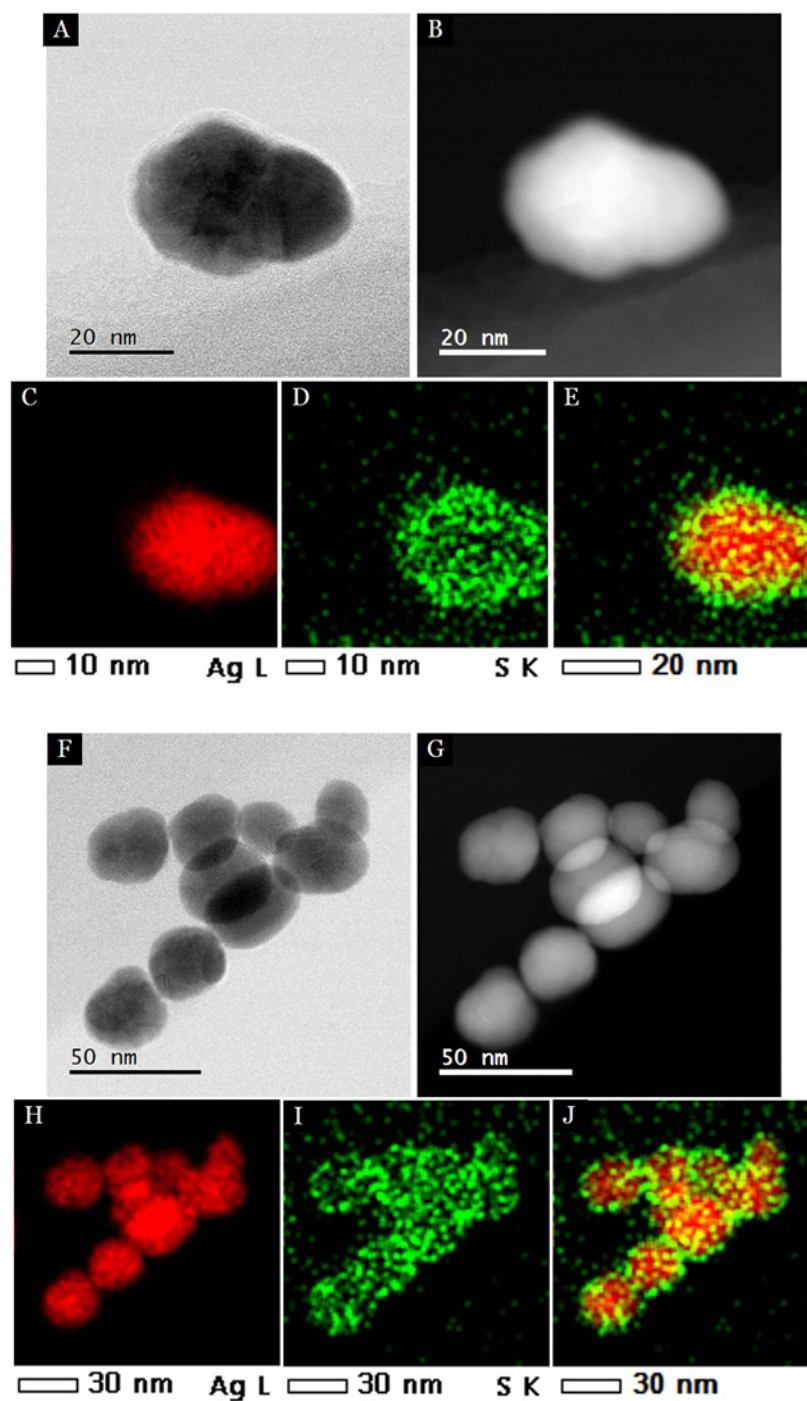


Figure 3.3. TEM, STEM images and mapping of silver/silver sulfide core-shell particles. Sulfur (green) signals were observed around silver (red). Yellow color indicates overlap of silver and sulfur.

STEM images in combination with EDX mapping show the distribution of sulfur (green) and silver (red). The sulfur, probably being the used sulfide species, decorates the silver nanoparticles. While there is no fully closed shell, the sulfur is homogeneously distributed around the silver nanoparticles according to the STEM images. Since the measurement is local, several EDX mappings were performed to ob-

tain an average value for the Ag:S ratio, which was around 50. The results are summarized in table 3.2 and the related EDX maps are given in appendix (A.3.2). Prepared core-shell particles were supported as described in chapter 2.2. The final catalysts were called BC1573 (Ag:S 20) and BC1574 (Ag:S 73).

Table 3.2. Results from EDX measurements at four different positions during STEM measurements. Theoretical silver to sulfur ratio was 73. STEM images for marked positions can be found in the appendix.

Position	Silver [at%]	Sulfur [at%]	Atomic ratio Ag:S
1	9.51	0.21	45.3
2	18.15	0.35	51.9
3*	8.16	0.39	20.9
4*	14.43	0.18	80.2

Another catalyst to examine the silver/sulfur interaction was synthesized. According to newest literature results the active site of the ethylene epoxidation catalysts is the sulfate supported on an oxygen-silver structure.^[97] To examine this finding, a colloid-based catalyst in same manner as BC991 was synthesized. On this catalyst, ammonium sulfate was deposited via dry impregnation. For comparability, the same Ag:S ratio was used as in BC1574 (Ag:S 73). After deposition, another short heat treatment for 60 s at 600 °C was carried out to remove the ammonium.

3.3.2. Performance Test

The program for the catalytic testing was based on the first series' results (figure 3.4). As the colloid-based catalysts were only active in higher temperature regions, this second program started at 215 °C and increased in 15 °C steps. Again, three cycles were run, the first without ethylene chloride (EC) dosage, the second with 0.6 ppm EC and the third with 1.2 ppm EC. The highest temperature was chosen to be 275 °C, which is higher than the industrial process temperature. The reason for that was the good performance of the first series catalysts at 260 °C (see chapter 2.3.). However, initial results didn't show a pronounced performance improvement from 260 °C to 275 °C. Thus, 260 °C was chosen as the highest temperature for the cycles with ethylene chloride (EC) dosage. After each temperature ramp

a reference point was measured at 245 °C and no EC dosage. The results for the synthesized catalyst and a reference colloid-based catalysts are shown in table 3.3.

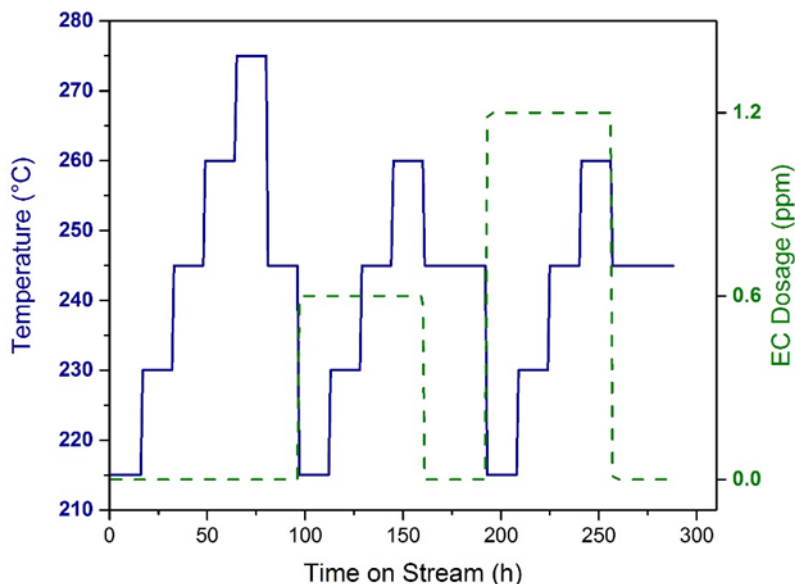


Figure 3.4. Screening program with temperature and ethylene chloride concentration over time on stream. Full test program is given in the experimental part. Due to low conversions in the first run (chapter 2), the maximum temperature was increased from 260 °C to 275 °C.

Table 3.3. Performance data at 260 °C without ethylene chloride, with 0.6 and 1.2 ppm EC dosage. More details about the reaction conditions can be found in the experimental section. BC1573 and BC1574 are silver-silver sulfide core-shell particles supported on α -alumina. The BC1575 sample was prepared by adding sulfate via dry impregnation (DI) to the BC991 catalyst. The data for the BC991 catalyst was measured with a slightly different run protocol. Further details can be found in chapter 2.3.

Condition Sample	$X_{C_2H_4}$, 0 ppm EC [%]	S_{EO} , 0 ppm EC [%]	$X_{C_2H_4}$, 0.6 ppm EC [%]	S_{EO} , 0.6 ppm EC [%]	$X_{C_2H_4}$, 1.2 ppm EC [%]	S_{EO} , 1.2 ppm EC [%]
BC1573 (Ag:S 20)	0.4	70.2	0.3	-	0.3	-
BC1574 (Ag:S 73)	0.4	61.7	0.5	73.3	0.4	77.6
BC1575 (Sulfate DI)	2.3	55.1	3.2	77.4	2.2	80.8
BC991 – Ag (40 nm)/Al ₂ O ₃	2.5	71.8	2.7	75	2.1	77.8

The conversion of both sulfide containing samples (BC1573 and BC1574) was very low at all reference points with no clear tendency if more or less sulfide leads to higher conversions. Also, no tendency regarding the influence of EC can be seen. The sample with the dry impregnated sulfate species (BC1575) showed a slightly higher ethylene conversion and selectivity to EO after EC dosage compared to the colloid-based reference catalyst (BC991). Based on these results it is assumed that the sulfide species is not the promotional sulfur species and does not convert into a promoter under reaction conditions. Thus, the sulfide species only coated active surface sites on the silver particles as the performance was lower compared to the colloidal reference sample. Another possibility could be a detrimental electronic effect by the sulfide species.

The sulfate added sample showed generally higher conversions compared to the sulfide samples. After heating to 275 °C (first temperature cycle) the ethylene conversion dropped from 1.7 % to 1.3 %, probably due to sintering. Adding 0.6 ppm EC improved the conversion for the colloid-based reference and the sulfate sample. After increasing the EC concentration to 1.2 ppm both samples decreased in ethylene conversion, but increased in ethylene oxide selectivity with the sulfate added sample showing a selectivity over 80 %. For all tested colloid-based catalysts the activity decreased after increasing the EC concentration to 1.2 ppm, indicating an active site poisoning. As described in chapter 2, promotion with chlorine can lead to higher amount of electrophilic oxygen and less nucleophilic oxygen. The first step for the chemical reaction is the adsorption of ethylene which is assumed to be done by nucleophilic oxygen. Thus, decreasing nucleophilic oxygen will lead to smaller conversions. Additionally, due to the low loading, an overpromotion can occur with much lower EC concentrations in comparison to the industrial catalyst with a silver loading of 15.5 %.

Jones et al. proposed that sulfate is the active site in ethylene epoxidation.^[97] This means that in a dynamic reaction always two species are present on the surface, namely sulfate and sulfite. The latter can stabilize electrophilic oxygen with the free electron pair, while the former can stabilize nucleophilic oxygen adatoms with the S^{2+} center. By this a balance between electrophilic and nucleophilic oxygen can be achieved.

3.3.3. Characterization of Spent Samples

XPS measurements were carried out to examine the surface of the sulfate promoted catalyst after the reaction. For the sulfate sample BC1575 the question was, if sulfate is deposited on the support or on the silver particles after catalysis. As references, two samples were prepared by dry impregnation. The first was ammonium sulfate on alumina, with the same precursor used as in the reference sample (BC1575). For the second sample, silver nitrate was impregnated with a very high amount (30 wt%) to ensure a complete surface coverage. Subsequently, ammonium sulfate was impregnated on the supported silver sample. By this, a difference between sulfate on alumina and on silver should be visible due to electronic effects. The binding energy of the S2p_{3/2} after fitting of the measured values distinguishes from 169.1 eV for the surface alumina sample and 168.4 eV for the surface silver sample (figure 3.5). Measurements of BC1683 (spent sample of BC1575) show a S2p_{3/2} peak at 169.1 eV after fitting. This indicates the presence of the sulfate species on the support and not on the silver particles. Nevertheless, sulfate and silver particles could be in close proximity for electronic promotion during the reaction.

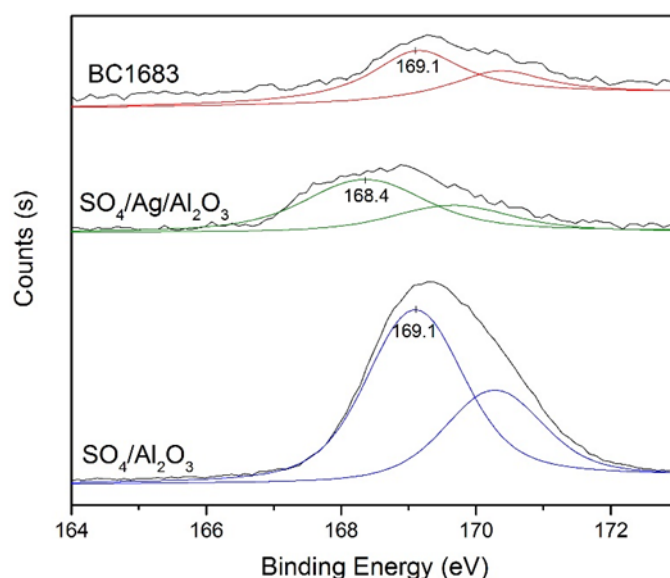


Figure 3.5. XPS measurement of spent catalysts after 300 h time on stream. After fitting, the S2p_{3/2} peak is measured at 169.1 eV for the spent BC1575 sample, which indicates that after reaction the sulfur is located on the alumina support.

3.4. Conclusion

The synthesis of silver-silver sulfide core-shell particles with two different silver to sulfur ratios was successful. STEM images with EDX maps confirm a uniform distribution of a sulfur species, probably silver sulfide around silver nanoparticles. After supporting and stabilizer removal according to chapter 2, colloid-based catalysts were tested for ethylene epoxidation. The supported core-shell particles showed very low activity so that a poisoning with the sulfide coverage can be assumed. The colloid-based catalyst with sulfate addition showed better activity and selectivity towards ethylene oxide in comparison to the unpromoted colloid sample. This indicates that sulfate is the active sulfur species in this reaction. The results show, that adding a high valent promoter like sulfate is beneficial for the catalyst's performance. As a next experiment, a test series with different sulfate amounts on supported silver catalysts, to examine to which degree the promoter effect could be maximized, could be carried out.

By XPS measurements the location of the sulfur was examined. The sulfate species is located on alumina and not on silver. Despite that, sulfur can be in close proximity to silver or grow over silver particles during the reaction. In situ XPS measurements under reaction conditions would be necessary to draw a final conclusion on the location of sulfur during reaction.

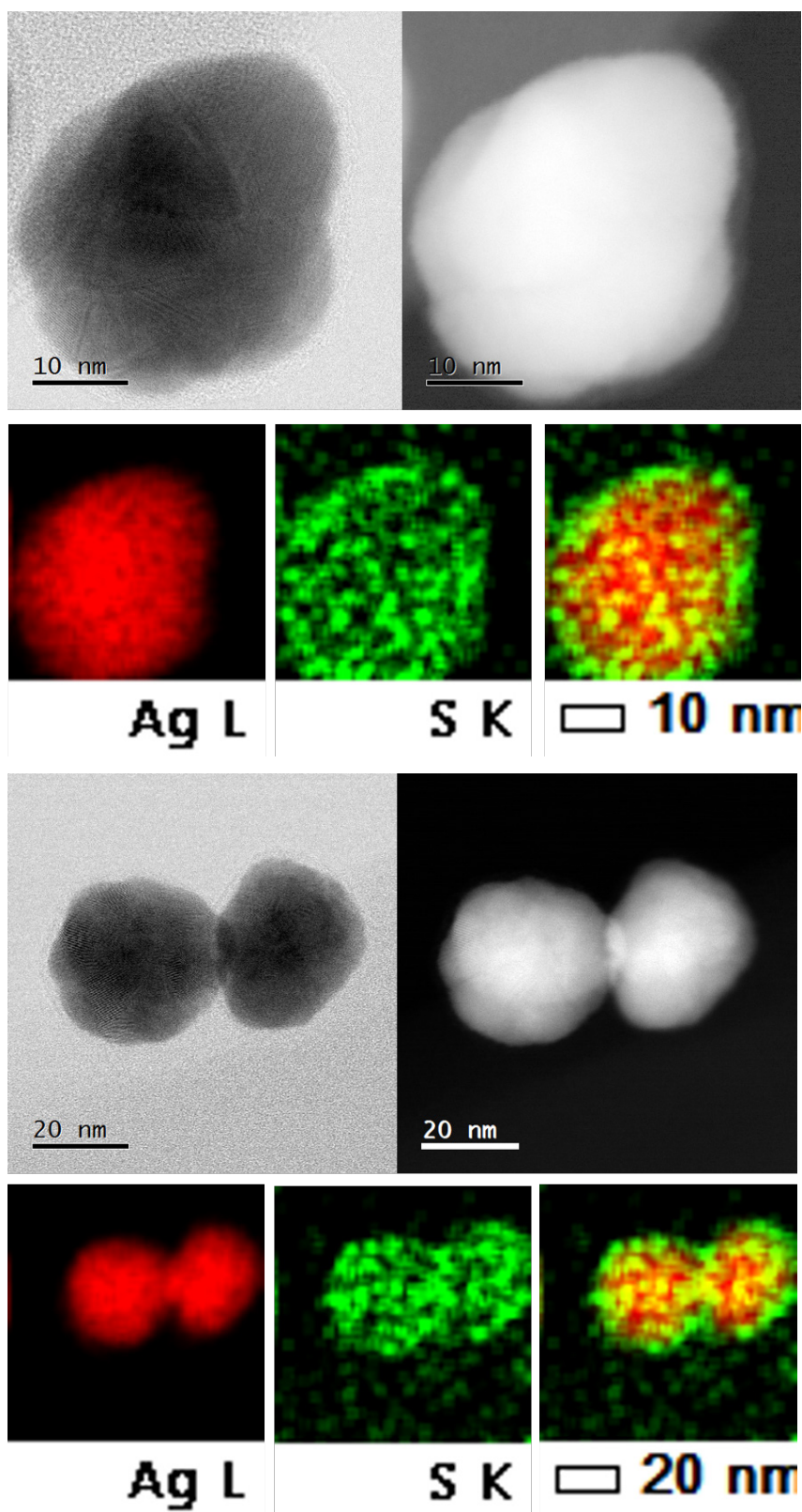
3.5. Appendix

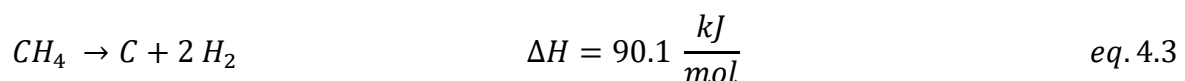
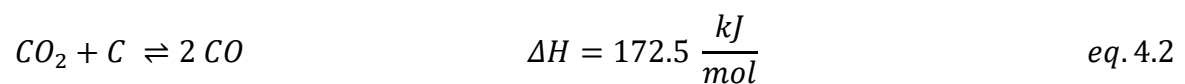
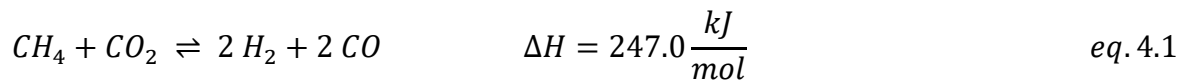
Figure A3.1. Additional TEM, STEM images and mapping of silver/silver sulfide core-shell particles. Sulfur (green) signals were observed around silver (red). Yellow color indicates overlap of silver and sulfur.

4. Supported Nickel Phosphide-Manganese Oxide Promoted Core-Shell Particles for DRM

4.1. Introduction

Depletion of crude oil due to continuously increasing energy demand requires a raw material change to meet future demands. An alternative feedstock to crude oil could be methane, which occurs in natural gas and thus, exists in enormous quantity on our planet.^[130] However, activation of methane and subsequent conversion to more valuable compounds is a challenging task.^[131,132] Producing syngas by endothermic reforming processes under high temperatures are a viable way to use methane.^{[133][134]} Besides commercial steam reforming, dry reforming of methane (DRM) with carbon dioxide, another greenhouse gas, is a sustainable alternative to produce syngas. DRM yields syngas with a H₂:CO ratio of 1, making it more suitable for the Fischer-Tropsch process compared to steam reforming. Another advantage of the DRM process is the direct application to flue gas without CO₂ separation.^[135] Recent reviews underline the high topicality of this process.^[136–140]

So far, no plant on an industrial scale has been used as the research for a viable catalyst is still ongoing.^[130] Besides expensive noble metals, nickel-based catalysts are considered promising for dry reforming of methane (equation 4.1) because of their high activity and low cost. However, using solely nickel will result in fast deactivation. Deactivation occurs mainly by particle sintering and carbon deposition on nickel particles due to the Boudouard equilibrium (equation 4.2) and methane pyrolysis (equation 4.3).^[141]



Particle size studies carried out by Han et al. showed that small nanoparticles are more active towards methane conversion and less susceptible for coke deposition.^[142] This implies, that stabilizing nickel nanoparticles to prevent sintering and reduce coke deposition is pivotal for a long-term stable catalyst.

The catalyst's performance can be increased by adding promoters.^[88] These promoters can interact with the active phase in different ways like changing electronical or morphological properties or block poisoning species from active sites. More details about the role of promoters in catalysis can be found in chapter 1. For DRM, the promoter should be able to block poisoning species, as coking is a severe deactivation source. To obtain stable catalysts for DRM, promoters like zirconia^[143,144], lanthan oxide^[145–147], ytterium oxide^[148,149], iron oxide^[150,151] and magnesia^[152] among others were tested in literature. Manganese oxide is another known promoter for nickel-based catalysts as it adsorbs CO₂ and partially blocks Ni sites which lead to much lesser carbon deposition resulting in a less pronounced deactivation.^[153] Not only the chosen metal/metal oxide, but also the method to distribute the promoter over the catalysts is decisive for performance increasement as described in the introduction. Manganese promoted nickel-based catalysts were produced by co-impregnation,^{[154][155]} sequential impregnation^[156] and co-precipitation.^[157] Guo et al. introduced manganese to nickel by co-impregnation on alumina and plasma treated all samples. They reported an increase in methane conversion of 10 % at 700 °C and ascribed the higher activity to the catalyst's anti-coking ability introduced with the manganese addition.^[154] Yao et al. compared co-impregnated and sequential impregnated Zr and Mn for nickel based catalysts with silica as support. The group showed, that the impregnation sequence plays a role for the final dispersion of metals, and hence for the activity. Furthermore, the dispersion influences the carbon species formed and therefore the deactivation behaviour of the catalyst.^[156] Littlewood et al. used the co-precipitation method to obtain a nickel manganese oxide species supported on silica. The catalyst showed stable methane conversion until 600 °C over many hours on stream, but deactivated quickly at higher temperatures.^[157]

Among supports, literature results indicate that γ -alumina seems to be the best choice for nickel-based catalysts.^[158] However, burying of active nickel in the support framework is another route of deactivation.^[159,160] In this case, nickel reacts with the support surface to form a catalytically inactive nickel aluminate species.

To exploit synergistic effects in a bimetallic catalyst as many interface sites as possible should be created. Considering this, core-shell particles are predestined to maximize the promoter effect. While silica and alumina coatings are numerous reported in literature, encapsulating nickel with promoting metal oxides like manganese oxide is a new research topic.^{[22][161,162]} Tian et al. conclude their review by stating it would be more attractive to synthesize the encapsulation structure for group VIII metals with catalysis-assisting oxides instead of silica, alumina or carbon.^[163] In this regard, a thin metal oxide shell would be effective against three deactivation sources, namely carbon deposition, sintering and nickel contact to γ -alumina leading to inactive nickel aluminate. Ideally, the used promoter would not decrease the catalyst's activity.

Various transition metal phosphides are known as active catalysts for different applications like hydrogen evolution reaction, hydrodesulfurization and hydroformylation of small olefins.^[164–167] For the colloidal synthesis approach high temperatures are needed and thus, a reaction between phosphorus stabilizers and nickel particles is likely to occur.^[168] To our knowledge, no experimental studies about nickel phosphide catalysts for DRM exist in literature. However, recently a DFT study on Ni₂P (0001) surfaces by Guharoy et al. was published. The group concludes that “the Ni₂P (0001) surface conserves the active characteristics of Ni surfaces toward the DRM reaction, but with increased resistance toward carbon formation in the relevant DRM temperature window”.^[169] Since phosphides can change electronic environments, they could act as an additional promoter for nickel-based catalyst in the DRM reaction.

In this thesis, the first synthesis of nickel phosphide manganese oxide core-shell particles as a precursor for a nickel based catalyst for dry reforming of methane process is reported. The core-shell particles are synthesized in a one-pot fashion. First, nickel nanoparticles are formed by thermal decomposition of nickel acetylacetonate and then coated via hot injection of a manganese oleate complex. During this step,

nickel nanoparticles convert to nickel phosphide. The core-shell particles are supported on γ -alumina by wet impregnation. Subsequent calcination was used to remove the stabilizer. For comparison a reference sample without manganese addition was also prepared by colloidal methods and tested for DRM.

After reduction of the catalysts before reaction, both catalysts were tested for DRM. The role of manganese and phosphorus as promoters regarding activity and stability in this reaction will be discussed. Therefore, both catalysts will be thoroughly analysed before and after the reaction.

4.2. Experimental

4.2.1. Synthesis of Colloidal Nickel Phosphide-Manganese Oxide Core-Shell Particles

Synthesis of nickel phosphide-manganese oxide core-shell particles was carried out using a Schlenk line under inert gas. Oleylamine (98 %), trioctylphosphine oxide (99 %) and dimanganese decacarbonyl (98 %) were purchased from Sigma Aldrich. Trioctylphosphine (97 %) and nickel acetylacetonate (95 %) were obtained from abcr. The γ -alumina support Puralox® was obtained from Sasol.

The synthesis of nickel phosphide nanoparticles was conducted as described in literature.^[170] In a 100 mL two neck round-bottom flask nickel acetylacetonate (700 mg, 2.7 mmol), trioctylphosphine oxide (25 g, 64.7 mmol) and oleylamine (9 mL, 27.4 mmol) were heated at 80 °C under reduced pressure ($5 \cdot 10^{-2}$ mbar) for 2 h. A color change from green to light blue was observed. After addition of trioctylphosphine (1.5 mL, 3.4 mmol) the reaction mixture was heated to 240 °C and held for 20 min. At 230 °C a color change from blue to black was observed, indicating the reduction of nickel(II) to nickel(0). In parallel, a manganese oleate complex was prepared as described in the literature.^[171] In a Schlenk flask, di-manganese decacarbonyl (150 mg, 0.51 mmol) was mixed with oleylamine (3 mL, 9.1 mmol) and heated at 100 °C for 1 h under inert conditions. The two neck round-bottom flask containing the nickel colloids was heated to 290 °C. The orange manganese oleate complex (1.6 mL) was injected to the hot reaction mixture with a syringe. The theoretical Ni:Mn molar ratio was 5.

Ethanol (100 mL) was added and the suspension was centrifuged at 9000 rpm for 30 min to collect the nanoparticles. The nanoparticles were redispersed in hexane (100 mL), again precipitated with ethanol and centrifuged. This washing step was repeated one more time before dispersing the nanoparticles in toluene (100 mL). Considering a full conversion the final dispersion concentration is 1.7 mg/mL.

4.2.2. Synthesis of Colloidal Nickel Phosphide Particles

For the reference material without manganese the synthesis was the same, but no manganese oleate complex was added after nickel phosphide formation. Still, the mixture was stirred for 30 min at 290 °C. The work-up of the synthesis went according to the core-shell particle synthesis.

4.2.3. Impregnation of Nickel Phosphide-Manganese Oxide Core-Shell Particles on Puralox®

Puralox®/ γ -aluminum oxide was activated in synair (20 % O₂ in N₂) at 550 °C for 3 h. In a round bottom flask, the dispersed nanoparticles were stirred at 600 rpm. To this dispersion, activated γ -aluminum oxide (3243 mg) was added to obtain a final theoretical loading of 5 wt % of nickel. The suspension was mixed for 20 h. After turning off magnetic stirring the black solid settled and the solvent was transparent. The black solid was filtered off and washed with toluene (2 x 30 mL). After drying at rt the material was calcined. The calcination temperature was 800 °C with a heating ramp of 5 K/min. The target temperature was held for 2 h in a synair (20 % O₂ in N₂) atmosphere. The reduction temperature was 850 °C with a gas composition of 5 % H₂ in N₂. Before catalytic testing, the catalyst was reduced at 500 °C in the reactor. The reference catalyst without manganese was pretreated in the same way.

4.2.4. Catalytic Screening

Catalytic testings were conducted at BasCat by Chengyue Guan. The catalysts were pressed and sieved into diameter fractions of 100-200 μ m. 133 mg of catalyst was loaded in a quartz tube with an inner diameter of 4 mm and fixed with quartz wool. To extend the catalyst bed, silica (400 mg) was added for dilution. The gas composition was He:N₂:CH₄:CO₂ 7:1:1:1 with a total flow of 80 mL/min. The final WHSV was 36,000 L/gh. Gas compositions at the exhaust were analyzed by online gas chromatography (GC) with an Agilent 7890A.

4.2.5. Colloids and Catalyst Characterization

Transmission electron microscopy (TEM) was carried out with a FEI Tecnai G² 20 S-TWIN with an equipped r-TEM SUTW Detector for electron dispersive x-ray spectroscopy. 25 μ L of sample (stabilized silver particles in water) were placed on a carbon coated copper grid. Then, the grid was dried at rt before put on the sample holder.

Further TEM measurements, STEM and STEM mappings were conducted with a JEOL JEM-ARM200CF electron microscope at the FHI. The samples were measured on carbon coated copper grid cells.

Elemental analysis was conducted with ICP-OES with a Varian 715 Emission Spectrometer for nickel quantification. Digestion of ICP-OES samples was done by stirring the sample (10-20 mg) in aqua regia (10 mL) for 16 h. After the solid settled, the supernatant liquid (5 mL) was diluted 1:1 with water (HPLC grade).

X-ray photoelectron spectroscopy (XPS) was measured on K-Alpha^{TM+} X-ray Photoelectron Spectrometer System from Thermo Scientific. The x-ray source was Al-K_α-radiation. For the measurement, the solid samples were pressed and put on carbon taps which were put in the sample holder for measurement. Survey spectra were run in the binding energy range of 0-1000 eV and high-resolution spectra of C1s, Ni2p, P2p and Mn2p were collected.

Temperature programmed reduction (TPR) was conducted with a Microtrac-BEL BelCat II setup. The sample was fixed with glass wool in a quartz glass setup and then put into the BelCat II setup. For the TPO measurement 180 mg of sample were used. The gas mixture was 10 % H₂ in N₂ with a total flow of 30 mL/min. The temperature was increased from 50 °C to 900 °C with 10 K/min.

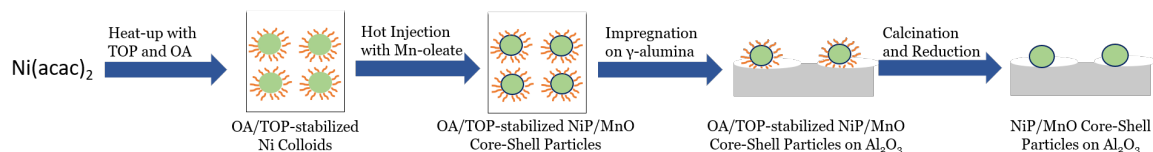
Nitrogen sorption analysis was performed at 77 K using a QUADRASORB SI system, which was equipped with an automated surface area analyzer. Before analysis, samples were degassed at 120 °C for 12 h. Specific surface areas (BET) were determined over a 0.05-0.30 P/P₀ range.

X-ray powder diffraction (XRD) patterns were recorded on Bruker D8 diffractometer with Cu K_α1 radiation ($\lambda = 0.154$ nm) equipped with scintillation counter.

4.3. Results

4.3.1. Synthesis and Characterization of Core-Shell Particles and Nickel Phosphide Colloids

For dry reforming of methane a stable, active and cost-efficient catalyst is desired. While encapsulation of nickel particles in silica and alumina is already known in literature, here an encapsulation approach with a promotional metal oxide is examined. The synthesis route of the catalyst is summarized in scheme 4.1.



Scheme 4.1. Scheme for the preparation of a colloid-based catalyst. First, the precursor is decomposed in presence of stabilizers (heat-up method). To the hot reaction mixture the manganese oxide precursor is added to give core-shell particles. After work-up, the colloids are supported via wet impregnation. Subsequent calcination and reduction gives the final catalyst.

Nickel-based nanoparticles were synthesized by the heat-up method. The nickel precursor nickel acetylacetonate was dissolved in a mixture of oleylamine, trioctylphosphine (TOP) and trioctylphosphine oxide (TOPO). After drying under reduced pressure, the mixture was heated up to 240 °C, whereby nickel nanoparticles were formed. To encapsulate the formed nanoparticles, the reaction mixture was heated up to 290 °C and a preformed manganese oleate complex was injected. Based on literature, at these temperatures phosphorus stabilizers react with nickel nanoparticles to give nickel phosphide.^[168] To check at which temperature this reaction takes place two experiments were conducted: One according to a literature source, where phosphorus stabilizers were used, but nickel nanoparticles were obtained, that was heated to 220 °C.^[172] The other one was heated to 290 °C, as needed for the hot injection of the manganese precursor complex.

XRD Analysis

The diffractogram (figure 4.1) shows that the synthesis from literature was reproducible, but at 290 °C the nickel phosphide phase was already formed. So far, there are no publications about activity of supported nickel phosphides in DRM. Besides evaluation of the phosphorus effect, the focus was on comparing nickel phosphide activity with and without manganese oxide shell.

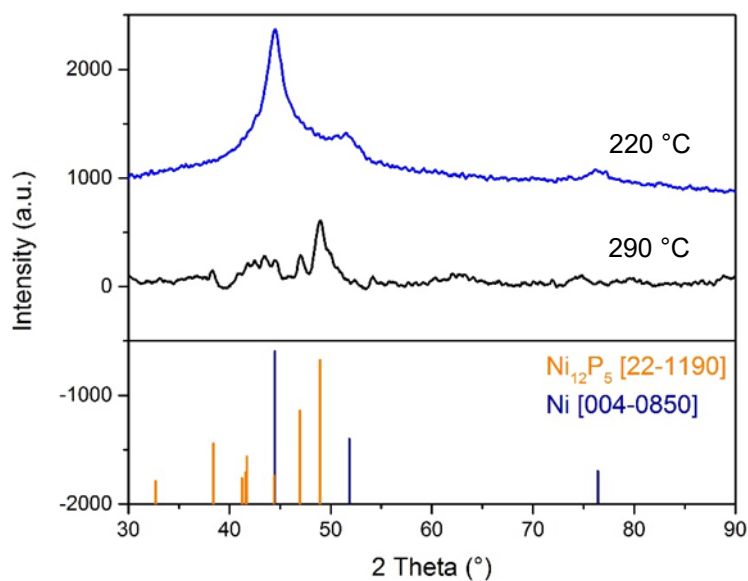


Figure 4.1. Comparison of measured diffractograms at different temperatures. At 220 °C all three reflexes can be assigned to the nickel phase. At 290 °C a complete conversion to nickel phosphide takes place.

After hot injection of the manganese precursor, the nanoparticles were purified, isolated and analyzed by XRD (figure 4.2). No manganese oxide reflexes were visible, which indicate a successful encapsulation, as homogeneously formed particles bigger than 3 nm would show manganese oxide reflexes if crystalline.^[171] All major reflexes (38.4 °, 41.6 °, 44.4 °, 46.7 and 48.9 °) can be assigned to the nickel phosphide phase (Ni_{12}P_5). Only the reflex at 44.4 ° could possibly be assigned to the nickel phase. However, due to an overlap with a nickel phosphide reflex, it is not determinable if metallic nickel is present in a small amount.

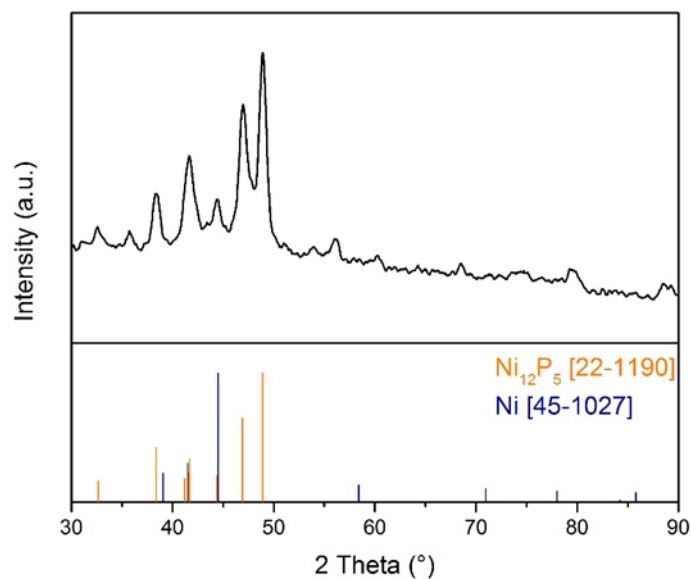


Figure 4.2. XRD diffractogram for colloidal particles after reaction (at 290 °C), work-up and isolation. All major reflexes can be assigned to the nickel phosphide phase.

TEM and EDX Analysis

TEM was used to analyze composition, size and structure of the nanoparticles (figure 4.3). The images show particles with a narrow particle size distribution with an average size of $16.3 \text{ nm} \pm 1.3 \text{ nm}$. All particles are nearly perfect spheres. Around the crystalline core a slightly lighter shell is visible, which is assumedly the manganese oxide phase.

The elemental composition of image 4.3A was examined by EDX (figure 4.3C). Carbon and copper signals are originating from the electron microscopy grid. As discussed before, the phosphorus signal originates from nickel phosphide nanoparticles. Quantification of the signals (table 4.1) shows a nickel to manganese atomic ratio of 3.5. In general, deviations from the educt ratio can occur, as EDX is a local analysis method. Furthermore, it is possible, that a small part of the manganese precursor formed manganese oxide nanoparticles by homogenous nucleation, which were not found during TEM or XRD analysis.

To confirm that the manganese EDX signal is originating from the manganese oxide shell around the nickel phosphide particles, the core and shell thicknesses of the

particles were measured and the volume was calculated. Detailed calculations and assumptions can be found in the appendix. The volume of the core and the shell were calculated with formulas for spheres and hollow spheres, respectively. 20 core-shell particles were measured with ImageJ software and the average was used for calculation. Based on these calculations the nickel manganese ratio is 3.2, which is a very good approximation to the EDX data.

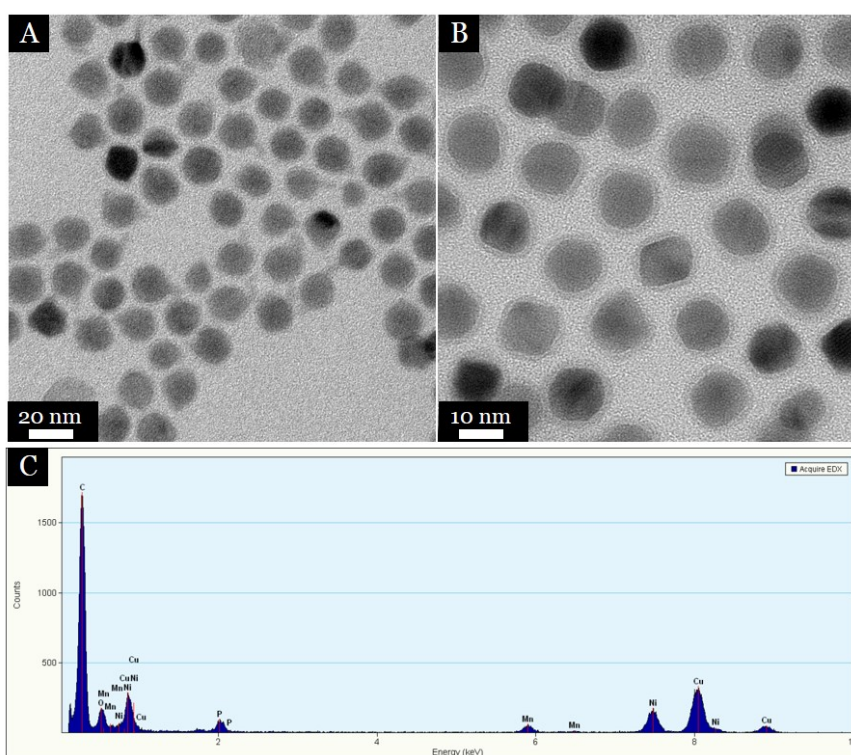
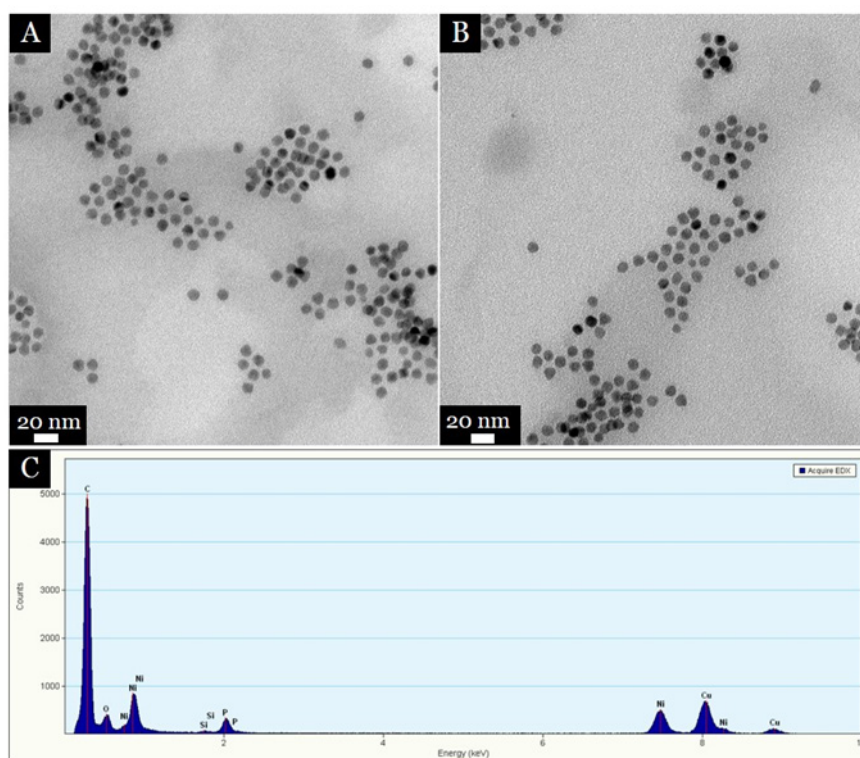


Figure 4.3. TEM and EDX analysis for colloidal particles after reaction (at 290 °C), work-up and isolation. A shell with higher brightness around the nickel phosphide particles can be observed. EDX measurements show a significant manganese signal.

Table 4.1. EDX quantitative analysis of nickel, manganese and phosphorus. Nickel to manganese ratio at the regarded position is 3.5.

Element	Weight %	Atomic %
Ni	45.02	22.61
Mn	11.5	6.17
P	10.00	9.52

For comparison, two images for the reference nanoparticles without manganese are shown with the EDX of the first image (figure 4.4). The particle size distribution is very narrow and thus, very similar to the core-shell particles. However, the particles are smaller with an average of $10.3 \text{ nm} \pm 1 \text{ nm}$ in comparison to $16.3 \text{ nm} \pm 1.3 \text{ nm}$ for the core-shell particles. As expected, the EDX spectrum shows signals assignable to nickel and phosphorus, but no manganese signal.

**Figure 4.4.** TEM and EDX analysis for colloidal particles after reaction without manganese addition (at $290 \text{ }^\circ\text{C}$), work-up and isolation. No shell is observable around the nickel phosphide particles and also the EDX results show no manganese signal.

4.3.2. Synthesis and Characterization of Supported Catalysts before DRM Test

Calcination Procedure

After successful nanoparticle synthesis, the next step is to support the colloids on γ -alumina. Therefore, the stabilized nanoparticles in toluene were mixed with the support by wet impregnation. After impregnation, the dark solid was separated from the solvent and washed thoroughly with toluene. To remove organic stabilizers, the sample was calcined. To monitor the decomposition of the organic stabilizers, a thermogravimetric analysis (TGA) in synair was performed (figure 4.5). From room temperature to about 500 °C a mass loss of about 8 % is observed. First, the solvents hexane and toluene were removed. Then, the stabilizers TOPO (boiling point: 212 °C), TOP (bp: 290 °C) and oleylamine (bp: 350 °C) decomposed. Due to intermolecular interaction with the metal particles and support, the decomposition temperature could be higher than the boiling point. The increase in mass from 550 °C to 630 °C can be assigned to oxygen uptake, probably caused by the reaction of nickel phosphide to nickel phosphate.

Although particle sintering above this temperature is probable, the calcination temperature was chosen according to the highest DRM reaction temperature, that is, 800 °C. This calcination temperature was also recommended in a review by Usman et al. to give the highest activity for nickel based catalysts.^[137]

Reduction Procedure

Based on literature results, the active phase for DRM is Ni(0).^[137,173] To study the reduction behavior of the sample, a temperature programmed reduction (TPR) was conducted (figure 4.5). The sample was reduced with 10 % H₂ in N₂ (total flow 30 mL/min) with a heating ramp of 10 K/min up to 900 °C. The diagram shows two major peaks at 410 °C and 680 °C, as well as a shoulder at 760 °C. The main reduction event starts at 520 °C. According to multiple publications, these signals can be assigned to the reduction of nickel phosphate, and different species of nickel oxyphosphates or nickel phosphides.^[174–176] These findings lead to the assumption, that after calcination nickel phosphate was mainly formed. Since a complete reduction of this phase was desirable, 850 °C was chosen as the reduction temperature.

According to literature, the first peak can be assigned to the reduction of supported nickel oxide to metallic nickel.^[177] Although nickel phosphate is mainly formed after calcination, the strong interaction between phosphates and the support, aluminum oxide, can lead to the formation of small amounts of aluminum phosphate and nickel oxide.^[178] Due to stabilization from the support, the reduction temperature is slightly shifted to higher temperatures compared to bulk nickel oxide.

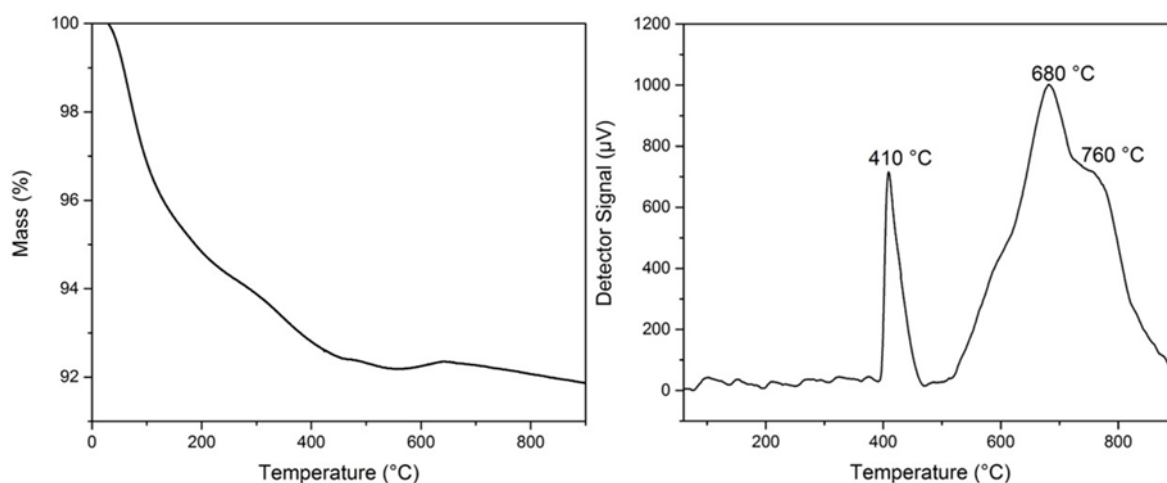


Figure 4.5. *Left:* TGA of freshly impregnated sample in synair (20 % O₂ in N₂). The oxidative atmosphere leads to decomposition of the stabilizers from rt to 500 °C. *Right:* TPR of the supported samples after calcination at 800 °C. Two distinct reduction events were observed. First, the reduction of nickel oxide to metallic nickel. Second, the reduction of nickel phosphate to nickel phosphide over several stages of different nickel phosphide species.

XRD Analysis

The composition of the calcined and reduced samples were examined by XRD (figure 4.6). The reflexes of the calcined sample can be assigned to the γ -alumina phase. No reflexes of nickel oxide, nickel phosphate or nickel phosphide phases can be found. The reason for that could be either small nanoparticles (< 5 nm), which could be the results of redispersion, or amorphous particles. Since XRD analysis of the colloids showed crystalline particles, the former reason is probably the case. For the reduced sample, nickel and nickel phosphide phases were detected. It was assumed that two processes happened during reduction. First, a reduction from nickel phosphate to nickel phosphide took place and second, the nickel phosphide was partially reduced to metallic nickel. Since the reaction runs under reducing atmosphere, a complete reduction of nickel phosphide to nickel with sufficient time on stream was expected. Alternatively, nickel oxide could be formed for the reason as described

above, that is, by separation of nickel phosphate to nickel oxide and the aluminum phosphate.

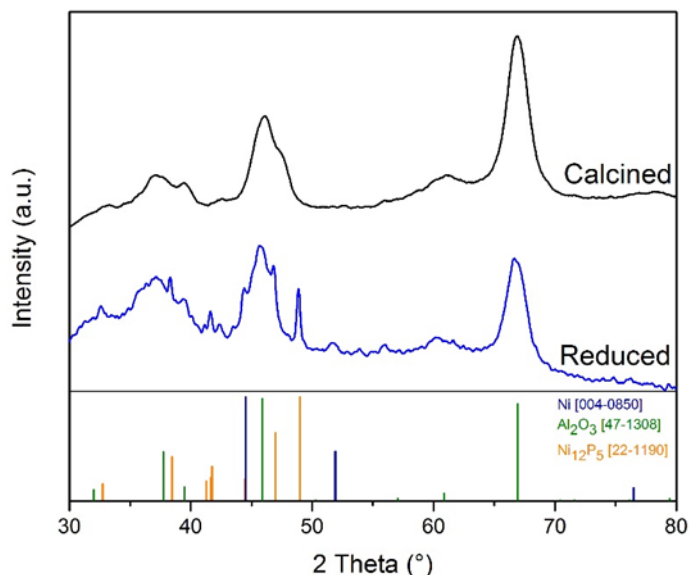


Figure 4.6. XRD of supported sample after calcination at 800 °C and subsequent reduction at 850 °C. After calcination the reflexes can be assigned to the alumina support, no nickel phosphide reflexes are observable due to a good distribution over the support. Reflexes of the reduced samples can be assigned to the support, nickel and nickel phosphides.

XPS Analysis

To further study the surface and oxidation state of the samples, XPS experiments were conducted (figure 4.7). The binding energy of nickel (Ni 2p_{3/2}) changes from 856.4 eV for the calcined sample to 852.4 eV for the reduced sample. According to literature, this indicates a change from Ni(II) to Ni(0).^[179] The binding energy for Ni(II) can vary significantly depending on the counteranion.^[179] After calcination at 800 °C, the presence of nickel phosphate species is probable and our XPS measurement are very similar to nickel phosphate spectra of Fa et al. with major peaks at 856.6 eV, that can be assigned to Ni 2p_{3/2} and the corresponding satellite peaks at 862.2-863.0 eV.^[180] The signal at 852.6 eV for the reduced sample could correspond to metallic nickel, but XRD data also shows the presence of nickel phosphide. Other groups analyzing nickel phosphides found binding energies at 852.4 eV or very close to that value and assign the signal to a Ni^{δ+} species.^[181,182] Thus, it is possible, that both species are present.

For the phosphorus (P 2p_{3/2}) signal of the calcined sample, one peak at 134.1 eV can be assigned to the P(V) oxidation state.^[183] After reduction, another peak at 129.6 eV appears, which can be assigned to P(-III) oxidation state originating from the Ni₁₂P₅ phase.^[184] This confirms the XRD findings that after reduction, nickel phosphide was present.

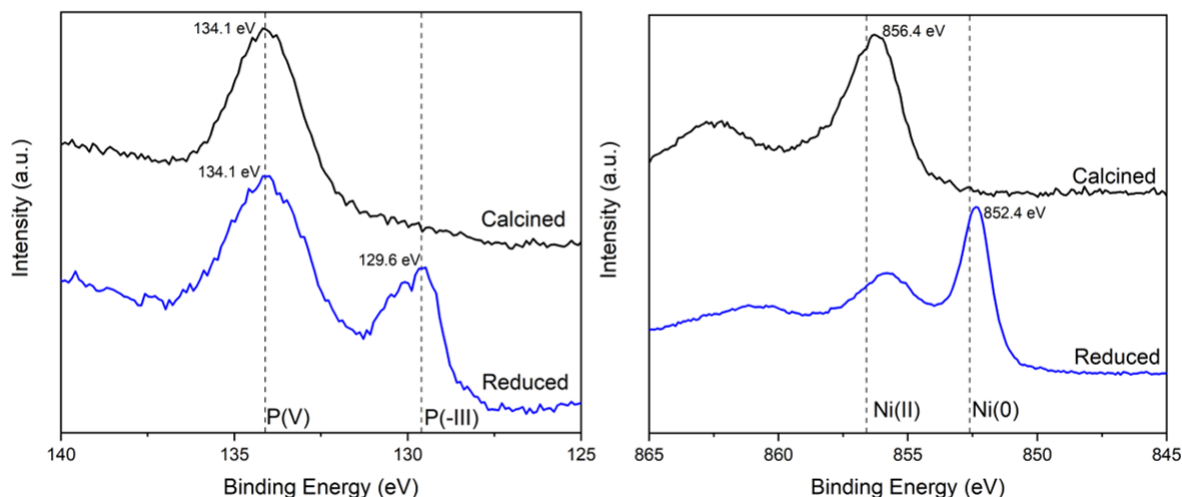


Figure 4.7. XPS measurements of supported sample after calcination at 800 °C and subsequent reduction at 850 °C. Left: Region for the phosphorus 2p signal. The calcined sample only shows a signal at 134.1 eV which can be assigned to P(V). This could be a well distributed phosphate species, either nickel or aluminum phosphate. The reduced sample shows an additional signal at 129.6 eV which can be assigned to P(-III), the phosphide species. This is in accordance with the XRD measurement. Right: Region for the nickel 2p signal. The signals for the calcined sample are shifted towards higher binding energy and thus, higher oxidation states in comparison to the reduced sample.

TEM Analysis

To examine the particle distribution on the support and particle sizes of the nickel-based catalyst, TEM and STEM studies were performed. Images of the calcined sample, including an elemental mapping, are shown in figure 4.8. Nickel-based particles are difficult to distinguish from the support. On elemental maps, nickel and manganese are very well distributed over the whole support. Furthermore, manganese concentrations near Ni are very high. In figure 4.8, a bigger particle can be seen on the right side. Here, based on the elemental map, a core-shell structure was observed. However, as other particles are difficult to identify, a final conclusion on the structure cannot be drawn from these images. Regarding the particle size, some sintered bigger particles are visible due to harsh calcination conditions.

For the reduced sample (figure 4.8) a sintering of the nickel phosphide particles is observed. While the manganese is still well distributed over the whole support, nickel phosphide particles partially sintered together. It can be observed that no manganese oxide shell is present around the nickel phosphide particles. Also small nickel phosphide particles (< 10 nm) can be found. These particles are probably stabilized in the support pores. A separation of core-shell particles of nickel and a highly oxyphilic metal like manganese was recently published from Margossian et al. where nickel iron core-shell particles were synthesized as precursors.^[185] The oxyphilic metal, in this case iron, is distributed all over the alumina after supporting and subsequent calcination while stabilizing the nickel. Such a metal oxide layer on the support prevents the nickel from forming the inactive nickel aluminate phase. Additionally, metal oxides of iron or manganese are known to react with surface carbon, thus decreasing coke formation on nickel metal.^[151,186]

For comparison, also the reference sample without manganese was analyzed by TEM (figure 4.9). Similar to the core-shell sample, a few sintered particles were observed. Nevertheless, also small stabilized particles are observable. Since distinguishing between thicker support areas and particles is difficult, an EDX was conducted in the marked area, in which nickel and phosphorus were measured.

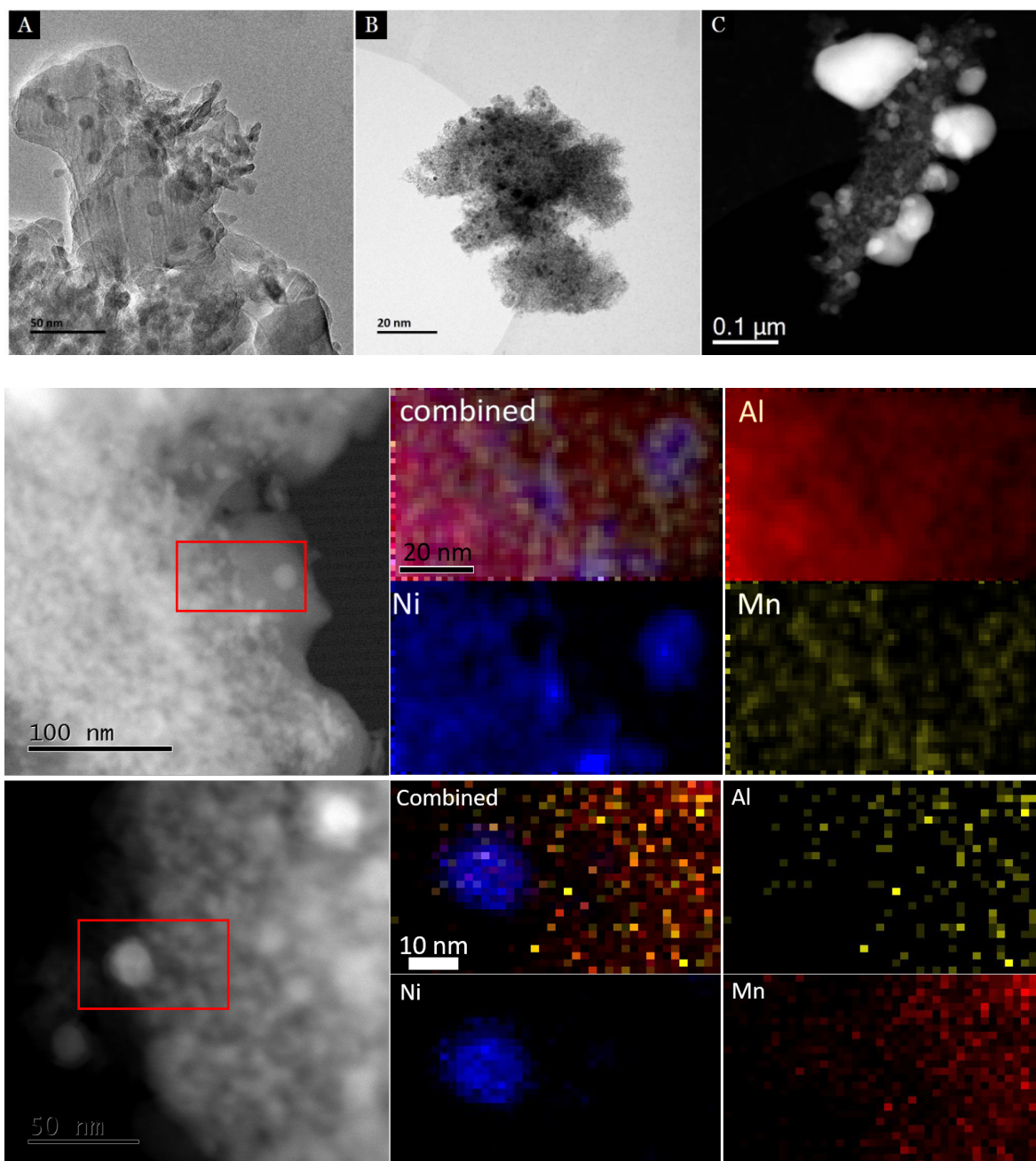


Figure 4.8. TEM, STEM and STEM mapping for the calcined and reduced samples. *Top:* For the calcined sample only few bigger particles are observable (A). The reduced sample shows a very heterogeneous particle size distribution. While many particles are well stabilized by the support (B), also bigger agglomerates at the support edges form (C). *Middle:* Mapping of calcined sample shows a very good distribution of nickel (blue) and manganese (yellow). Manganese concentration is higher near nickel. *Bottom:* Manganese (red) is still well distributed over the support and near nickel (blue) while nickel tends to form bigger particles after reduction.

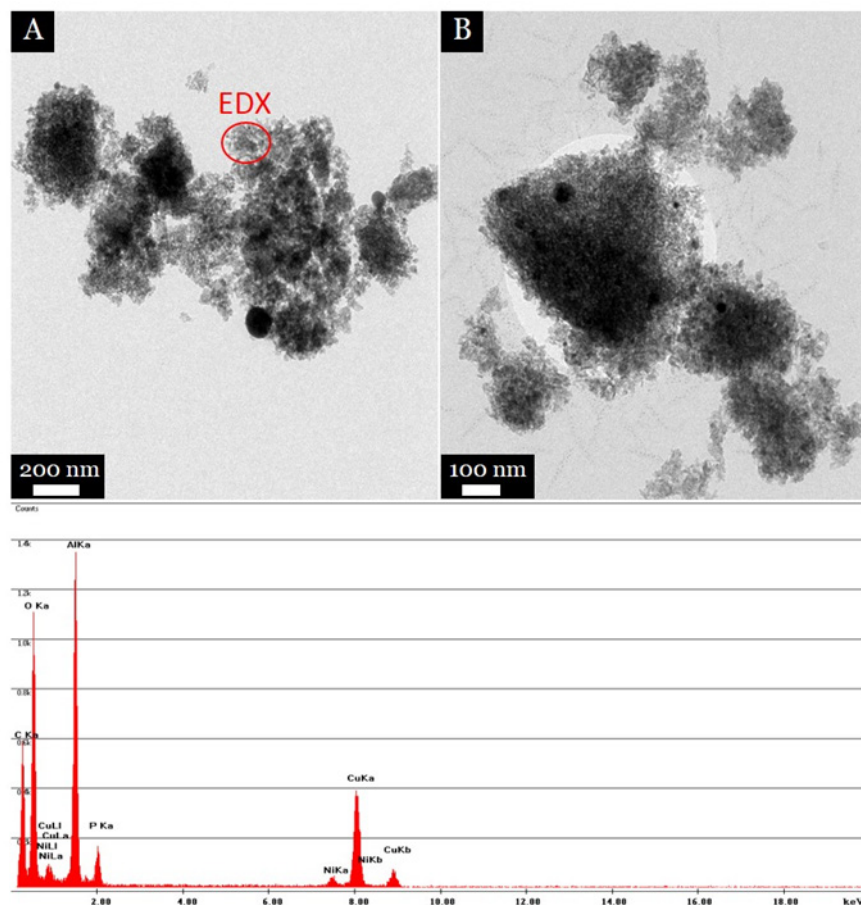


Figure 4.9. TEM images of the reference nickel phosphide sample without manganese after reduction. The sample shows a heterogeneous particle size distribution. While many particles are well stabilized by the support, also bigger agglomerates are observable. At some positions it is difficult to distinguish between thicker support and particles. However, even at the lighter position (red circle) EDX analysis confirms nickel presence.

ICP + BET Analysis

To classify the catalytic performance and compare the catalyst to others, the nickel loading was quantified by ICP-OES experiments. The sample was digested by stirring for 16 h in aqua regia and diluted before measurement. The manganese containing sample has a slightly higher nickel loading of 2.36 wt% compared to 2.16 wt% for the reference sample. This difference has to be taken in account when discussing performance results in the next part. Surface area was determined by nitrogen physisorption for both reduced catalysts (figure 4.10). Comparing to the pure support surface area of 189 m²/g, the surface area for both catalysts is decreasing after colloid deposition. The core-shell sample has a surface area of 153 m²/g, whereas the surface area of the reference sample is 134 m²/g. Since the loading is

quite similar, higher surface area is probable due to a better dispersion for the sample with manganese. Properties for the supported nickel phosphide manganese core-shell catalyst as well as the reference sample without manganese are presented in table 4.2. To simplify the discussion, the nickel phosphide is abbreviated by “NiP” and the manganese oxide shell “MnO”, although the phases are not exactly determined.

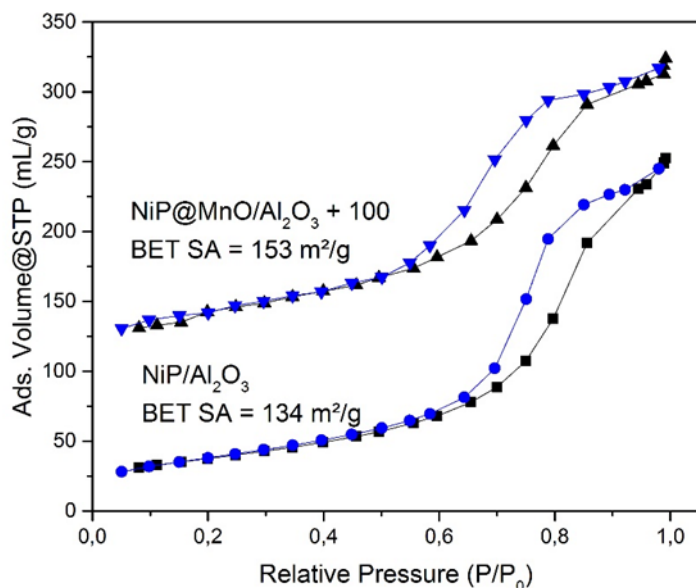


Figure 4.10. Nitrogen physisorption results for NiP@MnO/Al₂O₃ (with +100 offset) and NiP/Al₂O₃ after reduction at 850 °C. Both samples are type IV isotherms, typical for mesoporous materials.

Table 4.2. BET Surface area and nickel loading for NiP@MnO/Al₂O₃ and NiP/Al₂O₃ after reduction at 850 °C. Nickel loading and surface area are slightly higher for the manganese containing sample.

Sample	Ni loading [wt%]	BET SA [m ² /g]
BC1171 (NiP@MnO/Al ₂ O ₃)	2.36	153
BC1228 (NiP/Al ₂ O ₃)	2.16	134

Based on the analytics, a summary for the chemical structure of the catalyst can be given. The manganese oxide is well distributed over the whole support, which means it is also in contact with the nickel/nickel phosphide and can thus, act as a promoter. However, no core-shell particles are present anymore. Parts of the nickel are present as nickel phosphide, which was expected to be reduced to metallic nickel during the reaction. The role of nickel phosphide as well as the phosphorus on the support is

unknown as there are, at least to our knowledge, no publications with experimental background in the DRM literature.

4.3.3. DRM Performance Test

The catalytic performance of synthesized catalysts for dry reforming of methane was measured at BasCat by Chengyue Guan. Before testing, the catalysts were reduced in the reactor at 500 °C to exclude the presence of nickel oxide. The temperature was varied from 500 °C to 800 °C in 100 °C steps and was held for 5 h at each temperature. The WHSV was set to 36,000 h⁻¹ and then increased for a long-term measurement at 800 °C. The dry reforming of methane is limited by thermodynamic reaction equilibrium (figure 4.11). With higher temperatures the equilibrium is shifted towards the products (see equation 4.1.). An increase in WHSV decreases the conversion so that activation/deactivation phenomena could be explained.

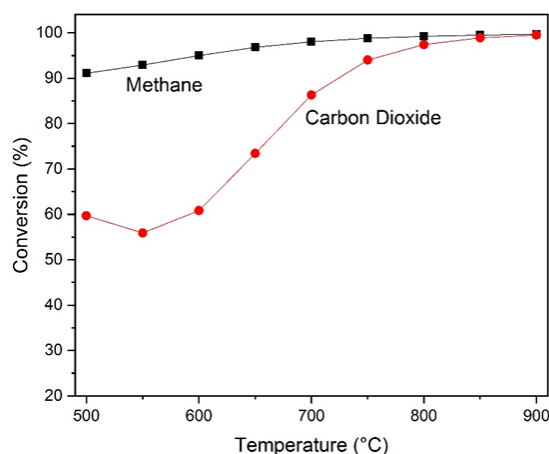


Figure 4.11. Thermodynamic equilibrium with maximum methane and carbon dioxide conversion at 1 bar for different temperatures as calculated by Dr. Benjamin Frank. A reaction limitation is based on carbon dioxide conversion.

The carbon dioxide conversion was always a bit higher than the methane conversion due to the Boudouard equilibrium and reverse water-gas shift reaction, but linear to the methane conversion (figure 4.12).

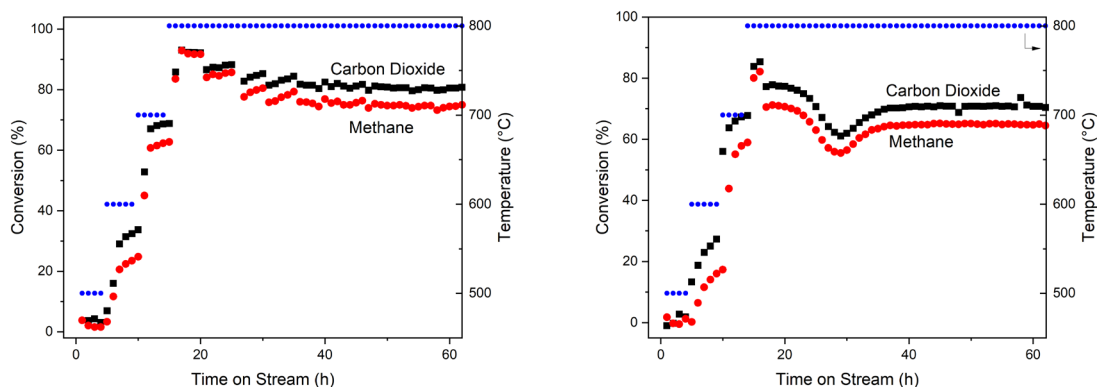


Figure 4.12. Methane and carbon dioxide in comparison for NiP@MnO/Al₂O₃ (left) and NiP/Al₂O₃ (right). Carbon dioxide is always converted at a higher percentage due to the Boudouard equilibrium and the reverse water-gas shift reaction. The WHSV is gradually increased at 800 °C, which leads to decreasing conversions for both catalysts.

Thus, it is sufficient to compare only the methane conversion. At every temperature NiP@MnO/Al₂O₃ conversion was higher compared to NiP/Al₂O₃ (figure 4.13). For both samples the highest conversion was observed at 800 °C. NiP@MnO/Al₂O₃ converted 93 % methane while NiP/Al₂O₃ showed a methane conversion of 82 %. If comparing the performance per gram nickel, both samples are very similar in methane conversion. During temperature increase from 500 °C to 700 °C for both samples an activation within each held temperature was observed. A stronger activation was detected for NiP/Al₂O₃, e.g. at 600 °C the conversion was increasing from 11 % to 19 % within 5 h on stream. A reason for the activation could be the gradual conversion of nickel phosphide to metallic nickel under the reducing atmosphere. This would mean, that phosphide addition is not beneficial for nickel-based catalysts regarding methane conversion.

The activation differences are due to manganese presence. Manganese is also reduced from higher valent manganese (Mn³⁺ or Mn⁴⁺) to Mn²⁺, thus the reducing atmosphere is weakened. Furthermore, manganese oxide can also reoxidize adjacent nickel species while in higher valent states.

The WHSV was increased at 800 °C, which resulted in decreased methane conversion to 74 % for NiP@MnO/Al₂O₃ and 65 % for NiP/Al₂O₃. The conditions were held for 40 additional hours to examine the long-term stability of both catalysts. After 40 h, the conversion for both samples decreased by about 3 %. Most literature publications concerning DRM do not show long-term studies, but only 20 h time on

stream, which makes it difficult to compare the results from this thesis with literature. However, even when comparing to 20 h measurement of other nickel/manganese oxide catalysts, the catalysts in the present work showed a very good stability.^[157] Since the manganese oxide addition showed no influence on the final activity, the addition of phosphorus is probably the reason for the increased stability. Important experimental values for both catalysts are summarized in table 4.3.

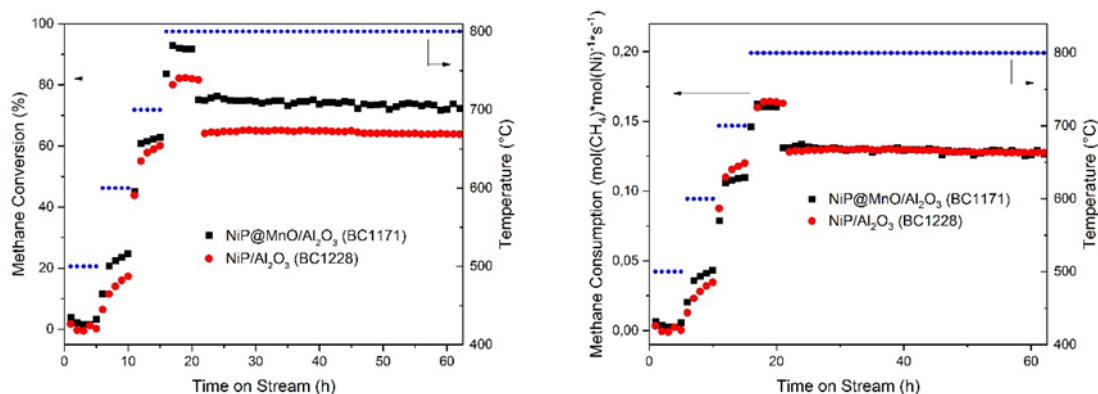


Figure 4.13. Methane conversion and methane consumption in comparison for NiP@MnO/Al₂O₃ and NiP/Al₂O₃. If the nickel amount is taken into account, both catalysts show a similar performance.

Table 4.3. Stability indicators with initial activity and activity after 40 h regarding methane conversion and methane consumption. Methane consumption was calculated with the assumption of an ideal gas. The input gas volume was multiplied with ideal gas volume and divided by the nickel amount.

Sample	Initial Methane Conversion @ 800 °C [%]	Methane Conversion after 40 h @ 800 °C [%]	Initial Methane Consumption @ 800 °C [mol(CH ₄)*mol(Ni) ⁻¹ *s ⁻¹]	Methane Consumption after 40 h @ 800 °C [mol(CH ₄)*mol(Ni) ⁻¹ *s ⁻¹]
NiP@MnO/Al ₂ O ₃ (BC1171)	74	71	0.133	0.128
NiP/Al ₂ O ₃ (BC1228)	65	62	0.129	0.127

4.3.4. Characterization of Spent Catalysts

Using various analytical methods like TG-MS, XRD, XPS and STEM the catalysts performance and activation/deactivation phenomena during the reaction were investigated.

Promotional manganese oxide was added to reduce coke formation on the final catalyst. Quantification of the deposited coke on the catalysts was determined by thermogravimetric analysis coupled with a mass spectrometer (TG-MS) (figure 4.14). Oxygen in the gas mixture burns carbon to carbon dioxide ($m/z = 44$), which is monitored by mass spectrometry. As coke is mostly deposited on nickel, the metal loading is crucial for interpretation of the results. Comparing the samples with and without manganese, the absolute mass loss for the sample without manganese is slightly higher (5.7 %) compared to the sample with manganese (4.2 %). Additionally, the nickel content for the sample with manganese is higher, therefore less coke is deposited per nickel due to the presence of manganese (table 4.4). In the performance test for 60 h this had no influence on the activity. However, for longer run time this should have a beneficial effect for the manganese containing sample.

Table 4.4. Comparison of nickel loading, coke formation as measured by TG-MS and the resulting coke formation per g Ni. Manganese addition results in 35 % less coke deposition on the catalyst.

Sample	Ni loading [wt%]	Coke formation [%]	Coke formation per g Ni [g]
NiP@MnO/Al ₂ O ₃ (BC1171)	2.36	4.2	1.78
NiP/Al ₂ O ₃ (BC1228)	2.16	5.7	2.64

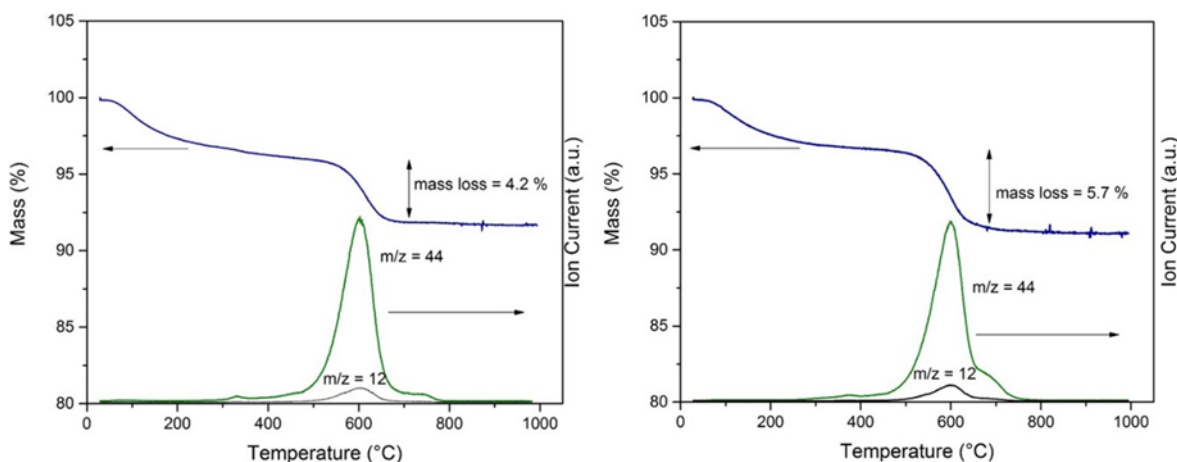


Figure 4.14. TG-MS analysis of NiP@MnO/Al₂O₃ (left) and NiP/Al₂O₃ (right) spent samples. M/z = 44 shows the signal of carbon dioxide, which is the main product after coke oxidation.

XRD Analysis

The spent catalyst with manganese was also studied by XRD (figure 4.15). Before the DRM reaction, metallic nickel as well as nickel phosphide were present. The reflexes of the diffractogram can be assigned to the support, γ -alumina and two reflexes (at 44.5° and 51.9°) can be assigned to metallic nickel. The silica reflexes originate from the inert material, which is added to the catalytic bed. The sharpness of the reflexes indicate big particles. Sintered particles are caused by the long time on stream and harsh DRM conditions. The presumption that the nickel phosphide phase will be converted to metallic nickel under reducing atmosphere during the DRM reaction was confirmed by XRD.

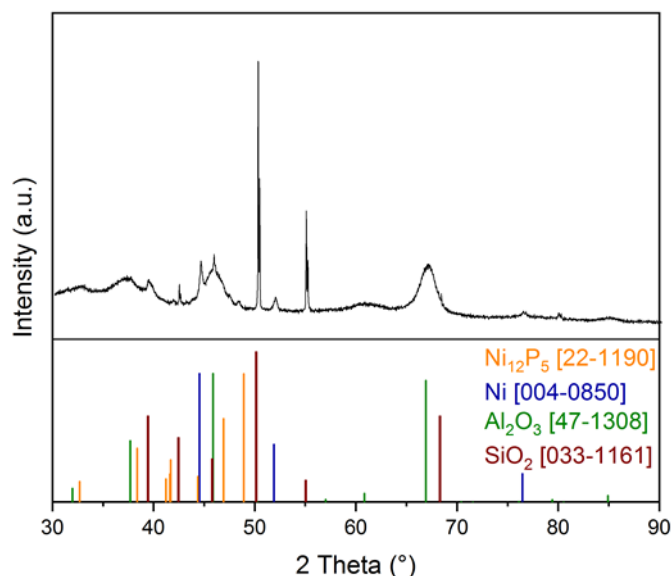


Figure 4.15. XRD of the spent NiP@MnO/Al₂O₃ sample. After reaction nickel phosphide was converted to metallic nickel due to the reducing atmosphere. The silica reflexes originate from the inert material, which is added to the catalytic bed.

XPS Analysis

To determine the oxidation state of the catalyst's surface after catalysis, XPS was carried out (figure 4.16). The phosphorus (P 2p_{3/2}) peak at 129.5 eV disappeared when compared to the reduced sample. This peak was assigned to the phosphide species from nickel phosphide. Confirming the XRD results, the nickel phosphide phase is reduced to metallic nickel during the reaction. The peak at 134.1 eV assigned to P⁵⁺, probably an phosphate species, is still present. A reason for that could be that a phosphate species is formed with the oxygen from the support.

The nickel (Ni 2p_{3/2}) peak signal is shifted slightly from 852.4 eV to 853.0 eV when compared to the reduced sample indicating at least a partial oxidation to Ni(II) species known from literature.^[187] Comparing the binding energy of calcined and spent samples (figure 4.7.) reveals that the formed species is not nickel phosphate, because the binding energy is much lower for the spent sample (856.4 eV to 853.0 eV). This would support the assumption that the phosphate bound to the support during the catalytic test. A peak deconvolution could not be performed due to poor signal to noise ratio.

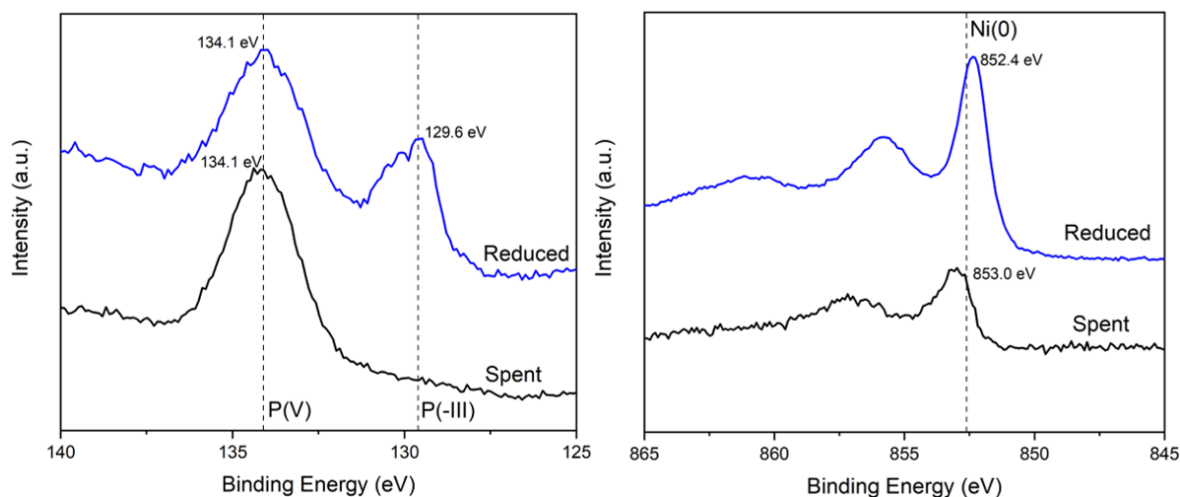


Figure 4.16. XPS measurements of spent NiP@MnO/Al₂O₃ sample. *Left:* Region for the phosphorus 2p signal. The signal at 129.6 eV was not detected for the spent signal. This is in accordance with the XRD results, that the phosphide species reacted. The phosphate species is still present. *Right:* Region for the nickel 2p signal. The signals for the spent sample are shifted towards higher binding energy and thus, higher oxidation states in comparison to the reduced sample.

TEM Analysis

To examine the sintering process of the nickel particles during reaction TEM and STEM analyses were carried out (figure 4.17). Despite 65 h time on stream and temperatures up to 800 °C, the particles only grew to a certain extent. Some particles were detached from the support. In these cases much bigger particle sizes can be observed. An explanation could be that particles which sintered on the support through particle migration and coalescence were detached from the support surface. These particles also show a carbon shell around the center. This is in line with literature publication showing that smaller nickel particles are not as prone to coke formation as bigger particles.^[142] Line scans also show that bigger particles do not contain phosphorus (figure 4.17 D-F).

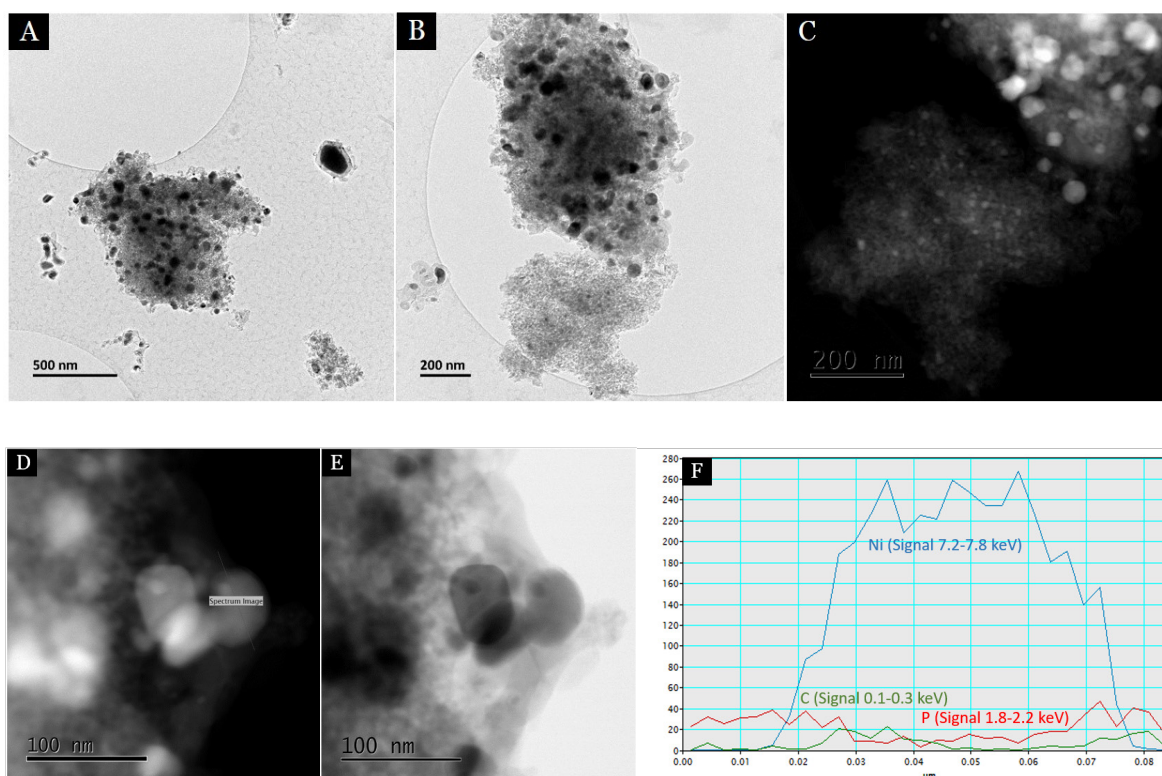


Figure 4.17. TEM and STEM measurements of spent NiP@MnO/Al₂O₃ sample. The spent sample shows a very heterogeneous particle size distribution. Some particles are well stabilized by the support (C), but the majority of particles sintered to bigger agglomerates. Some particles are detached from the support and show a thick carbon shell. Line scan of supported particles shows no phosphorus signal (D-F).

In general, the particles sintered after each step. The particle size distributions in figure 4.18. reveal this development for the catalyst with manganese addition. During calcination, particles redisperse and become better distributed over the support. After reduction, many bigger agglomerates form and during DRM reaction the particle size distribution becomes very broad.

The spent reference sample showed a similar result in TEM analysis (figure 4.19). More sintered nickel based particles were formed, especially non-supported or at the edge of the support. Still, small particles stabilized by support pores were present. In this region, the EDX spectrum showed the presence of Ni and P. This could indicate, that phosphorus helps to stabilize small nickel particles on the support. In contrast to that, line scans of bigger particles showed no phosphorus (figure 4.17). Furthermore, carbon nanotubes and other carbon depositions were observed.

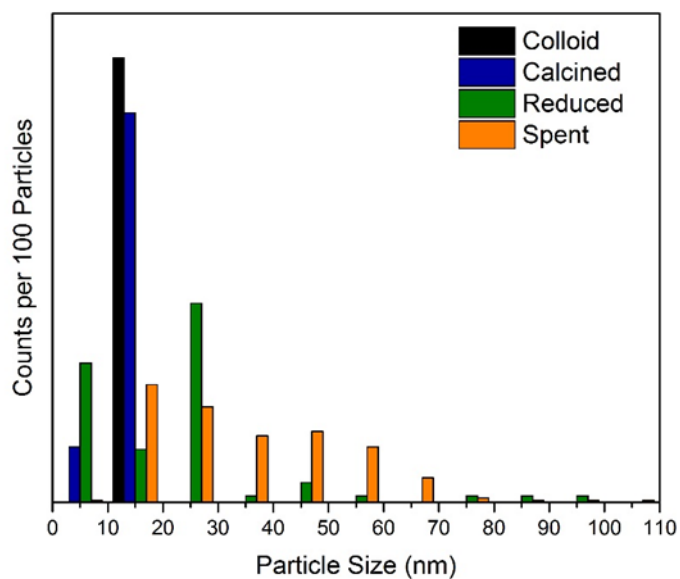


Figure 4.18. Particle size distributions after colloidal synthesis and after calcination, reduction and reaction of the supported nickel phosphide manganese oxide core-shell particles.

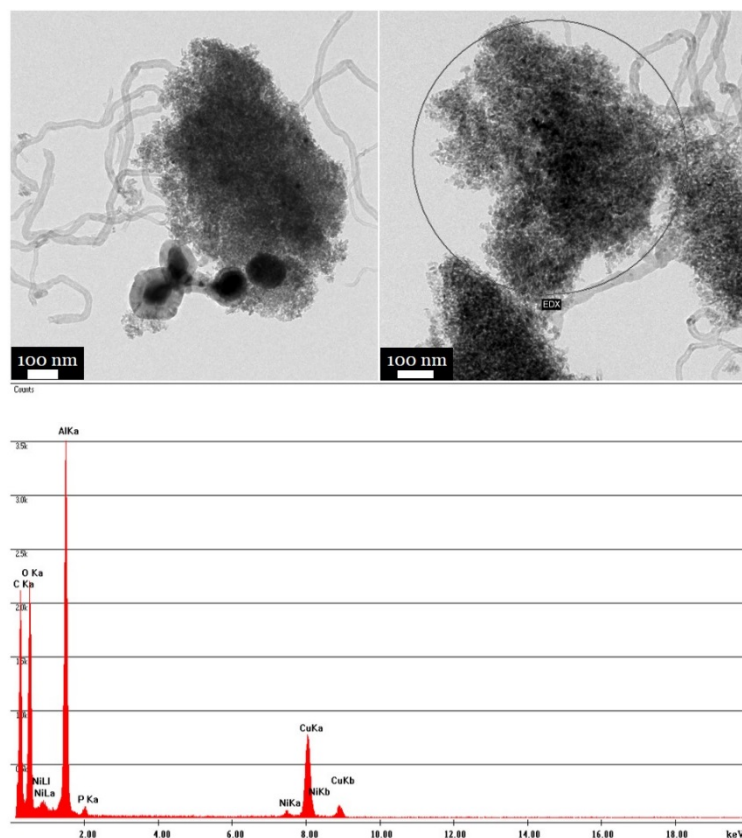


Figure 4.19. TEM and EDX measurements of spent NiP/Al₂O₃ sample. The spent sample shows a very heterogeneous particle size distribution similar to the manganese containing sample with small particles confirmed by EDX measurements but also sintered particles with a carbon shell.

4.4. Conclusion

In conclusion, manganese oxide encapsulated nickel phosphide nanoparticles were prepared by coupling the heat-up method to generate nickel nanoparticles and the hot injection method to give core-shell particles. The synthesis was conducted in a one-pot fashion making it a fast procedure to produce core-shell nanoparticles. As the next step, the synthesized core-shell nanoparticles were supported on γ -alumina and subsequently calcined and reduced. By STEM analysis a distribution of manganese oxide over the whole support was observed with high concentrations near nickel phosphide particles after calcination. In similar fashion, nickel phosphide nanoparticles were synthesized, supported on γ -alumina and pretreated for the DRM reaction.

Catalytic testing showed that both samples, with and without manganese, were fairly stable for 65 h time on stream in comparison to other literature publication despite harsh reaction conditions.^[157] The sample with manganese needed longer time for activation compared to the reference sample. It was assumed, that manganese oxide slows down the conversion of nickel phosphide to metallic nickel. TG-MS characterization revealed less carbon deposition for the manganese containing catalyst. Since coke formation is a major deactivation source, it can be assumed that manganese addition leads to longer longevity of the catalyst. During synthesis nickel phosphide formation was observed but after reduction and catalysis under reducing atmosphere stepwise transformation to metallic nickel was observed by XPS and XRD analysis. After characterization of the spent catalysts with XPS and TEM, it was assumed that a phosphate species is still present on the support. This species could be the key for the good long-term stability of both catalysts. To confirm this assumption more studies would be necessary.

With the presented approach, core-shell particle synthesis was used as another method to bring promoters in close proximity to the active metal/metal oxide. The used synthesis procedure can be applied to other metal/promoter pairs and hence, can also be used for preparing catalysts for different reactions. Desirable would be a reaction with mild conditions to keep the core-shell structure intact and therefore maximize the synergistic effect.

4.5. Appendix**Table A4.1.** Boudouard-equilibrium at different temperatures. From David R. Lide: *CRC Handbook of Chemistry and Physics*, 90th Edition, Taylor & Francis, **2009**.

Temperature [°C]	Amount CO ₂ [%]	Amount CO [%]
450	98	2
600	77	23
700	42	58
800	6	94
900	3	97
1000	1	99

Table A4.2. EDX calculations for fraction of core to shell ratio. Particles were measured with the imageJ software.

Number	Inner diameter [nm]	Total diameter [nm]	Inner radius [nm]	Total radius [nm]	Total Volume	Shell Volume	Fraction Total Volume/Shell Volume
1	14.21	15.62	7.11	7.81	1995.84	492.82	4.05
2	16.23	17.77	8.12	8.88	2936.08	695.94	4.22
3	14.95	16.30	7.47	8.15	2268.41	519.93	4.36
4	15.68	17.07	7.84	8.53	2603.43	583.35	4.46
5	15.81	17.53	7.91	8.77	2821.10	751.16	3.76
6	14.54	16.81	7.27	8.41	2487.59	877.09	2.84
7	15.09	17.05	7.55	8.53	2595.66	795.09	3.26
8	13.42	15.24	6.71	7.62	1853.70	587.08	3.16
9	13.86	15.66	6.93	7.83	2012.36	619.79	3.25
10	15.37	17.34	7.69	8.67	2730.84	829.67	3.29
11	10.24	12.08	5.12	6.04	922.77	361.05	2.56
12	15.15	17.16	7.57	8.58	2643.45	824.20	3.21
13	13.53	15.74	6.76	7.87	2041.80	746.38	2.74
14	15.40	16.91	7.70	8.46	2531.80	618.73	4.09
15	13.18	15.44	6.59	7.72	1927.64	729.93	2.64
16	15.45	17.68	7.73	8.84	2894.63	962.87	3.01
17	15.56	17.34	7.78	8.67	2728.01	755.08	3.61
18	14.89	16.79	7.44	8.39	2476.95	749.79	3.30
19	14.08	15.83	7.04	7.91	2076.24	614.71	3.38
20	14.29	16.29	7.14	8.15	2263.40	736.14	3.07
21	13.73	14.96	6.87	7.48	1754.45	398.34	4.40

5. Mesoporous Zirconium Oxide as Novel Support for Dry Reforming of Methane

5.1. Introduction

Ordered mesoporous silica materials like MCM-41, SBA-15 and KIT-6 were discovered in the 1990s and 2000s.^[188–190] Since then, these materials have been used for multiple applications like catalysis, gas adsorption and many more in research.^[191–195] High surface area, tunable pore sizes and high thermal stability are some of the attractive properties of these materials. In heterogeneous catalysis, a higher surface area of the support leads to a better dispersion of the active material and thus, to higher activity in most cases. Therefore mesoporous silica materials are a popular support in the catalytic research community.^[196–199] Over the years, the synthesis procedure was extended to many different metal oxides.^[200,201]

Synthesis of mesoporous silica or metal oxides can be carried out in two different ways. On the one hand, the soft template method, where used templates are amphiphilic molecules that form micelles in aqueous solution. After addition of the oxide precursor, the hydrolysis and consequently the formation of the oxide around the micelles takes place. Subsequent calcination removes the template and produces a porous material with pore sizes corresponding to the diameter of the micelles. By varying the type of the amphiphilic molecule, it is possible to tune the pore size.

For the hard template or nanocasting method a nanostructured solid, such as mesoporous silica, is used as template.^[202–204] The precursor of the desired metal oxide is dissolved and deposited by impregnation on the template. After successful impregnation and crystallization, the template is removed by calcination or selective dissolution, e.g. in hydrofluoric acid or sodium hydroxide for silica templates. The desired material is obtained as a replica of the used template. The most distinct advantage in synthesis of metal oxides by nanocasting compared to the soft template method is the possibility of a heat treatment at high temperatures. Due to the presence of the template, the desired metal oxide can form and crystallize. In contrast, a heat treatment with soft templates would lead to a pore collapse and hence, a decrease in long-range order and surface area.^[205]

Zirconium oxide is known as a promoter for nickel-based catalysts in the dry reforming of methane. According to Jing and Zheng zirconia improves the nickel dispersion.^[206] Increasing the nickel dispersion improves catalytic performance and reduces sintering behavior as previously described in chapter 4. Studies by Albarazi et al. show that zirconia in combination with ceria reduces coke by introducing higher oxygen mobility.^[207] Zirconia is known as an amphoteric material where oxygen exchange occurs rapidly. Rezaei et al. synthesized a high surface area zirconia support by the soft template method.^[208] The BET surface area after calcination was 174 m²/g for the pure support. The nickel/zirconia catalyst showed comparatively stable activity for 50 h on stream at 700 °C with nickel loadings between 5 and 10 %.

Based on these results, using zirconia could improve the activity of nickel-based catalysts. To increase the nickel dispersion, mesoporous supports could be used. However, methane activation requires very high temperatures of 600-800 °C. At these temperatures, the pore structure of most mesoporous materials collapses and therefore enclose the active nickel particles. This leads to deactivation of the catalyst. As a consequence, a mesoporous support that is stable at high temperatures and has a good interaction with the active nickel is desirable.

In our group, hard templated mesoporous manganese oxide was already tested as support, but was not stable at high temperatures. In this study high-surface area mesoporous zirconia with KIT-6 as a hard template was synthesized. This material was used as nickel support for dry reforming of methane. To compare the activity of this novel catalyst a reference sample was synthesized with Puralox®, a γ -alumina, as support. Alumina is a regularly used oxide support for nickel-based catalysts in the DRM reaction.^[209–213]

5.2. Experimental

The synthesis of the zirconia support was based on the hard template method described in the introduction. So far, hard templated zirconia was only synthesized with SBA-15 template by Liu and Baker.^[214] The reported synthesis in this thesis is based on this publication, but with KIT-6 as the hard template.

5.2.1. Synthesis of Mesoporous KIT-6

Mesoporous KIT-6 silica was prepared as follows: Pluronic P123 (18 g, average M ca. 5900 g/mol) was dissolved in HPLC water (660 mL) and conc. Hydrochloric acid (36 mL, 432 mmol). The solution was stirred for 5 h at 35 °C. After addition of 1-butanol (22.2 mL, 242.6 mmol), the solution was stirred for one hour at 35 °C. Subsequently, TEOS (40.2 mL, 181.4 mmol) was added and the solution was stirred for 22 h at 35 °C. The turbid solution was transferred to a glass bottle with a screw cap and heated in the oven for 24 h at 90 °C. The suspension was filtered off and the solid washed with water (2 x 50 mL) and ethanol (1 x 50 mL). The white solid was dried overnight at room temperature and then calcined in the oven at 500 °C for 4 h with a ramp of 2 K/min. KIT-6 was obtained as a white solid.

5.2.2. Synthesis of Mesoporous Zirconium Oxide

Zirconyl chloride octahydrate (1.8 g, 5.6 mmol) was dissolved in HPLC water (4.2 mL). KIT-6 (1 g) was activated by heating at 500 °C for 1 h. After cooling down, one third of the zirconium precursor solution was mixed with the activated silica. The solid was dried in an oven for 2 h at 100 °C. This cycle was repeated two more times until there was no precursor solution left. The white solid was then calcined at 600 °C for 5 h with a ramp of 2 K/min. To remove silica, the powder was stirred in sodium hydroxide solution (250 mL, 2 M) for 16 h at rt. The suspension was filtered off and washed with water (2 x 50 mL) and ethanol (50 mL). After drying overnight at 80 °C, a white powder was obtained.

5.2.3. Catalysts Synthesis via Dry Impregnation Method

The catalyst was prepared as follows: Nickel nitrate hexahydrate (87 mg, 0.3 mmol) was dissolved in HPLC water (320 µL). One half of the precursor solution was mixed with the mesoporous zirconia (486 mg) with a spatula. The green powder was dried in the oven for 2 h at 100 °C. This cycle was repeated one more time. The green

powder was then calcined at 500 °C in air for 1 h, with a ramp of 5 K/min. Subsequently, the sample was reduced at 500 °C for 1 h, with a ramp of 10 K/min. Hydrogen concentration was 10 % in nitrogen.

For comparison, a reference catalyst was prepared with Puralox®, a γ -alumina from Sasol. Nickel nitrate hexahydrate (870 mg, 3 mmol) was dissolved in HPLC water (2 mL) and then added dropwise to Puralox® (4750 mg). The mixture was homogenized with a spatula for 15 min. The green powder was then calcined at 500 °C in air for 1 h, with a ramp of 5 K/min. Subsequently, the sample was reduced at 500 °C for 1 h, with a ramp of 10 K/min. Hydrogen concentration was 10 % in nitrogen.

5.2.4. Catalytic Screening

Catalytic testings were conducted at BasCat by Chengyue Guan. The catalysts were pressed and sieved into diameter fractions of 100-200 μm . 133 mg of catalyst was loaded in a quartz tube with an inner diameter of 4 mm and fixed with quartz wool. To extend the catalyst bed silica (400 mg) was added for dilution. The gas composition was He:N₂:CH₄:CO₂ 7:1:1:1 with a total flow of 80 mL/min. The final WHSV was 36,000 L/gh. Gas compositions at the exhaust were analyzed by online gas chromatography (GC) with an Agilent 7890A.

5.2.5. Characterization of Catalysts

Transmission electron microscopy (TEM) was carried out with a FEI Tecnai G² 20 S-TWIN with an equipped r-TEM SUTW Detector for electron dispersive x-ray spectroscopy. 25 μL of sample (stabilized silver particles in water) were placed on a carbon coated copper grid. Then, the grid was dried at rt before put on the sample holder.

Elemental analysis was conducted with ICP-OES with a Varian 715 Emission Spectrometer for nickel quantification. Digestion of ICP-OES samples was done by stirring the sample (10-20 mg) in aqua regia (10 mL) for 16 h. After the solid settled, the supernatant liquid (5 mL) was diluted 1:1 with water (HPLC grade).

Temperature programmed reduction (TPR) was conducted with a Microtrac-BEL BelCat II setup. The sample was fixed with glass wool in a quartz glass setup and then put into the BelCat II setup. For the TPO measurement 220 mg of sample

were used. The gas mixture was 10 % H₂ in N₂ with a total flow of 30 mL/min. The temperature was increased from 50 °C to 900 °C with 10 K/min.

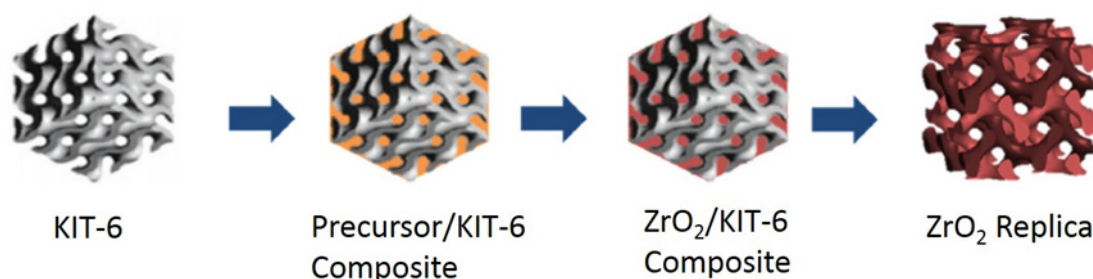
Nitrogen sorption analysis was performed at 77 K using a QUADRASORB SI system, which was equipped with an automated surface area analyzer. Before analysis, sampler were degassed at 120 °C for 12 h. Specific surface areas (BET) were determined over a 0.05-0.30 P/P₀ range.

X-ray powder diffraction (XRD) patterns were recorded on Bruker D8 diffractometer with Cu K α 1 radiation ($\lambda = 0.154$ nm) equipped with scintillation counter.

5.3. Results

Ordered mesoporous silica materials can be used as hard templates to synthesize high surface area mesoporous metal oxides. To stabilize nickel nanoparticles for dry reforming of methane, mesoporous zirconium oxide (mp-ZrO₂) was synthesized and used as a support for nickel. Using the confinement by the pores, a stabilization of nickel nanoparticles and hence, reduced sintering, should be achieved. In addition, zirconium oxide surfaces have high oxygen mobility that is required to prevent coke deposition. Nickel on mesoporous zirconium oxide and, as comparison, on industrial alumina are tested for dry reforming of methane.

To synthesize the catalyst, the first step is to prepare the ordered mesoporous silica, in this case KIT-6. KIT-6 is then impregnated with an aqueous solution of zirconyl chloride, the zirconia precursor. The composite is heated to let the zirconium oxide form followed by the silica template removal by stirring in sodium hydroxide. The nickel is deposited on the mesoporous zirconia by dry impregnation. The synthesis procedure is shown in scheme 5.1.



Scheme 5.1. Scheme for the preparation of hard templated zirconium oxide. KIT-6 is used as the hard template. The zirconia precursor is added in a small excess. The composite is heated to crystallize the zirconia phase. In the last step the silica template is removed in sodium hydroxide. Adopted from [215].

5.3.1. Mesoporous Zirconium Oxide Synthesis and Characterization

The synthesis of KIT-6 is very similar to that of SBA-15. The triblock copolymer Pluronic P123 is used to form micelles under acidic conditions. The diameter of the micelles corresponds to the pore size of the final silica. In contrary to the SBA-15 synthesis, *n*-butanol is added for the KIT-6 synthesis. The *n*-butanol interacts with the micelles of the copolymer and is responsible for the formation of the cubic pore structure.^[190] Tetraethyl orthosilicate (TEOS) is used as the silica precursor. The template was decomposed by calcination and KIT-6 was obtained as a white powder. Zirconyl chloride was dissolved in water and dry impregnated on the synthesized KIT-6. After calcination and template removal, mesoporous zirconia is obtained.

XRD Analysis

The long-range order of KIT-6 and mp-ZrO₂ can be observed by small angle x-ray diffraction (SAXS) (figure 5.1). For KIT-6 the reflexes at 2θ of 1.05 °, 1.20 ° and 1.91 ° can be assigned to the (210), (220) and (420) planes, respectively. After templating, only the (210) plane, which was assigned to the reflex at 1.20 ° can be seen. The shift toward wider diffraction angles indicates shrinkage of the periodic pore distance.^[216] The wide angle x-ray diffraction (figure 5.1) was used to determine the crystal phase of zirconia after calcination at 600 °C. The reflexes can be assigned to the monoclinic and the tetragonal crystal phase of zirconium oxide. A complete transition from monoclinic to tetragonal occurs at higher temperatures. However, calcination at higher temperatures would decrease the surface area. Moreover, benefits from pure crystal phases are not reported for zirconia in the DRM reaction.

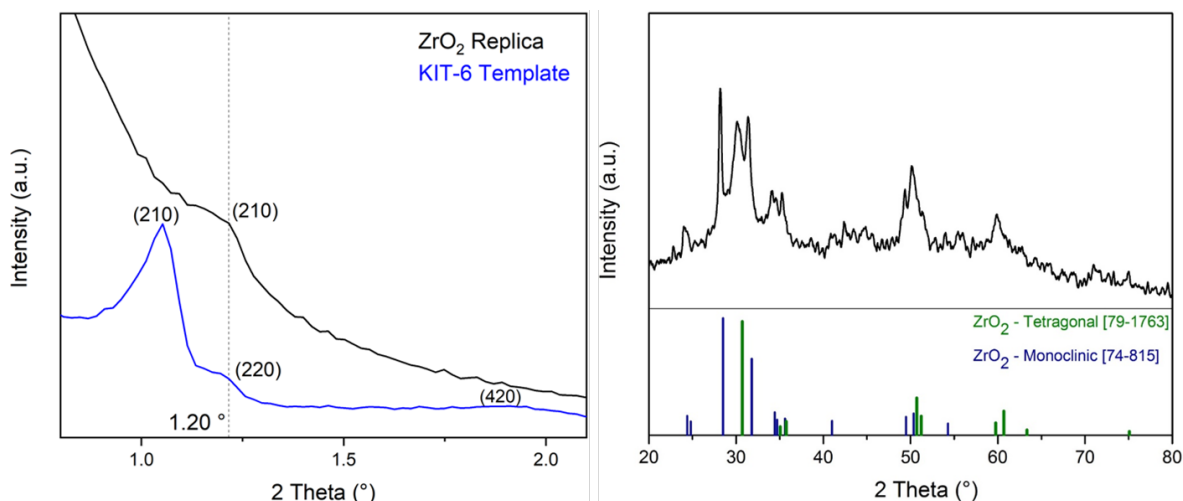


Figure 5.1. SAXS measurements of KIT-6 and zirconia replica (left) and WAXS measurement of the zirconia replica (right). The SAXS shows a long range order regarding the (210) plane for the zirconia replica. The WAXS shows reflexes that can be assigned to tetragonal and monoclinic zirconium oxide.

BET Analysis

To examine the pore structure and surface area, nitrogen physisorption was carried out to compare the mesoporous zirconia and the γ -alumina (figure 5.2). The alumina showed a type IV isotherm which is typical for mesopores.^[217] The hysteresis is originating from capillary condensation in the pores that changes the desorption behavior of nitrogen. Although the templated zirconia isotherm also shows a hysteresis and thus, the presence of mesopores is confirmed, the pore structure changed after the replica synthesis. Some mesopores disappear at the expense of macropores, which indicates that an excess of the precursor was used. Nevertheless, the BET surface area of 244 m²/g is the highest for hard templated and crystalline zirconia in literature based on our knowledge.^[201]

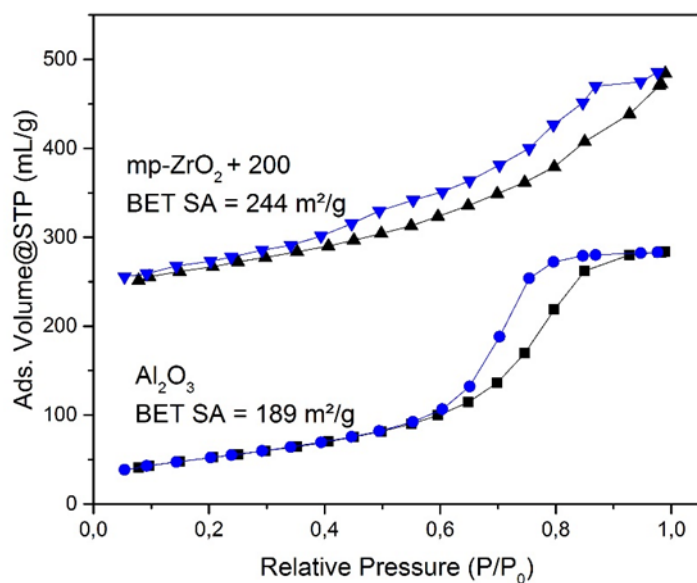


Figure 5.2. Nitrogen physisorption results for mesoporous zirconia (with +200 offset) and Al₂O₃ after synthesis. Both samples are type IV isotherms, typical for mesoporous materials, the zirconia support shows a higher BET surface area compared to alumina (244 m²/g to 189 m²/g).

TEM Analysis

To check the local pore structure of KIT-6 and hard-templated zirconia, TEM was conducted (figure 5.3). KIT-6 images show cubic pore structure. In addition, the long range order can be observed, confirming the XRD results. For zirconia the images look similar regarding the long-range order and the pore size. However, few zirconia particles without pores could be found, which is in line with the results acquired from the nitrogen physisorption isotherm.

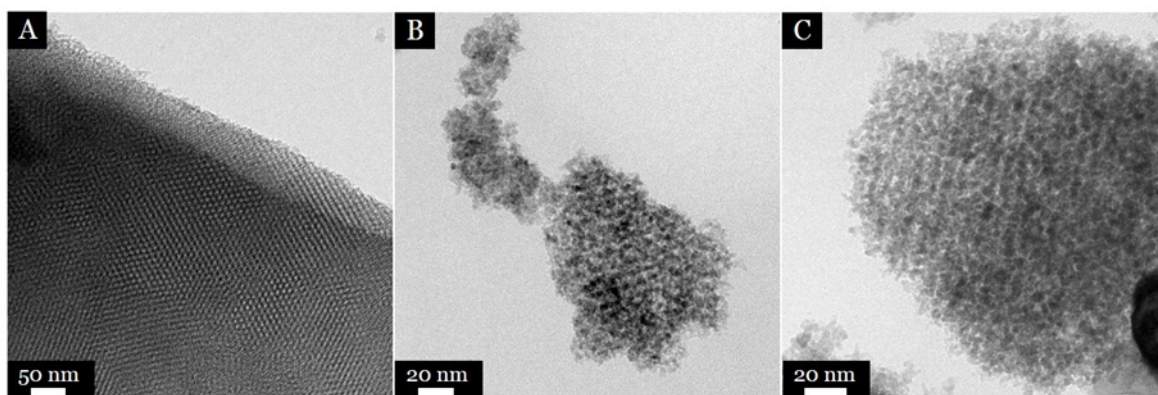


Figure 5.3. TEM measurements of KIT-6 (A) and zirconia replica (B, C). Both samples show ordered mesoporous pore structure.

5.3.2. Synthesis and Characterization of Supported Samples

The next step was to add nickel to the supports. Nickel nitrate hexahydrate was used as the precursor with a target loading of 3 wt% nickel on the final catalysts. The nickel precursor was dissolved in water and deposited on the support via dry impregnation. After impregnation, the samples were calcined at 500 °C in synair atmosphere and then reduced at 500 °C. These temperatures are sufficient to decompose the nitrate counter-anion and then to reduce nickel oxide to catalytically active metallic nickel.

XRD Analysis

The prepared catalysts were examined by XRD to check the final material composition (figure 5.4). Most reflexes can be assigned to the respective supports. For both, the zirconia and alumina sample, reflexes at 44.5 ° and 51.9 ° can be assigned to metallic nickel. The reflexes are very broad and thus, indicate nickel particles with small diameters on both supports.

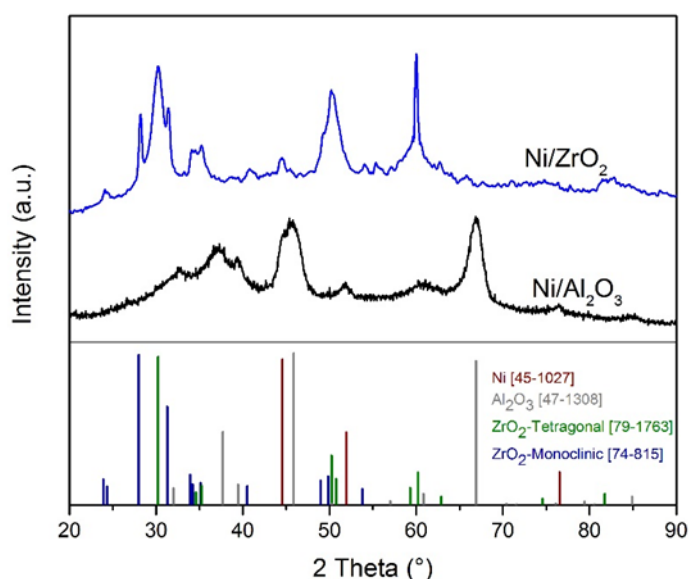


Figure 5.4. XRD measurements of Ni/ZrO₂ and Ni/Al₂O₃ after calcination and subsequent reduction. Reflexes, which can be assigned to nickel are very broad. This indicates small particle sizes. Other reflexes can be assigned to the support phases.

Reduction Procedure

The reducibility of the calcined catalyst gives a further indication of particle size and dispersion of nickel on the support.^[218] In general, stronger stabilization by the support results in higher reduction temperatures. Therefore TPR measurements were conducted for both samples after calcination at 500 °C (figure 5.5). For each sample two peaks were observed. Reduction peaks for the alumina supported sample were measured at 300 °C and 420 °C. In contrast, the reduction peaks for the zirconia sample were measured at 360 °C and 610 °C. The temperature difference can occur due to various surroundings of the nickel oxide particle. If at the edge of the support, nickel oxide particles are more readily reduced when compared to particles within the pores. The pore channels of zirconia stabilize the nickel particles exceptionally well, which results in a high reduction temperature of 610 °C. Because of the set pore diameters, nickel oxide particles only grow to the diameter of the pore during the calcination. This surrounding stabilizes the nickel oxide particles more than in an unordered alumina support. A reduction of zirconia occurs at much higher temperature and is therefore excluded.^[219]

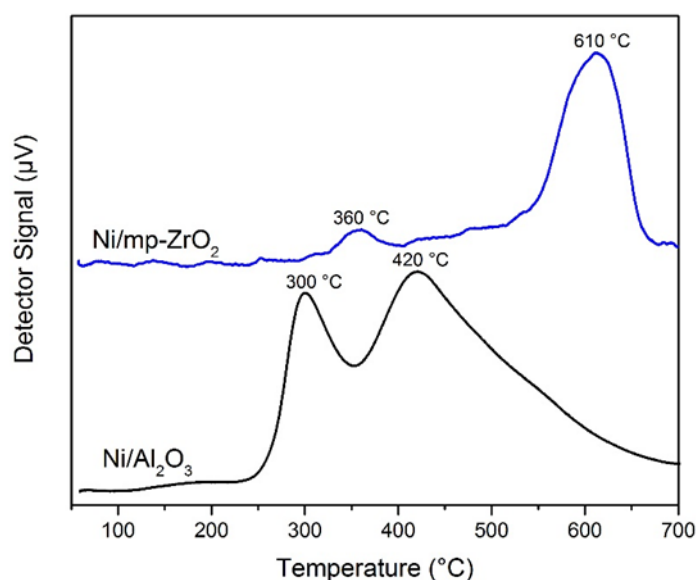


Figure 5.5. TPR of Ni/ZrO₂ and Ni/Al₂O₃ supported samples after calcination at 500 °C. The reduction peaks for the zirconia supported sample are shifted towards higher temperatures due to stronger support interaction between nickel and zirconia.

TEM Analysis

To examine the nickel particle size on a local level, TEM for both samples were carried out (figure 5.6). For both samples, it is very difficult to distinguish between thicker support sites and nickel nanoparticles. This indicates that nickel is very finely dispersed over the supports and no bigger particles are present in the examined areas. EDX measurements confirm the presence of nickel on the support in the observed support particles. Changing to STEM mode could not increase the visibility of nickel particles as the difference in contrast between nickel and zirconia/alumina is not sufficient.

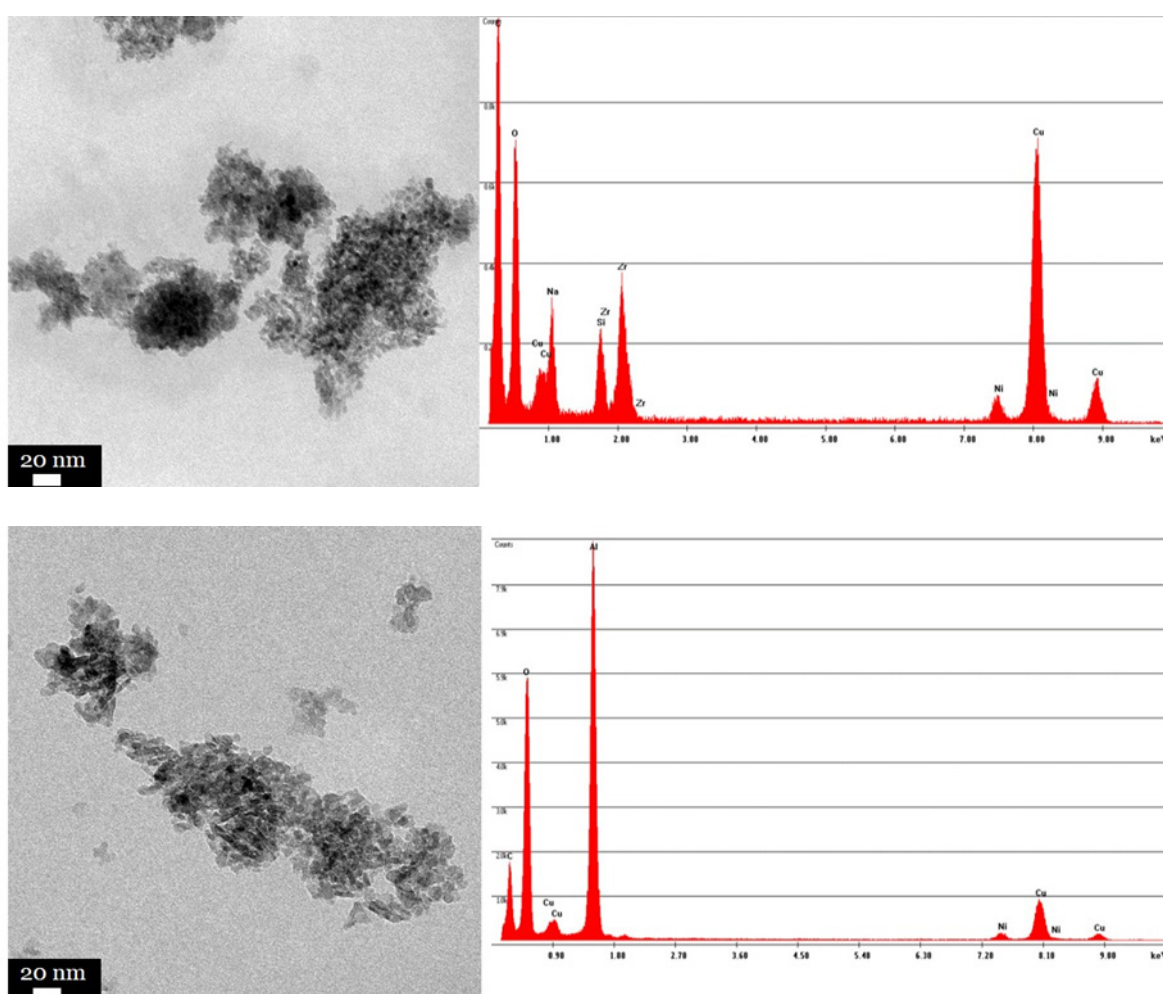


Figure 5.6. TEM and EDX measurements of Ni/ZrO₂ (top) and Ni/Al₂O₃ (bottom) supported samples after calcination and subsequent reduction. Both samples show well distributed nickel particles over the support. The nickel presence was confirmed by EDX measurements. EDX measurements were carried out over the whole image range.

BET and ICP Analysis

After addition of metal particles to the support, the BET surface area can decrease, because nickel particles block pore channels. The nitrogen physisorption isotherms for Ni/Al₂O₃ and Ni/ZrO₂ is shown in figure 5.7. The BET surface area decreases from 189 to 182 m²/g for the alumina support. For zirconia the BET surface area decreases from 244 to 154 m²/g. The curve and hysteresis do not change after addition of nickel on the alumina support. However, the strong decrease in surface area and reduction of the hysteresis for the zirconia supported sample indicates partial pore blocking by nickel particles.

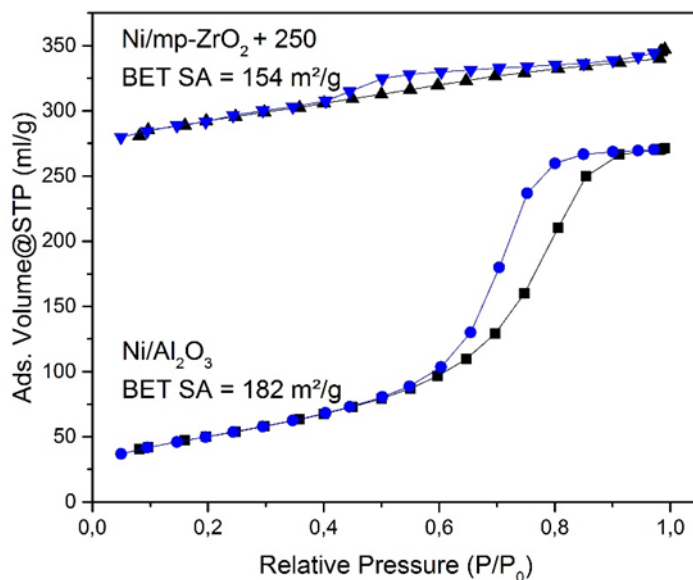


Figure 5.7. Nitrogen physisorption results for nickel supported on zirconia (with +250 offset) and Al₂O₃ after calcination and reduction. Both samples are type IV isotherms, typical for mesoporous materials. The zirconia support shows a lower BET surface area compared to alumina (154 m²/g to 182 m²/g).

To quantify the nickel amount for each catalyst, elemental analysis by ICP-OES was performed. For this, a certain amount of the catalyst was stirred in aqua regia overnight. The suspension was centrifuged and half of the supernatant liquid was used for analysis. The found nickel amounts are very similar with 2.2 wt% for Ni/ZrO₂ and 2 wt% for Ni/Al₂O₃. Properties of both catalysts are summarized in table 5.1.

Table 5.1. BET Surface area and nickel loading for Ni/ZrO₂ and Ni/Al₂O₃ after reduction at 500 °C. Nickel loading is slightly higher for the zirconia supported sample, while the surface area is higher for the alumina supported sample.

Sample	Ni loading [wt%]	BET Surface Area [m ² /g]
Ni/ZrO ₂ (BC1380)	2.2	154
Ni/Al ₂ O ₃ (BC1230)	2	182

5.3.3. DRM Performance Test

The catalytic performance of synthesized catalysts for dry reforming of methane was measured by Chengyue Guan. The temperature was gradually increased in 100 °C intervals from 500 °C to 800 °C at 1 bar. Each temperature was held for 5 h and each hour one measuring point was recorded. After 20 h time on stream the temperature was decreased to 700 °C for a long time measurement for 60 h. The WHSV was set to 36,000 h⁻¹ and then increased for the long-term measurement. The results are shown in figure 5.8.

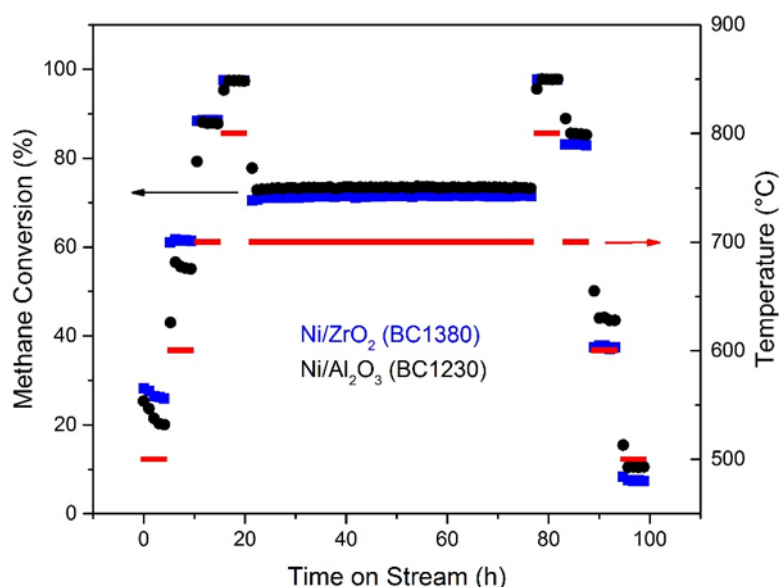


Figure 5.8. Methane conversion for Ni/ZrO₂ and Ni/Al₂O₃ at different temperatures and WHSVs. During ramp-up the zirconia supported sample shows a higher activity in comparison to the alumina support. After increasing the temperature to 800 °C, the alumina supported sample shows higher methane conversions.

Table 5.2. Performance data at 700 °C during ramp-up, long term measurement with increased WHSV and ramp-down for Ni/ZrO₂ and Ni/Al₂O₃. Ni/ZrO₂ shows the higher initial activity but is less stable compared to Ni/Al₂O₃. Both samples show very high stability under these conditions.

Sample	X_{CH₄} Ramp-up @ 700 °C [%]	X_{CH₄} after 50 h TOS [%] with in- creased WHSV	X_{CH₄} Ramp-down @ 700 °C [%]
Ni/ZrO ₂ (BC1380)	88.5	71.5	83.1
Ni/Al ₂ O ₃ (BC1230)	87.9	73.3	85.4

At intermediate temperatures until 700 °C, Ni/ZrO₂ showed a higher conversion of methane compared to Ni/Al₂O₃. At 800 °C methane conversion of Ni/Al₂O₃ was slightly higher. For the ensuing long time measurement at 700 °C both catalysts were very stable and showed almost no deactivation. The methane conversion of Ni/Al₂O₃ was slightly higher compared to Ni/ZrO₂. The decreasing performance for the zirconia supported catalyst at high temperatures could be due to collapsing mesopores. This would lead to a worse accessibility of the active nickel sites and an overall decrease in surface area and nickel dispersion. Especially when comparing the performance of Ni/ZrO₂ at 600 and 700 °C between heating up and heating down after the long time measurement a decrease in methane conversion is apparent. For example, while 61 % methane conversion was measured during ramp-up at 600°C, the methane conversion decreased to 37 % during ramp-down at 600 °C. The alumina supported sample showed less deactivation when comparing ramp-up and ramp-down methane conversion, e.g. from 55 % to 43 % at 600 °C. Important values are summarized in table 5.2.

5.3.4. Characterization of Spent Catalysts**BET Analysis**

To examine if the deactivation of the zirconia supported sample is associated with mesopore collapse, nitrogen physisorption was conducted. The BET surface area for the zirconia supported sample decreased from 154 to 76 m²/g during the catalytic reaction while the alumina supported BET surface area only decreased from 182 to 146 m²/g (figure 5.9). This shows that the alumina support is more stable under the harsh DRM conditions. Despite that, the zirconia support still shows a high surface area for a hard templated mesoporous metal oxide with an ordered pore structure. The performance data indicates that the partial pore collapse occurred at 800 °C. Furthermore, if the catalytic performance is calculated per surface area the zirconia supported sample is more active in comparison to the alumina supported sample (Table 5.3). This indicates a promoter effect by the zirconia support. Either by the before mentioned oxygen mobility or by the structural pathway due to the pore channels. However, also the higher nickel loading of the zirconia supported sample needs to be taken into account (2.2 wt% for Ni/ZrO₂ in comparison to 2 wt% for Ni/Al₂O₃).

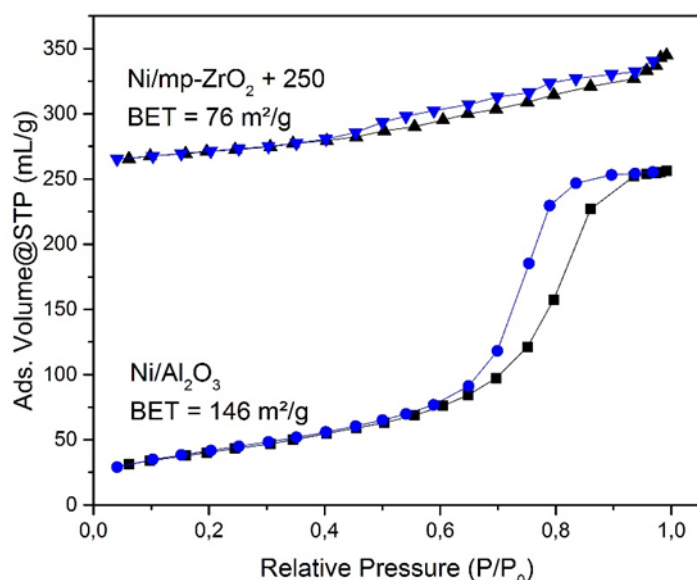


Figure 5.9. Nitrogen physisorption results for nickel supported on zirconia (with +250 offset) and Al₂O₃ after 100 h time on stream. The BET surface area of Ni/ZrO₂ decreased by about 50 % during the reaction (154 m²/g to 76 m²/g), while the surface area Ni/Al₂O₃ just decreased by 36 m²/g.

Table 5.3. BET surface area and correlating methane conversion and methane consumption per m² and nickel loading of Ni/ZrO₂ and Ni/Al₂O₃. If methane consumption is calculated per spent catalysts surface area and nickel loading, Ni/ZrO₂ shows the better performance in comparison to Ni/Al₂O₃.

Sample	BET Surface Area after Catalysis [m²/g]	X_{Methane} Ramp- down @ 700 °C [%]	Methane Consumption [mmol/mmol(Ni)*s*m²]
Ni/ZrO ₂ (BC1380)	76	83.1	9.82
Ni/Al ₂ O ₃ (BC1230)	146	85.4	5.74

XRD Analysis

By XRD analysis information about crystal phase changes of zirconia and alumina supported nickel samples were obtained (figure 5.10). The sharp reflex at 27 ° can be assigned to quartz, the used inert material for the reaction. Reflexes of both zirconia phases, monoclinic and tetragonal, are still present and have not changed during reaction. Small, broad reflex or shoulders at 44.5 ° and 51.9 ° can be assigned to metallic nickel for both samples. This indicates that a sintering during the reaction was mitigated as the broadness of the reflexes is similar to the sample before catalysis. Consequently, particle sintering is not the source of deactivation, but rather the decrease in surface area.

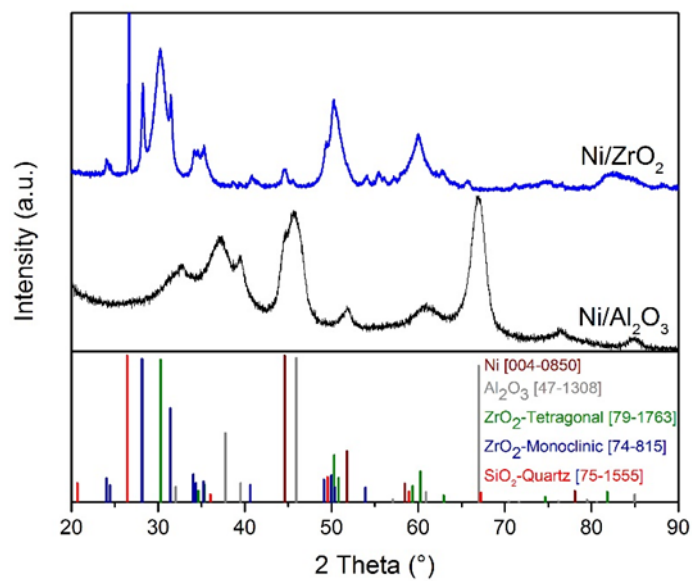


Figure 5.10. XRD of spent Ni/ZrO₂ and Ni/Al₂O₃ sample. Both diffractograms look very similar to those before the reaction which means that no phase change occurred during reaction and nickel particle sintering was mitigated due to support stabilization.

5.4. Conclusion

Ordered mesoporous zirconium oxide was synthesized with the nanocasting method with KIT-6 as the template. The final BET surface area of 244 m²/g is the highest for a hard templated, crystalline zirconia to our knowledge.

The material was used as a support for nickel-based catalysts in the DRM reaction due to its promoter properties. After nickel deposition, XRD, TEM and BET measurements indicate very good nickel dispersion over the support.

The catalytic performance was compared with an aluminum supported nickel catalysts with similar metal loading. Until 700 °C, the mesoporous zirconia support outperformed the reference catalyst. At 800 °C, the reverse case was observed. During the ensuing long-term test at 700 °C, both samples showed remarkable stability regarding methane conversion. Also, these catalysts showed a higher activity and stability compared to those in chapter 4, although the stabilization of the nickel particles was carried out only by high surface area supports. The lowered performance values during the ramp-down indicated a partial pore collapse for the mesoporous zirconia support. By nitrogen physisorption, a decrease from 154 m²/g to 74 m²/g during the reaction was observed.

The results in this thesis showed, that zirconia is a stable catalyst support up to 700 °C. At higher temperatures than 700 °C the pores start to collapse. Therefore this support is only suitable up to 700 °C for the DRM reaction. Due to the high surface support and stability, this support would also be suitable for other processes.

6. Summary and Outlook

In this thesis, colloidal methods were used to synthesize novel catalysts for ethylene epoxidation and dry reforming of methane. The advantages of colloidal methods were exploited to synthesize well-defined catalysts. The synthesis for all colloid-based catalyst followed the same procedure: First, the colloids were synthesized. The stabilized nanoparticles were then supported via wet impregnation. In the last step the stabilizer was removed and the material pretreated for the catalytic reaction.

With colloidal methods, model catalysts were synthesized to examine the particle size effect and the role of sulfur during the ethylene epoxidation process. For a particle size study, the synthesis of silver nanoparticles with narrow particle size distributions and the exclusion of particles smaller than 10 nm was successful. With conventional synthesis methods (e.g. impregnation methods), such a particle size distribution and an exclusion of very small nanoparticles would not be possible. Three supported samples with differently sized silver nanoparticles (40, 60 and 100 nm on average) were prepared. Among the prepared samples, smaller silver particles (40 nm) showed the highest selectivity for ethene epoxidation if no promoter is added. When ethylene chloride was added to the feed, the selectivities for all samples were levelled out.

It was suggested that bigger particles benefit more after promoter addition. Bigger particles can take higher amounts of bulk oxygen which can diffuse to the surface and facilitate total oxidation. When ethylene chloride is used as a promoter in the gas stream, the electronic properties on the surface change which leads to higher selectivity towards ethylene oxide.

To examine the sulfur promoter effect during the ethylene epoxidation reaction, supported silver-silver sulfide core-shell particles were tested along with a sulfate promoted Ag/Al₂O₃ sample. The catalytic screening showed a better performance by the sulfate promoted catalyst, whereas the sulfide samples were almost inactive. The results proved, that adding a high valent promoter like sulfate is beneficial for the catalyst's performance. Furthermore, there is no conversion of sulfides to sulfates during catalysis. XPS measurements of the spent samples showed that the sulfate is positioned at the support and not on silver particles. However, catalytical processes are very dynamic and thus, the position of the sulfate can also change during the reaction.

A disadvantage of colloid-based catalysts is the limited loading capacity. For both projects the catalysts had a much lower silver loading in comparison to the industrial silver catalyst (about 2 % vs. 15 %). As a result, the performance could not be compared to the industrial catalyst at the same conditions. In general, it is difficult to imagine that colloid-based catalysts could perform better than conventional catalysts in processes where catalysts with high metal loading are used. For supported precious metal catalysts, where metal loadings seldomly exceed 2 wt%, the colloid-based approach could be interesting due to size and shape control of the final nanoparticles. Here, the challenge is to remove the stabilizer without sintering of the particles. In this thesis, several approaches like different kind of heat treatments and ozone treatment were employed. For the highly mobile silver particles on a low surface area support, the short heat treatment was the best solution to remove tannic acid and mitigate sintering.

For uses in industrial processes the scalability of nanoparticle synthesis becomes an issue. Nucleation and growth processes are very sensitive to concentration gradients in the reaction vessel. Therefore, homogeneous addition of the reactants and fast and uniform mixing is crucial for upscaling. In this thesis, even a small upscale on a lab scale required adjustments regarding the pH value and the stirring speed.

For the ethylene oxide process, further research is necessary to increase loading with intermediate sized particles (40-60 nm) on α -alumina. As the results from the particle size study in chapter 2 showed, with this particle size a high selectivity can be achieved even without ethylene chloride. If the conversion can be increased by increasing the silver loading without decreasing selectivity, the use of ethylene chloride could be expendable. This could save the use of expensive non-corrosive tubing and would thus facilitate the process in general.

In search for a stable DRM catalyst, nickel phosphide manganese oxide core-shell particles and nickel phosphide nanoparticles were synthesized by colloidal methods, supported on γ -alumina and tested for dry reforming of methane. Both catalysts showed high activity and very good stability over 60 h time on stream. During reaction the nickel phosphides converted to metallic nickel as confirmed by XRD measurements. By TG-MS measurements of the spent catalysts, the sample with manganese showed 35 % less coke deposition in comparison to the pure nickel phosphide

sample. This had no impact during the measured run, but could increase the stability for longer time on stream as coke deposition is a major source of deactivation. In contrast, the addition of phosphorus stabilizers to the synthesis could be the reason for the good long-term stability during the run as the characterization of both catalysts showed. XPS measurements confirmed a phosphate species on the support, while STEM and TEM images revealed small particles on the support in close proximity to the phosphorus. In contrast, bigger particles were detached from the support.

In the last chapter a support variation for the dry reforming of methane was examined. Ordered mesoporous zirconium oxide was synthesized with the nanocasting method, whereby KIT-6 was used as the template. The final BET surface area of 244 m²/g was the highest for a hard templated crystalline zirconia in literature. Metallic nickel was deposited via dry impregnation on zirconia and alumina. Until 700 °C, the mesoporous zirconia support outperformed the alumina supported catalyst. At higher temperatures the surface area, and consequently the performance, decreased. Nevertheless, the methane consumption per surface area and nickel loading was higher compared to the alumina supported sample indicating a promoter effect by the zirconia support.

Both catalysts from chapter 5 outperformed the manganese/phosphorus promoted catalysts from chapter 4. This means, that the stabilization of nickel by high surface area supports is sufficient to give a stable catalyst for DRM. However, as described above, the zirconia support can outperform the conventional alumina support when the reaction conditions are adjusted to the material.

It is difficult to compare these with other literature findings, because no standardized procedure for measuring dry reforming of methane is established yet. This could change, if a technical plant for DRM is put into operation and research groups would use these reaction conditions for comparability. For our test a more simple approach (dry impregnation) lead to the best catalysts. Still, the nickel phosphide-manganese oxide core-shell catalysts from chapter 4 could outperform nickel/manganese catalysts from literature.

With colloidal synthesis methods desired structures can be synthesized precisely. This can have a severe impact on the final properties of the material. In the future,

more materials with unique properties will be synthesized, which could help for an advancement in catalysis research. As described in the introduction, for this a deeper understanding for catalytic processes is necessary. For a general outlook a stronger interaction between academic and industrial research is recommended. The introduced approach to synthesize model catalysts, which can be assigned to an academic approach, and test these materials at industrially relevant conditions can yield valuable information towards deeper understanding of catalytic processes. Although at first, these catalysts will not have a direct industrially relevant success, the gathered information can help to “design” better performing catalysts in the future. To maximize the gained information about the structure-reactivity relationship of model catalysts, in-situ analytics have to be used to monitor electronic and structural changes during the reaction.

Abbreviations

ALD	Atomic layer deposition
BET	Brunauer-Emmett-Teller
DFT	Density functional theory
DRM	Dry reforming of methane
EC	Ethylene chloride
EDX	Energy dispersive X-ray spectroscopy
EO	Ethylene oxide
GC	Gas chromatography
GHSV	Gas hourly space velocity
HPLC	High performance liquid chromatography
ICP-OES	Inductively coupled plasma optical emission spectroscopy
IR	Infrared
KIT-6	Korean Institute of Technology 6
MCM-41	Mobil composition of matter 41
MIM	Multiple injection method
MS	Mass spectrometry
OMC	Oxometalloycycle
PSD	Particle size distribution
RT	Room temperature
SAXS	Small angle x-ray scattering
SBA-15	Santa Barbara amorphous
SEM	Scanning electron microscopy
SIM	Single injection method
STEM	Scanning transmission electron microscopy
TEM	Transmission electron microscopy
TG	Thermal gravimetry
TOF	Turnover frequency
TOP/TOPO	Triocetyl phosphine (oxide)
TPO/TPR	Temperature programmed oxidation/reduction
UV-VIS	Ultraviolet-visible
WAXS	Wide angle x-ray scattering
WHSV	Weight hourly space velocity
XPS	X-ray photoelectron spectroscopy
XRD	X-ray diffraction

List of Figures

Nr.	Figure description	Page
1.1	Thermodynamic reaction progress of educt A to product Z with and without a catalyst. With catalyst addition the activation energy for the reaction is decreased. Adopted from [3].	1
1.2	A precursor solution is mixed with the support. The volume is the same as the pore volume of the support. After Calcination particles with a broad range of particle sizes, depending on the position in/on the pore, form.	2
1.3	Performance data of industrial processes based on patents. Left: Selectivity to ethylene oxide in the selective oxidation of ethylene. The selectivity is strongly dependant on the conversion and process conditions. The performance increase in earlier years is due to improvement of the added promoter package. ^[29–33] Right: Yield of maleic anhydride in the selective oxidation of <i>n</i> -butane. The strong yield improvement from 1966 to 1985 was due to optimization of the synthesis pretreatment procedure. ^[34–38]	6
1.4	Model of particle formation mechanism as postulated by LaMer. In the first phase the precursor is reduced to metallic atoms. If a critical atom concentration is reached the fast nucleation event occurs. Remaining or new formed atoms nucleate at the surface of existing particles until saturation is reached. Adopted from [55].	8
2.1	Examples for Particle size studies in the literature. A: The influence of different cobalt particles size regarding the activity for the Fischer-Tropsch process. The highest activity is observed at 6 nm. B: Turnover frequencies for different sized gold nanoparticles on ceria for the carbon monoxide oxidation. The highest TOF is observed at around 3 nm. C: Selectivity influence for different sized platinum colloids in the pyrrole hydrogenation. Smaller particles give higher amounts of pyrrolidone and lower amounts of <i>n</i> -butylamine compared to bigger particles. Adopted from [99–101].	16
2.2	UV-VIS measurements of the tannic acid stabilized silver colloids at different reaction pH values. The sample synthesized at higher pH value absorbs at higher wave lengths (left). The Sigma Aldrich reference diagram shows assignation of absorption maxima to particle size. Based on the reference, the pH 6.8 sample is around 30 nm and the pH 5.9 sample around 60 nm in size. The strong increase in absorbance in the UV region could originate from the tannic acid stabilizer. Right graph adopted from sigmaaldrich.com/technical-document/articles/materials-science/nanomaterial/silver-nanoparticles.html .	24
2.3	TEM images of the tannic acid stabilized silver colloids at different reaction pH values (A,B) and their particle size distribution (C). The images show a homogeneous particle size distribution. The TEM measurement is in accordance with the UV-VIS results.	25
2.4	Images of the stepwise multiple injection synthesis. After each injection a color change can be observed. With each injection silver nitrate and tannic acid are added. Color changed from yellow to brown.	26
2.5	TEM images of stabilized silver colloids synthesized by multiple injection method. The images show a narrow particle size distribution with an average diameter of 78 nm.	26
2.6	TEM images of stabilized silver colloids synthesized by citrate added multiple injection method. The images show a narrow particle size distribution but also some irregular shaped particles.	27

2.7	TEM and UV-VIS analysis for upscaled silver colloid synthesis. Smaller particles show a more narrow particle size distribution in comparison to bigger particles.	28
2.8	Tannic acid structure with two layers of gallic acid units and a glucose core ring. Gallic acid units can also decompose as pyrogallol and carbon dioxide. Adopted from [118].	30
2.9	TPO-MS measurement of stabilized silver nanoparticles on alumina support. The temperature was increased by 2 K/min. The MS signal $m/z=44$ is shown, as carbon dioxide is main de-composition product. The MS signal $m/z=52$ is a pyrogallol fragment.	31
2.10	IR measurements after impregnation step and after four different calcination procedures (see table 2.2 for more information). The measurement was conducted from 4000-400 cm^{-1} , but the relevant bands are in the represented range from 2000-800 cm^{-1} . Spectra were plotted with following offsets: Impregnated: -10 % ; 270 °C: -7 % ; 285 °C: +3 % ; 300 °C: +5 % ; 330 °C: +5 %.	32
2.11	SEM images after the impregnation step (A) and after calcination procedure D (B). The particles grow during calcination from 23 to 41 nm on average and the PSD broadens.	33
2.12	Left: Ozone decomposition as measured by MS The MS signal $m/z=44$ is shown, as carbon dioxide is the main decomposition product. The decomposition starts between 100 °C and 200 °C with ozone treatment. Right: IR measurements after impregnation and after ozone treatment. Shifting of vibrational stretching bands at 1194 cm^{-1} (-C-O-) and 1446 cm^{-1} (aromatic -C=C-) is observed, which indicates a partial decomposition of the tannic acid stabilizer.	35
2.13	IR measurements after impregnation and after four different heat treatment times. The measurement was conducted from 4000-400 cm^{-1} , but the relevant bands are in the represented range from 2000-800 cm^{-1} . After 30 s the bands of the impregnated samples disappeared indicating tannic acid decomposition. Spectra were plotted with following offsets: 0 s: -8 % ; 15 s: -6 % ; 30 s: -4 % ; 45 s: -2 %.	37
2.14	SEM images after impregnation and after 60 s short heat treatment. The particles grow during calcination from 23 to 37 nm on average and the PSD broadens. Still, this result for the stabilizer removal is better compared to the conventional calcination procedure.	37
2.15	SEM images of the three catalysts after the stabilizer removal. The particle size distribution broadened for all samples. Still, the overlap of the samples PSDs is small.	38
2.16	Screening program with temperature and ethylene chloride concentration over time on stream. Full test program is given in the experimental part. Due to low conversions, the maximum temperature was increased from 245 °C to 260 °C.	40
2.17	Selectivity towards ethylene oxide in dependence of particle size and EC concentration. The graphs are linear fits with data from table 2.6. With EC dosing, the particle size regarding the selectivity is offset.	42
2.18	SEM images of spent catalysts after 300 h time on stream. Left: BC991 (40 nm); middle: BC990 (60 nm); right: BC992 (100 nm). For the 100 nm sample the most pronounced growth is observed (+ 33 % in average particle size). The 40 and 60 nm samples have an increased average particle size of about 14 %.	44
2.19	XPS measurement of spent catalysts after 300 h time on stream. A tendency towards surface silver oxide is observed for samples 40, 60 and 100 nm, while the 20 nm sample (prepared by laser ablation) can rather be assigned to metallic silver.	45

2.20	UV-VIS measurements of the tannic acid stabilized silver colloids at different reaction pH values with ammonium hydroxide as the pH setting reagent. The sample synthesized at higher pH value absorbs at higher wave length.	47
2.21	TEM images of the tannic acid stabilized silver colloids at different reaction pH values (A, B, C) and their particle size distribution (D). Smaller particles show a more narrow particle size distribution in comparison to bigger particles.	48
3.1	TEM overview image of silver/silver sulfide composite (A) and magnification (B, C, D) of image A. Silver shows a stronger contrast (darker compared to the background) than silver sulfide. Colloids formed as desired core-shell particles (A), but also as Janus particles (B). Furthermore, also silver sulfide only particles formed (D).	58
3.2	TEM image of silver/silver sulfide core-shell particles (A, B) and EDX measurements confirming the presence of sulfur (C). No silver sulfide particles were observed.	59
3.3	TEM, STEM images and mapping of silver/silver sulfide core-shell particles. Sulfur (green) signals were observed around silver (red). Yellow color indicates overlap of silver and sulfur.	60
3.4	Screening program with temperature and ethylene chloride concentration over time on stream. Full test program is given in the experimental part. Due to low conversions in the first run (chapter 2), the maximum temperature was increased from 260 °C to 275 °C.	62
3.5	XPS measurement of spent catalysts after 300 h time on stream. After fitting, the S2p _{3/2} peak is measured at 169.1 eV for the spent BC1575 sample, which indicates that after reaction the sulfur is located on the alumina support.	64
A3.1	Additional TEM, STEM images and mapping of silver/silver sulfide core-shell particles. Sulfur (green) signals were observed around silver (red). Yellow color indicates over-lap of silver and sulfur	66
4.1	Comparison of measured diffractograms at different temperatures. At 220 °C all three reflexes can be assigned to the nickel phase. At 290 °C a complete conversion to nickel phosphide takes place.	75
4.2	XRD diffractogram for colloidal particles after reaction (at 290 °C), work-up and isolation. All major reflexes can be assigned to the nickel phosphide phase.	76
4.3	TEM and EDX analysis for colloidal particles after reaction (at 290 °C), work-up and isolation. A shell with higher brightness around the nickel phosphide particles can be observed. EDX measurements show a significant manganese signal.	77
4.4	TEM and EDX analysis for colloidal particles after reaction without manganese addition (at 290 °C), work-up and isolation. No shell is observable around the nickel phosphide particles and also the EDX results show no manganese signal.	78
4.5	<i>Left:</i> TGA of freshly impregnated sample in synair (20 % O ₂ in N ₂). The oxidative atmosphere leads to decomposition of the stabilizers from rt to 500 °C. <i>Right:</i> TPR of the supported samples after calcination at 800 °C. Two distinct reduction events were observed. First, the reduction of nickel oxide to metallic nickel. Second, the reduction of nickel phosphate to nickel phosphide over several stages of nickel phosphides.	80
4.6	XRD of supported sample after calcination at 800 °C and subsequent reduction at 850 °C. After calcination the reflexes can be assigned to the alumina support, no nickel phosphide reflexes are observable due to a good distribution over the support. Reflexes of the reduced samples can be assigned to the support, nickel and nickel phosphides.	81

4.7	XPS measurements of supported sample after calcination at 800 °C and subsequent reduction at 850 °C. Left: Region for the phosphorus 2p signal. The calcined sample only shows a signal at 134.1 eV which can be assigned to P(V). This could be a well distributed phosphate species, either nickel or aluminum phosphate. The reduced sample shows an additional signal at 129.6 eV which can be assigned to P(-III), the phosphide species. This is in accordance with the XRD measurement. Right: Region for the nickel 2p signal. The signals for the calcined sample are shifted towards higher binding energy and thus, higher oxidation states in comparison to the reduced sample.	82
4.8	TEM, STEM and STEM mapping for the calcined and reduced samples. <i>Top</i> : For the calcined sample only few bigger particles are observable (A). The reduced sample shows a very heterogeneous particle size distribution. While many particles are well stabilized by the support (B), also bigger agglomerates at the support edges form (C). <i>Middle</i> : Mapping of calcined sample shows a very good distribution of nickel (blue) and manganese (yellow). Manganese concentration is higher near nickel. <i>Bottom</i> : Manganese (red) is still well distributed over the support and near nickel (blue) while nickel tends to form bigger particles after reduction.	84
4.9	TEM images of the reference nickel phosphide sample without manganese after reduction. The sample shows a heterogeneous particle size distribution. While many particles are well stabilized by the support, also bigger agglomerates are observable. At some positions it is difficult to distinguish between thicker support and particles. However, even at the lighter position (red circle) EDX analysis confirms nickel presence.	85
4.10	Nitrogen physisorption results for NiP@MnO/Al ₂ O ₃ (with +100 offset) and NiP/Al ₂ O ₃ after reduction at 850 °C. Both samples are type IV isotherms, typical for mesoporous materials.	86
4.11	Thermodynamic equilibrium with maximum methane and carbon dioxide conversion at 1 bar for different temperatures as calculated by Dr. Benjamin Frank. A reaction limitation is based on carbon dioxide conversion.	87
4.12	Methane and carbon dioxide in comparison for NiP@MnO/Al ₂ O ₃ (left) and NiP/Al ₂ O ₃ (right). Carbon dioxide is always converted at a higher percentage due to the Boudouard equilibrium and the reverse water-gas shift reaction. The WHSV is gradually increased at 800 °C, which leads to decreasing conversions for both catalysts.	88
4.13	Methane conversion and methane consumption in comparison for NiP@MnO/Al ₂ O ₃ and NiP/Al ₂ O ₃ . If the nickel amount is taken into account, both catalysts show a similar performance.	89
4.14	TG-MS analysis of NiP@MnO/Al ₂ O ₃ (left) and NiP/Al ₂ O ₃ (right) spent samples. M/z = 44 shows the signal of carbon dioxide, which is the main product after coke oxidation.	91
4.15	XRD of spent NiP@MnO/Al ₂ O ₃ sample. After reaction nickel phosphide was converted to metallic nickel due to the reducing atmosphere. The silica reflexes originate from the inert material, which is added to the catalytic bed.	92
4.16	XPS measurements of spent NiP@MnO/Al ₂ O ₃ sample. <i>Left</i> : Region for the phosphorus 2p signal. The signal at 129.6 eV was not detected for the spent signal. This is in accordance with the XRD results, that the phosphide species reacted. The phosphate species is still present. <i>Right</i> : Region for the nickel 2p signal. The signals for the spent sample are shifted towards higher binding energy and thus, higher oxidation states in comparison to the reduced sample.	93
4.17	TEM and STEM measurements of spent NiP@MnO/Al ₂ O ₃ sample. The spent sample shows a very heterogeneous particle size distribution. Some particles are	94

	well stabilized by the support (C), but the majority of particles sintered to bigger agglomerates. Some particles are detached from the support and show a thick carbon shell. Line scan of supported particles shows no phosphorus signal (D-F).	
4.18	Particle size distributions after colloidal synthesis and after calcination, reduction and reaction of the supported nickel phosphide manganese oxide core-shell particles.	95
4.19	TEM and EDX measurements of spent NiP/Al ₂ O ₃ sample. The spent sample shows a very heterogeneous particle size distribution similar to the manganese containing sample with small particles confirmed by EDX measurements but also sintered particles with a carbon shell.	95
5.1	SAXS measurements of KIT-6 and zirconia replica (left) and WAXS measurement of the zirconia replica (right). The SAXS shows a long range order regarding the (210) plane for the zirconia replica. The WAXS shows reflexes that can be assigned to tetragonal and monoclinic zirconium oxide.	105
5.2	Nitrogen physisorption results for mesoporous zirconia (with +200 offset) and Al ₂ O ₃ after synthesis. Both samples are type IV isotherms, typical for mesoporous materials, the zirconia support shows a higher BET surface area compared to alumina (244 m ² /g to 189 m ² /g).	106
5.3	TEM measurements of KIT-6 (A) and zirconia replica (B, C). Both samples show ordered mesoporous pore structure.	106
5.4	XRD measurements of Ni/ZrO ₂ and Ni/Al ₂ O ₃ after calcination and subsequent reduction. Reflexes, which can be assigned to nickel are very broad. This indicates small particle sizes. Other reflexes can be assigned to the support phases.	107
5.5	TPR of Ni/ZrO ₂ and Ni/Al ₂ O ₃ supported samples after calcination at 500 °C. The reduction peaks for the zirconia supported sample are shifted towards higher temperatures due to stronger support interaction between nickel and zirconia.	108
5.6	TEM and EDX measurements of Ni/ZrO ₂ (top) and Ni/Al ₂ O ₃ (bottom) supported samples after calcination and subsequent reduction. Both samples show well distributed nickel particles over the support. The nickel presence was confirmed by EDX measurements. EDX measurements were carried out over the whole image range.	109
5.7	Nitrogen physisorption results for nickel supported on zirconia (with +250 offset) and Al ₂ O ₃ after calcination and reduction. Both samples are type IV isotherms, typical for mesoporous materials. The zirconia support shows a lower BET surface area compared to alumina (154 m ² /g to 182 m ² /g).	110
5.8	Methane conversion for Ni/ZrO ₂ and Ni/Al ₂ O ₃ at different temperatures and WHSVs. During ramp-up the zirconia supported sample shows a higher activity in comparison to the alumina support. After increasing the temperature to 800 °C, the alumina supported sample shows higher methane conversions.	111
5.9	Nitrogen physisorption results for nickel supported on zirconia (with +250 offset) and Al ₂ O ₃ after 100 h time on stream. The BET surface area of Ni/ZrO ₂ decreased by about 50 % during the reaction (154 m ² /g to 76 m ² /g), while the surface area Ni/Al ₂ O ₃ just decreased by 36 m ² /g.	113
5.10	XRD of spent Ni/ZrO ₂ and Ni/Al ₂ O ₃ sample. Both diffractograms look very similar to those before the reaction which means that no phase change occurred during reaction and nickel particle sintering was mitigated due to support stabilization.	115

List of Tables

Nr.	Figure description	Page
2.1	Run protocol for 1 st ethylene epoxidation catalysts screening at hte.	20
2.2	Four different calcination procedures used for tannic acid removal. Heat rate and holding time are similar to industrial synthesis conditions for silver based ethylene oxide catalysts.	32
2.3	Carbon and hydrogen (on average) amount as measured by elemental analysis for different calcination procedures. Average values were taken from three measurements of each sample.	33
2.4	Carbon and hydrogen (on average) amount as measured by elemental analysis for ozone treatment. Average values were taken from two or three measurements of each sample.	35
2.5	Carbon amount as measured by elemental analysis for short heat treatment at 600 °C in a preheated oven. Average values were taken from two measurements of each sample. For all samples, no hydrogen was detected.	36
2.6	Properties of synthesized catalysts and comparison with literature catalysts from Van den Reijen et al. In contrast to these results, any particles smaller than 20 nm in diameter were not detected for the samples in the present work.	39
2.7	Performance data at 260 °C without ethylene chloride and with 0.6 and 1.2 ppm EC dosage. More details about the reaction conditions can be found in the experimental section. Values with an asterisk were measured at 215 °C.	41
2.8	Carbon amount as measured by elemental analysis before and after catalysis for all three samples. Two measurements were conducted for each sample.	46
2.9	Particle sizes as measured by UV-VIS depending on the pH value and the pH setting value. With ammonium hydroxide, a higher pH value is needed to obtain silver colloids with the same size as with potassium carbonate.	47
A2.1	Calculation for total silver surface per gram in each sample. Calculations were carried out with colloid radius and the assumption that all particles are perfect spheres.	51
3.1	Run protocol for 2 nd ethylene epoxidation catalysts screening at hte.	55
3.2	Results from EDX measurements at four different positions during STEM measurements. Theoretical silver to sulfur ratio was 73. STEM images for marked positions can be found in the appendix.	61
3.3	Performance data at 260 °C without ethylene chloride, with 0.6 and 1.2 ppm EC dosage. More details about the reaction conditions can be found in the experimental section. BC1573 and BC1574 are silver-silver sulfide core-shell particles supported on α -alumina. The BC1575 sample was prepared by adding sulfate via dry impregnation (DI) to the BC991 catalyst. The data for the BC991 catalyst was measured with a slightly different run protocol. Further details can be found in chapter 2.3.	62
4.1	EDX quantitative analysis of nickel, manganese and phosphorus. Nickel to manganese ratio at the regarded position is 3.5.	78
4.2	BET Surface area and nickel loading for NiP@MnO/Al ₂ O ₃ and NiP/Al ₂ O ₃ after reduction at 850 °C. Nickel loading and surface area are slightly higher for the manganese containing sample.	86

4.3	Stability indicators with initial activity and activity after 40 h regarding methane conversion and methane consumption. Methane consumption was calculated with the assumption of an ideal gas. The input gas volume was multiplied with ideal gas volume and divided by the nickel amount.	89
4.4	Comparison of nickel loading, coke formation as measured by TG-MS and the resulting coke formation per g Ni. Manganese addition results in 35 % less coke deposition on the catalyst.	90
A4.1	Bouduard-equilibrium at different temperatures. From David R. Lide: <i>CRC Handbook of Chemistry and Physics</i> , 90th Edition, Taylor & Francis, 2009 .	97
A4.2	EDX calculations for fraction of core to shell ratio. Particles were measured with the imageJ software.	97
5.1	BET Surface area and nickel loading for Ni/ZrO ₂ and Ni/Al ₂ O ₃ after reduction at 500 °C. Nickel loading is slightly higher for the zirconia supported sample, while the surface area is higher for the alumina supported sample.	111
5.2	Performance data at 700 °C during ramp-up, long term measurement with increased WHSV and ramp-down for Ni/ZrO ₂ and Ni/Al ₂ O ₃ . Ni/ZrO ₂ shows the higher initial activity but is less stable compared to Ni/Al ₂ O ₃ . Both samples show very high stability under these conditions.	112
5.3	BET surface area and correlating methane conversion and methane consumption per m ² and nickel loading of Ni/ZrO ₂ and Ni/Al ₂ O ₃ . If methane consumption is calculated per spent catalysts surface area and nickel loading, Ni/ZrO ₂ shows the better performance in comparison to Ni/Al ₂ O ₃ .	114

Literature

- [1] J. A. Dumesic, G. W. Huber, M. Boudart, in *Handb. Heterog. Catal.*, **2008**, pp. 1–15.
- [2] R. Schlögl, *Angew. Chemie - Int. Ed.* **2015**, 3465–3520.
- [3] J. R. H. Ross, in *Heterog. Catal.*, **2012**, pp. 69–89.
- [4] C. Perego, P. Villa, *Catal. Today* **1997**, 34, 281–305.
- [5] J. E. Mondloch, E. Bayram, R. G. Finke, *J. Mol. Catal. A Chem.* **2012**, 355, 1–38.
- [6] P. Munnik, P. E. De Jongh, K. P. De Jong, *Chem. Rev.* **2015**, 115, 6687–6718.
- [7] M. Behrens, *Catal. Today* **2015**, 246, 46–54.
- [8] M. Behrens, D. Brennecke, F. Girgsdies, S. Kibner, A. Trunschke, N. Nasrudin, S. Zakaria, N. F. Idris, S. B. A. Hamid, B. Kniep, et al., *Appl. Catal. A Gen.* **2011**, 392, 93–102.
- [9] J. Shi, *Chem. Rev.* **2013**, 113, 2139–2181.
- [10] A. J. McCue, J. A. Anderson, *Catal. Sci. Technol.* **2014**, 4, 272–294.
- [11] P. G. W. A. Kompio, A. Brückner, F. Hipler, G. Auer, E. Löffler, W. Grünert, *J. Catal.* **2012**, 286, 237–247.
- [12] J. Xie, J. Yang, A. I. Dugulan, A. Holmen, D. Chen, K. P. De Jong, M. J. Louwerse, *ACS Catal.* **2016**, 6, 3147–3157.
- [13] Z. Li, T. Lin, F. Yu, Y. An, Y. Dai, S. Li, L. Zhong, H. Wang, P. Gao, Y. Sun, et al., *ACS Catal.* **2017**, 7, 8023–8032.
- [14] S. K. Kim, J. H. Lee, I. Y. Ahn, W. J. Kim, S. H. Moon, *Appl. Catal. A Gen.* **2011**, 401, 12–19.
- [15] D. Hu, J. Gao, Y. Ping, L. Jia, P. Gunawan, Z. Zhong, G. Xu, F. Gu, F. Su, *Ind. Eng. Chem. Res.* **2012**, 51, 4875–4886.
- [16] Q. Liu, F. Gu, X. Lu, Y. Liu, H. Li, Z. Zhong, G. Xu, F. Su, *Appl. Catal. A Gen.* **2014**, 488, 37–47.
- [17] F. Epron, F. Gauthard, C. Pinéda, J. Barbier, *J. Catal.* **2001**, 198, 309–318.
- [18] R. L. Puurunen, *J. Appl. Phys.* **2005**, 97, 1–52.
- [19] T. M. Onn, S. Zhang, L. Arroyo-Ramirez, Y. C. Chung, G. W. Graham, X. Pan, R. J. Gorte, *ACS Catal.* **2015**, 5, 5696–5701.
- [20] B. J. O'Neill, D. H. K. Jackson, J. Lee, C. Canlas, P. C. Stair, C. L. Marshall, J. W. Elam, T. F. Kuech, J. A. Dumesic, G. W. Huber, *ACS Catal.* **2015**, 5, 1804–1825.
- [21] Y. Lei, S. Lee, K. Bin Low, C. L. Marshall, J. W. Elam, *ACS Catal.* **2016**, 6, 3457–3460.

- [22] E. Baktash, P. Littlewood, R. Schomäcker, A. Thomas, P. C. Stair, *Appl. Catal. B, Environ.* **2015**, *179*, 122–127.
- [23] V. E. Stempel, D. Löffler, J. Kröhnert, K. Skorupska, B. Johnson, R. N. d'Alnoncourt, M. Driess, F. Rosowski, *J. Vac. Sci. Technol. A Vacuum, Surfaces, Film.* **2016**, *34*, 01A135.
- [24] P. Preikschas, J. Bauer, X. Huang, S. Yao, R. Naumann d'Alnoncourt, R. Kraehnert, A. Trunschke, F. Rosowski, M. Driess, *ChemCatChem* **2019**, 885–892.
- [25] P. W. Menezes, A. Indra, P. Littlewood, C. Gçbel, **2016**, 370–377.
- [26] J. Dou, Z. Sun, A. A. Opalade, N. Wang, W. Fu, F. Tao, *Chem. Soc. Rev.* **2017**, *46*, 2001–2027.
- [27] K. Ding, A. Gulec, A. M. Johnson, N. M. Schweitzer, G. D. Stucky, L. D. Marks, P. C. Stair, *Science (80-.)*. **2015**, *350*, 189–192.
- [28] J. P. H. Li, Z. Liu, H. Wu, Y. Yang, *Catal. Today* **2018**, *307*, 84–92.
- [29] I. Maxwell, *United States Patent*, **1977**, US4033903A.
- [30] A. Lauritzen, *United States Patent*, **1988**, US005485919A.
- [31] T. Iwakura, T. Imamoto, K. Nakashiro, *United States Patent*, **1998**, US005705661A.
- [32] J. Lockemeyer, R. Yeates, D. Reinalda, *United States Patent*, **2004**, US2004/0049061.
- [33] L. Zhang, S. Raha, B. Devassy, B. Up-Hade, A. Basrur, A. Philips, R. Tupe, *International Patent*, **2013**, WO2013/086081.
- [34] H. Raffelson, M. Suda, *United States Patent*, **1975**, US3867411.
- [35] J. Wrobelski, *United States Patent*, **1985**, US4515973.
- [36] C. Dobner, M. Duda, A. Raichle, H. Wilmer, F. Rosowski, M. Holzle, *United States Patent*, **2008**, US2008.
- [37] B. Barone, *United States Patent*, **1993**, US5262548.
- [38] C. Schulz, F. Pohl, M. Driess, R. Glaum, F. Rosowski, B. Frank, *Ind. Eng. Chem. Res.* **2019**, *58*, 2492–2502.
- [39] J. K. Nørskov, T. Bligaard, J. Rossmeisl, C. H. Christensen, *Nat. Chem.* **2009**, *1*, 37–46.
- [40] Z. W. Ulissi, A. J. Medford, T. Bligaard, J. K. Nørskov, *Nat. Commun.* **2017**, *8*, 1–7.
- [41] C. J. Burrows, *Acc. Chem. Res.* **2017**, *50*, 445–445.
- [42] F. Zaera, **2013**, *2*, 2746–2762.
- [43] T. S. Rodrigues, M. Zhao, T. H. Yang, K. D. Gilroy, A. G. M. da Silva, P. H. C. Camargo, Y. Xia, *Chem. - A Eur. J.* **2018**, *24*, 16944–16963.
- [44] H. Goesmann, C. Feldmann, *Angew. Chemie - Int. Ed.* **2010**, *49*, 1362–

1395.

- [45] P. L. Gai-Boyes, *Catal. Rev.* **1992**, *34*, 1–54.
- [46] K. An, G. A. Somorjai, *ChemCatChem* **2012**, *4*, 1512–1524.
- [47] A. R. Tao, S. Habas, P. Yang, *Small* **2008**, *4*, 310–325.
- [48] P. Christopher, S. Linic, *J. Am. Chem. Soc.* **2008**, *130*, 11264–11265.
- [49] H. T. Luk, C. Mondelli, D. C. Ferré, J. A. Stewart, J. Pérez-Ramírez, *Chem. Soc. Rev.* **2017**, *46*, 1358–1426.
- [50] I. Lee, F. Delbecq, R. Morales, M. A. Albiter, F. Zaera, *Nat. Mater.* **2009**, *8*, 132–138.
- [51] S. Shankar, A. Rai, B. Ankamwar, A. Singh, A. Ahmad, M. Sastry, *Nat. Mater.* **2004**, *3*, 482–488.
- [52] G. Berhault, M. Bausach, L. Bisson, L. Becerra, C. Thomazeau, D. Uzio, *J. Phys. Chem. C* **2007**, 5915–5925.
- [53] V. K. Lamer, R. H. Dinegar, *J. Am. Chem. Soc.* **1950**, *72*, 4847–4854.
- [54] N. T. K. Thanh, N. Maclean, S. Mahiddine, *Chem. Rev.* **2014**, *114*, 7610–7630.
- [55] J. Polte, *CrystEngComm* **2015**, *17*, 6809–6830.
- [56] R. Ghosh Chaudhuri, S. Paria, *Chem. Rev.* **2012**, *112*, 2373–2433.
- [57] H. Wang, L. Chen, Y. Feng, H. Chen, *Acc. Chem. Res.* **2013**, *46*, 1636–1646.
- [58] K. Chatterjee, S. Sarkar, K. Jagajjanani Rao, S. Paria, *Adv. Colloid Interface Sci.* **2014**, *209*, 8–39.
- [59] E. A. Kwizera, E. Chaffin, Y. Wang, X. Huang, *RSC Adv.* **2017**, *7*, 17137–17153.
- [60] M. B. Gawande, A. Goswami, T. Asefa, H. Guo, A. V. Biradar, D. L. Peng, R. Zboril, R. S. Varma, *Chem. Soc. Rev.* **2015**, *44*, 7540–7590.
- [61] M. Volmer, A. Weber, *Zeitschrift für Phys. Chemie* **1926**, *119*, 277–301.
- [62] J. Frenkel, *J. Chem. Phys.* **1939**, *7*, 538–547.
- [63] S. Navalon, H. Garcia, *Nanomaterials* **2016**, *6*, 1–4.
- [64] R. Merkle, J. Maier, *Zeitschrift für Anorg. und Allg. Chemie* **2005**, *631*, 1163–1166.
- [65] M. D. Argyle, C. H. Bartholomew, *Catalysts* **2015**, *5*, 145–269.
- [66] C. J. Jia, F. Schüth, *Phys. Chem. Chem. Phys.* **2011**, *13*, 2457–2487.
- [67] G. A. Somorjai, J. Y. Park, *Angew. Chemie - Int. Ed.* **2008**, *47*, 9212–9228.
- [68] M. Cargnello, C. Chen, B. T. Diroll, V. V. T. Doan-Nguyen, R. J. Gorte, C. B. Murray, *J. Am. Chem. Soc.* **2015**, *137*, 6906–6911.
- [69] J. A. Lopez-Sanchez, N. Dimitratos, C. Hammond, G. L. Brett, L. Kesavan, S.

- White, P. Miedziak, R. Tiruvalam, R. L. Jenkins, A. F. Carley, et al., *Nat. Chem.* **2011**, *3*, 551–556.
- [70] M. Crespo-Quesada, J. M. Andanson, A. Yarulin, B. Lim, Y. Xia, L. Kiwi-Minsker, *Langmuir* **2011**, *27*, 7909–7916.
- [71] E. W. Elliott, R. D. Glover, J. E. Hutchison, *ACS Nano* **2015**, *9*, 3050–3059.
- [72] E. L. Rosen, R. Buonsanti, A. Llordes, A. M. Sawvel, D. J. Milliron, B. A. Helms, *Angew. Chemie - Int. Ed.* **2012**, *51*, 684–689.
- [73] M. Casavola, J. Hermannsdörfer, N. De Jonge, A. I. Dugulan, K. P. De Jong, *Adv. Funct. Mater.* **2015**, *25*, 5309–5319.
- [74] A. Villa, D. Wang, G. M. Veith, F. Vindigni, L. Prati, *Catal. Sci. Technol.* **2013**, *3*, 3036–3041.
- [75] “<https://www.shell.com/business-customers/global-solutions/petrochemicals-technologies-licensing/ethylene-oxide-ethylene-glycol-processes.html>,” **2018**.
- [76] S. Rebsdatt, D. Mayer, *Ullmann’s Encycl. Ind. Chem.* **2012**, 547–572.
- [77] J. K. Lee, X. E. Verykios, R. Pitchai, *Appl. Catal.* **1988**, *44*, 223–237.
- [78] M. O. Özbek, I. Önal, R. A. Van Santen, *ChemCatChem* **2013**, *5*, 443–451.
- [79] M. O. Özbek, I. Önal, R. A. Van Santen, *ChemCatChem* **2011**, *3*, 150–153.
- [80] W. Diao, C. D. Digiulio, M. T. Schaal, S. Ma, J. R. Monnier, *J. Catal.* **2015**, *322*, 14–23.
- [81] M. O. Özbek, R. A. Van Santen, *Catal. Letters* **2013**, *143*, 131–141.
- [82] C. Stegelmann, N. C. Schiødt, C. T. Campbell, P. Stoltze, *J. Catal.* **2004**, *221*, 630–649.
- [83] P. A. Kilty, W. M. H. Sachtler, *Catal. Rev.* **1974**, *10*, 1–16.
- [84] R. B. Grant, R. M. Lambert, *Langmuir* **1985**, *1*, 29–33.
- [85] R. B. Grant, R. M. Lambert, *J. Catal.* **1985**, *375*, 364–375.
- [86] R. A. Van Santen, H. P. C. E. Kuipers, *Adv. Catal.* **1987**, *35*, 265–321.
- [87] V. V. Kaichev, R. W. Mayer, R. Schlo, *Phys. Rev. B* **2003**, *67*, 1–12.
- [88] T. C. R. Rocha, M. Hävecker, A. Knop-Gericke, R. Schlögl, *J. Catal.* **2014**, *312*, 12–16.
- [89] T. Campbell, *Surf. Sci.* **1985**, *157*, 43–60.
- [90] C. Rehren, G. Isaac, G. Ertl, *Catal. Letters* **1991**, *11*, 6–10.
- [91] X. Bao, B. Pettinger, G. Ertl, R. Schlögl, *Berichte der Bunsen Gesellschaft für Phys. Chemie* **1993**, *97*, 322–325.
- [92] A. J. Nagy, G. Mestl, D. Herein, G. Weinberg, E. Kitzelmann, R. Schlögl, *J. Catal.* **1999**, *429*, 417–429.
- [93] S. Linic, M. A. Barteau, *J. Am. Chem. Soc.* **2002**, *124*, 310–317.

- [94] S. Linic, M. A. Barteau, *J. Catal.* **2003**, *214*, 200–212.
- [95] D. Torres, F. Illas, R. M. Lambert, *J. Catal.* **2008**, *260*, 380–383.
- [96] E. A. Carbonio, T. C. R. Rocha, A. Klyushin, I. Pis, E. Magnano, S. Nappini, S. Piccinin, A. Knop-Gericke, R. Schlögl, T. Jones, *Chem. Sci.* **2018**, *9*, 990–998.
- [97] T. E. Jones, R. Wyrwich, S. Bo, E. A. Carbonio, M. T. Greiner, A. Y. Klyushin, W. Moritz, A. Locatelli, T. O. Montes, M. A. Nin, et al., *ACS Catal.* **2018**, *8*, 3844–3852.
- [98] V. I. Bukhtiyarov, A. I. Nizovskii, H. Bluhm, M. Hävecker, E. Kleimenov, A. Knop-Gericke, R. Schlögl, *J. Catal.* **2006**, *238*, 260–269.
- [99] G. L. Bezemer, J. H. Bitter, H. P. C. E. Kuipers, H. Oosterbeek, J. E. Holewijn, X. Xu, F. Kapteijn, A. J. Van Diilen, K. P. De Jong, *J. Am. Chem. Soc.* **2006**, *128*, 3956–3964.
- [100] M. Valden, X. Lai, D. W. Goodman, *Science (80-.)*. **1998**, *281*, 1647–1650.
- [101] J. N. Kuhn, W. Huang, C. K. Tsung, Y. Zhang, G. A. Somorjai, *J. Am. Chem. Soc.* **2008**, *130*, 14026–14027.
- [102] S. N. Goncharova, E. A. Paukshtis, B. S. Bal'zhinimaev, *Appl. Catal. A, Gen.* **1995**, *126*, 67–84.
- [103] J. Wu, P. Harriott, *J. Catal.* **1975**, *402*, 395–402.
- [104] X. Verykios, F. Stein, R. W. Coughian, *J. Catal.* **1980**, *382*, 368–382.
- [105] J. K. Lee, X. E. Verykios, R. Pitchai, *Appl. Catal.* **1989**, *50*, 171–188.
- [106] S. V. Tsybulya, G. N. Kryukova, S. N. Goncharova, A. N. Shmakov, B. S. Bal'zhinimaev, *J. Catal.* **1995**, *154*, 194–200.
- [107] V. I. Bukhtiyarov, I. P. Prosvirin, R. I. Kvon, S. N. Goncharova, B. S. Bal'zhinimaev, *J. Chem. Soc. Faraday Trans.* **1997**, *93*, 2323–2329.
- [108] J. E. Van den Reijen, S. Kanungo, T. A. J. Welling, M. Versluijs-helder, T. A. Nijhuis, K. P. De Jong, P. De Jongh, *J. Catal.* **2017**, *356*, 65–74.
- [109] Y. Cao, R. Zheng, X. Ji, H. Liu, R. Xie, W. Yang, *Langmuir* **2014**, *30*, 3876–3882.
- [110] V. Bastús, N.; Merkoçi, F; Piella, J.; Puentes, *Chem. Mater.* **2014**, *26*, 2836–2846.
- [111] M. Volmer, A. Weber, *Zeitschrift fur Phys. Chemie* **1926**, *119*, 277–301.
- [112] S. Karthika, T. K. Radhakrishnan, P. Kalaichelvi, *Cryst. Growth Des.* **2016**, *16*, 6663–6681.
- [113] S. Zeng, D. Baillargeat, *Chem. Soc. Rev.* **2014**, 3426.
- [114] T. Wriedt, *Mie Theory: A Review*, Springer-Verlag, **2012**.
- [115] A. Birrozzi, M. Copley, J. von Zamory, M. Pasqualini, S. Calcaterra, F. Nobili, A. Di Cicco, H. Rajantie, M. Briceno, E. Bilbé, et al., *J. Electrochem. Soc.* **2015**, *162*, A2331–A2338.

- [116] C. Kästner, A. F. Thünemann, *Langmuir* **2016**, *32*, 7383–7391.
- [117] T. Rosendahl, T. Mäurer, C. Dobner, A. Lehr, J. Wanka, *BASF Patent EO Cat 2013*, **2013**, WO2013/061294A1.
- [118] Z. Xia, A. Singh, W. Kiratitanavit, R. Mosurkal, J. Kumar, R. Nagarajan, *Thermochim. Acta* **2015**, *605*, 77–85.
- [119] P. S. Bailey, *Chem. Rev.* **1958**, *58*, 925–1010.
- [120] C. Aliaga, J. Y. Park, Y. Yamada, H. S. Lee, C. Tsung, P. Yang, G. Somorjai, *J. Phys. Chem. C* **2009**, *113*, 6150–6155.
- [121] J. Shen, H. Ziaei-Azad, N. Semagina, *J. Mol. Catal. A Chem.* **2014**, *391*, 36–40.
- [122] V. Lazarescu, M. Stanciu, M. Vass, *Stud. Surf. Sci. Catal.* **1994**, *82*, 495–498.
- [123] D. Ren, H. Xu, J. Li, J. Li, D. Cheng, *Mol. Catal.* **2017**, *441*, 92–99.
- [124] D. Ren, G. Cheng, J. Li, J. Li, W. Dai, X. X. Sun, D. Cheng, *Catal. Letters* **2017**, *147*, 2920–2928.
- [125] S. Tan, R. Grant, R. Lambert, *J. Catal.* **1987**, *106*, 54–64.
- [126] H. Liu, F. Ye, H. Cao, G. Ji, J. Y. Lee, J. Yang, *Nanoscale* **2013**, *5*, 6901–7.
- [127] S. I. Sadovnikov, A. I. Gusev, E. Y. Gerasimov, A. A. Rempel, *Inorg. Mater.* **2016**, *52*, 441–446.
- [128] N. Cathcart, A. J. Frank, V. Kitaev, *Chem. Commun.* **2009**, 7170–7172.
- [129] S. George, S. Lin, Z. Ji, C. R. Thomas, L. Li, M. Mecklenburg, H. Meng, X. Wang, H. Zhang, T. Xia, et al., *ACS Nano* **2012**, *6*, 3745–3759.
- [130] R. Horn, R. Schloegl, *Catal. Letters* **2015**, *145*, 23–39.
- [131] P. Schwach, X. Pan, X. Bao, *Chem. Rev.* **2017**, *117*, 8497–8520.
- [132] P. B. Armentrout, *Chem. - A Eur. J.* **2016**, *22*, 1–10.
- [133] P. Djinovic, I. Crnivec, B. Erjavec, A. Pintar, *Appl. Catal. B Environ.* **2012**, *125*, 259–270.
- [134] S. Wang, D. Cao, Y. Li, J. Wang, H. Jiao, *J. Phys. Chem. B* **2006**, 9976–9983.
- [135] G. Centi, E. A. Quadrelli, S. Perathoner, *Energy Environ. Sci.* **2013**, 1711–1731.
- [136] D. Pakhare, J. Spivey, *Chem. Soc. Rev.* **2014**, 7813–7837.
- [137] M. Usman, W. M. A. W. Daud, H. F. Abbas, *Renew. Sustain. Energy Rev.* **2015**, *45*, 710–744.
- [138] S. Kawi, Y. Kathiraser, J. Ni, U. Oemar, Z. Li, *ChemSusChem* **2015**, 3556–3575.
- [139] S. Li, J. Gong, *Chem. Soc. Rev.* **2014**, *43*, 7245–7256.

- [140] W. Chung, M. Chang, *Renew. Sustain. Energy Rev.* **2016**, *62*, 13–31.
- [141] D. P. Serrano, J. A. Botas, R. Guil-lopez, *Int. J. Hydrogen Energy* **2009**, *34*, 4488–4494.
- [142] J. Han, J. Seong, M. Suk, H. Lee, *Appl. Catal. B, Environ.* **2017**, *203*, 625–632.
- [143] D. Liu, X. Yang, W. Ni, E. Cheo, R. Lau, A. Borgna, Y. Yang, *J. Catal.* **2009**, *266*, 380–390.
- [144] C. Wang, N. Sun, M. Kang, X. Wen, N. Zhao, F. Xiao, W. Wei, T. Zhao, Y. Sun, *Catal. Sci. Technol.* **2013**, *3*, 2435–2443.
- [145] X. Li, D. Li, H. Tian, L. Zeng, Z. Zhao, J. Gong, *Appl. Catal. B, Environ.* **2017**, *202*, 683–694.
- [146] A. Tsoukalou, Q. Imtiaz, S. M. Kim, P. M. Abdala, S. Yoon, C. R. Müller, *J. Catal.* **2016**, *343*, 208–214.
- [147] K. Sutthiumporn, S. Kawi, *Int. J. Hydrogen Energy* **2011**, *36*, 14435–14446.
- [148] B. Li, W. Su, X. Wang, X. Wang, *Int. J. Hydrogen Energy* **2016**, *41*, 14732–14746.
- [149] N. Zhao, N. Sun, *Catal. Sci. Technol.* **2016**, *6*, 449–459.
- [150] S. A. Theofanidis, V. V Galvita, H. Poelman, G. B. Marin, *ACS Catal.* **2015**, *5*, 3028–3039.
- [151] S. M. Kim, P. M. Abdala, T. Margossian, D. Hosseini, L. Foppa, A. Armutlulu, W. Van Beek, A. Comas-vives, C. Coperet, C. Mueller, *J. Am. Chem. Soc.* **2017**, *139*, 1937–1949.
- [152] K. Mette, S. Ku, A. Tarasov, M. G. Willinger, J. Kro, S. Wrabetz, A. Trunschke, M. Scherzer, F. Girgsdies, H. Du, et al., *ACS Catal.* **2016**, *6*, 7238–7248.
- [153] S. Seok, S. Hwan, J. Sung, *Appl. Catal. A Gen.* **2001**, *215*, 31–38.
- [154] F. Guo, J. Xu, W. Chu, *Catal. Today* **2015**, *256*, 124–129.
- [155] L. Yao, J. Zhu, X. Peng, D. Tong, C. Hu, *Int. J. Hydrogen Energy* **2013**, *38*, 7268–7279.
- [156] L. Yao, J. Shi, C. Hu, *RSC Adv.* **2015**, *5*, 90168–90177.
- [157] P. Littlewood, X. Xie, M. Bernicke, A. Thomas, R. Schomäcker, *Catal. Today* **2015**, *242*, 111–118.
- [158] L. Zhou, L. Li, N. Wei, J. Li, J. Basset, *ChemCatChem* **2015**, *7*, 2508–2516.
- [159] B. Phillips, J. Hutta, I. Warshaw, *J. Am. Ceram. Soc.* **1963**, *46*, 579–583.
- [160] T. Margossian, K. Larmier, S. M. Kim, F. Krumeich, A. Fedorov, P. Chen, C. R. Müller, C. Copéret, *J. Am. Chem. Soc.* **2017**, *139*, 6919–6927.
- [161] S. K. Z. Li, L. Mo, Y. Kathiraser, *ACS Catal.* **2014**, *4*, 1526–1536.

- [162] S. K. Z. Li, J. Kathiraser, J. Ashok, U. Oemer, *Langmuir* **2014**, *30*, 14694–14705.
- [163] H. Tian, X. Li, L. Zeng, J. Gong, *ACS Catal.* **2015**, *5*, 4959–4977.
- [164] Y. Shi, B. Zhang, *Chem. Soc. Rev.* **2016**, *45*, 1529–1541.
- [165] Y. Pei, Y. Cheng, J. Chen, W. Smith, P. Dong, P. M. Ajayan, M. Ye, J. Shen, *J. Mater. Chem. A* **2018**, *6*, 23220–23243.
- [166] X. Wang, P. Clark, S. T. Oyama, *J. Catal.* **2002**, *208*, 321–331.
- [167] L. Alvarado Rupflin, J. Mormul, M. Lejkowski, S. Titlbach, R. Papp, R. Gläser, M. Dimitrakopoulou, X. Huang, A. Trunschke, M. G. Willinger, et al., *ACS Catal.* **2017**, *7*, 3584–3590.
- [168] S. Carenco, Z. Liu, M. Salmeron, *ChemCatChem* **2017**, *9*, 2318–2323.
- [169] U. Guharoy, T. Ramirez Reina, E. Olsson, S. Gu, Q. Cai, *ACS Catal.* **2019**, *9*, 3487–3497.
- [170] A. Johnston-Peck, J. Wang, J. Tracy, *ACS Nano* **2009**, *3*, 1077–1084.
- [171] J. Park, E. Kang, C. J. Bae, J. G. Park, H. J. Noh, J. Y. Kim, J. H. Park, H. M. Park, T. Hyeon, *J. Phys. Chem. B* **2004**, *108*, 13594–13598.
- [172] S. Carenco, C. Boissière, L. Nicole, C. Sanchez, P. Le Floch, N. Mézailles, *Chem. Mater.* **2010**, *22*, 1340–1349.
- [173] Z. Bian, S. Das, M. H. Wai, P. Hongmanorom, S. Kawi, *ChemPhysChem* **2017**, *18*, 3117–3134.
- [174] N. Jiang, H. Song, H. L. Song, X. W. Xu, F. Y. Zhang, *Russ. J. Appl. Chem.* **2017**, *90*, 1883–1891.
- [175] H. Song, M. Dai, Y. T. Guo, Y. J. Zhang, *Fuel Process. Technol.* **2012**, *96*, 228–236.
- [176] S. T. Oyama, X. Wang, Y. K. Lee, K. Bando, F. G. Requejo, *J. Catal.* **2002**, *210*, 207–217.
- [177] P. Munnik, M. E. Z. Velthoen, P. E. De Jongh, K. P. De Jong, C. J. Gommers, *Angew. Chemie - Int. Ed.* **2014**, *53*, 9493–9497.
- [178] R. Prins, M. E. Bussell, *Catal. Letters* **2012**, *142*, 1413–1436.
- [179] A. P. Grosvenor, M. C. Biesinger, R. S. C. Smart, N. S. McIntyre, *Surf. Sci.* **2006**, *600*, 1771–1779.
- [180] D. Fa, B. Yu, Y. Miao, *Colloids Surfaces A Physicochem. Eng. Asp.* **2019**, *564*, 31–38.
- [181] Y. Pan, Y. Liu, J. Zhao, K. Yang, J. Liang, D. Liu, W. Hu, D. Liu, Y. Liu, C. Liu, *J. Mater. Chem. A* **2015**, *3*, 1656–1665.
- [182] Z. Huang, Z. Chen, Z. Chen, C. Lv, H. Meng, C. Zhang, *ACS Nano* **2014**, *8*, 8121–8129.
- [183] R. Franke, T. Chassé, P. Streubel, A. Meisel, *J. Electron Spectros. Relat. Phenomena* **1991**, *56*, 381–388.

- [184] A. J. Nelson, S. Frigo, R. Rosenberg, *J. Appl. Phys.* **1992**, *71*, 6086–6089.
- [185] T. Margossian, K. Larmier, S. M. Kim, F. Krumeich, C. Mueller, C. Coperet, *ACS Catal.* **2017**, *7*, 6942–6948.
- [186] N. Wang, W. Chu, T. Zhang, X. Zhao, *Chem. Eng. J.* **2011**, *170*, 457–463.
- [187] J. F. Moulder, W. F. Stickle, P. E. Sobol, K. D. Bomben, *Handbook of X-Ray Photoelectron Spectroscopy*, **1992**.
- [188] J. S. Beck, J. C. Vartuli, W. J. Roth, M. E. Leonowicz, C. T. Kresge, K. D. Schmitt, C. T. W. Chu, D. H. Olson, E. W. Sheppard, S. B. McCullen, et al., *J. Am. Chem. Soc.* **1992**, *114*, 10834–10843.
- [189] D. Zhao, Q. Huo, J. Feng, B. F. Chmelka, G. D. Stucky, *J. Am. Chem. Soc.* **1998**, *120*, 6024–6036.
- [190] T. W. Kim, F. Kleitz, B. Paul, R. Ryoo, *J. Am. Chem. Soc.* **2005**, *127*, 7601–7610.
- [191] A. Taguchi, F. Schüth, *Ordered Mesoporous Materials in Catalysis*, **2005**.
- [192] D. Trong On, D. Desplandier-Giscard, C. Danumah, S. Kaliaguine, *Appl. Catal. A Gen.* **2003**, *253*, 545–602.
- [193] W. S. Chiang, E. Fratini, P. Baglioni, J. H. Chen, Y. Liu, *Langmuir* **2016**, *32*, 8849–8857.
- [194] B. Coasne, A. Galarneau, F. Di Renzo, R. J. M. Pellenq, *Langmuir* **2006**, *22*, 11097–11105.
- [195] J. Yang, K. Hidajat, S. Kawi, *J. Mater. Chem.* **2009**, *19*, 292–298.
- [196] J. Zhu, K. Kailasam, X. Xie, R. Schomaecker, A. Thomas, *Chem. Mater.* **2011**, *23*, 2062–2067.
- [197] L. Lopez, J. Velasco, V. Montes, A. Marinas, S. Cabrera, M. Boutonnet, S. Järås, *Catalysts* **2015**, *5*, 1737–1755.
- [198] H. Song, R. M. Rioux, J. D. Hoefelmeyer, R. Komor, K. Niesz, M. Grass, P. Yang, G. A. Somorjai, *J. Am. Chem. Soc.* **2006**, *128*, 3027–3037.
- [199] G. Chen, C.-Y. Guo, X. Zhang, Z. Huang, G. Yuan, *Fuel Process. Technol.* **2011**, *92*, 456–461.
- [200] Y. Ren, Z. Ma, P. G. Bruce, *Chem. Soc. Rev.* **2012**, *41*, 4909–4927.
- [201] D. Gu, F. Schüth, *Chem. Soc. Rev.* **2014**, *43*, 313–344.
- [202] A. H. Lu, F. Schüth, *Adv. Mater.* **2006**, *18*, 1793–1805.
- [203] M. Tiemann, *Chem. Mater.* **2008**, *20*, 961–971.
- [204] X. Deng, K. Chen, H. Tüysüz, *Chem. Mater.* **2017**, *29*, 40–52.
- [205] S. W. Boettcher, J. Fan, C. K. Tsung, Q. Shi, G. D. Stucky, *Acc. Chem. Res.* **2007**, *40*, 784–792.
- [206] Q. S. Jing, X. M. Zheng, *Energy* **2006**, *31*, 1848–1856.

- [207] A. Albarazi, P. Beaunier, P. Da Costa, *Int. J. Hydrogen Energy* **2013**, *38*, 127–139.
- [208] M. Rezaei, S. M. Alavi, S. Sahebdehfar, L. Xinmei, L. Qian, Z. F. Yan, *Energy and Fuels* **2007**, *21*, 581–589.
- [209] N. Zhao, N. Sun, **2016**, *6*, DOI 10.1039/c5cy01171j.
- [210] X. Huang, C. Ji, C. Wang, F. Xiao, N. Zhao, N. Sun, W. Wei, Y. Sun, *Catal. Today* **2017**, *281*, 241–249.
- [211] X. Zhu, P. Huo, Y. Zhang, D. Cheng, C. Liu, *Appl. Catal. B, Environ.* **2008**, *81*, 132–140.
- [212] J. Lee, E. Lee, O. Joo, K. Jung, *Appl. Catal. A, Gen.* **2004**, *269*, 1–6.
- [213] L. C. L. Xu, H. Song, *ACS Catal.* **2012**, *2*, 1331–1342.
- [214] B. Liu, R. T. Baker, *J. Mater. Chem.* **2008**, *18*, 5200–5207.
- [215] M. Klapproth, Synthese von Hochoberflächigen Metalloxiden Und Geträgerten Metalloxid-Katalysatoren Für Die Oxidative Kupplung von Methan, Technische Universität Berlin, **2017**.
- [216] J. Roggenbuck, G. Koch, M. Tiemann, *Chem. Mater.* **2006**, *18*, 4151–4156.
- [217] K. A. Cychosz, M. Thommes, *Engineering* **2018**, *4*, 559–566.
- [218] B. W. Hoffer, A. D. Van Langeveld, J. P. Janssens, R. L. C. Bonn e, C. M. Lok, J. A. Moulijn, *J. Catal.* **2000**, *192*, 432–440.
- [219] F. K. McTaggart, *Nature* **1961**, *191*, 1192.